1999

First quasi-elastic polarized electron scattering measurement of polarization transfer to protons in a complex nucleus: Oxygen-16

Krishni Wijesooriya
College of William & Mary - Arts & Sciences

INFORMATION TO USERS

This manuscript has been reproduced from the microfilm master. UMI films the text directly from the original or copy submitted. Thus, some thesis and dissertation copies are in typewriter face, while others may be from any type of computer printer.

The quality of this reproduction is dependent upon the quality of the copy submitted. Broken or indistinct print, colored or poor quality illustrations and photographs, print bleedthrough, substandard margins, and improper alignment can adversely affect reproduction.

In the unlikely event that the author did not send UMI a complete manuscript and there are missing pages, these will be noted. Also, if unauthorized copyright material had to be removed, a note will indicate the deletion.

Oversize materials (e.g., maps, drawings, charts) are reproduced by sectioning the original, beginning at the upper left-hand corner and continuing from left to right in equal sections with small overlaps.

Photographs included in the original manuscript have been reproduced xerographically in this copy. Higher quality 6" x 9" black and white photographic prints are available for any photographs or illustrations appearing in this copy for an additional charge. Contact UMI directly to order.

Bell & Howell Information and Learning
300 North Zeeb Road, Ann Arbor, MI 48106-1346 USA
800-521-0600

UMI®

First $(\vec{e}, e'\vec{p})$ Measurement of Polarization Transfer in a Complex Nucleus: ^{16}O

A Dissertation

Presented to The Faculty of the Department of Physics

The College of William and Mary

In Partial Fulfillment

Of the Requirements for the Degree of

Doctor of Philosophy

By

Krishni Wijesooriya

May 1999

Bell & Howell Information and Learning Company
300 North Zeeb Road
P.O. Box 1346
Ann Arbor, MI 48106-1346

APPROVAL SHEET

This dissertation is submitted in partial fulfillment
of the requirements for the degree of

Doctor of Philosophy.

Krishni Wijesooriya

Krishni Wijesooriya

Approved, May 1999

Professor John Michael Finn

Professor David S. Armstrong

Professor Marc Sher

Professor John Dirk Walecka

Professor Charles Glashausser, Rutgers University

To My Mother and Father.

Contents

Acknowledgments

This thesis would have never been possible were it not for the efforts of many people. First I would like to thank my advisor Mike Finn. In the three years I spent in graduate school at William and Mary, Mike had always directed me into getting things done. From the first Summer I arrived at Wiiliam and Mary, Mike provided support and guidance, while making available to me many opportunities to learn and contribute to new physics. If it were not for Mike, my Ph.D would have taken much longer. I really enjoyed the generous hospitality of Mike and Kit Finn.

I would like to thank my thesis committee members: Mike Finn, Charlie Glashausser, Dirk Walecka, David Armstrong and Marc Sher for reading my thesis. I thank David and Charlie specially for pointing out many mistakes in the original draft of this thesis. Their corrections made this thesis stronger and much easier to read.

I would like to thank the spokespersons of this experiment: Charlie Glashausser, George Chang, Sirish Nanda and Paul Rutt. Special thanks are in order for Charlie, who had always been the guiding force behind this experiment. Every time he payed a visit to CEBAF, I had to work through many sleepless nights to get the results he was interested in. His persistence really directed this analysis in a considerable pace. I would like to thank the Hall A FPP collaboration for making this first FPP experiment in Hall A possible. Some names that come in to my mind are, Ron Gilman, Mark Jones, Charles Perdrisat, Vina Punjabi, Charlie Glashausser, Ron Ransome, Ed Brash, Sergey Malov, Gilles Quemener, Justin McIntyre, Paul Rutt. Most of them were there from the very beginning of the FPP project. A special thanks is due for Mark Jones without whom the FPP project would have taken a longer time. I was so fortunate to have the opportunity to work with Mark, from the time of installation and testing of the FPP chambers, through the commissioning and experiment period and all through the data analysis, Mark was always there to help me whenever I got stuck!!. I would also like to thank Ron Gilman, for advice and guidance throughout

data analysis and for helping me prepare many of my FPP talks. It was a great pleasure to work with Ron and I am happy that I would get to work with him for the next couple of years as well. We all owe a great deal to Ed Brash for writing most of the software for the FPP analysis. Justin McIntyre was another person whom I worked closely with, during the data taking time and the analysis of this experiment. Justin always had a positive attitude towards life that made every one around him take life lightly and enjoy it. I would like to thank Sergey Malov for his many contributions to FPP analysis, including the incorporation of x straws in the tracking routines and analyzing P_n data.

I would like to thank Larry Cardman, Kees De Jager and the Hall A staff members at the time of this experiment: Javier Gomez, John LeRose, Robert Michaels, Bogdan Wojtsekhowski, Eddy Offerman, Meme Liang, J. P. Chen, Sirish Nanda, Arun Saha for their hard work and commitment to getting the Hall A experimental setup up and running in such a timely manner. I would like to thank the Hall A technical staff: Ed Folts, Jack Segal, Mark Stevens, James Proffit, and Scot Spiegel for their hard work and many sleepless nights during the running time of this experiment. I would also like to thank the polarized source group at CEBAF including Charlie Sinclair and Matt Polker for doing their ultimate best to deliver a high intesity polarized beam into the hall with a high polarization as well as getting the Mott polarimeter working. Specially being one of the first experiments in Hall A, and the first to use polarized beam at Jefferson Lab, it is amazing that this experiment ran as scheduled.

I would like to thank Jim Kelly for answering many of my questions regarding how to run his theoretical calculation code, LEA and for his many publications on coincidence electron scattering and polarization observables. We used LEA not only to obtain theoretical numbers to compare to our experimental results but also in acceptance averaging. I would like to thank A.W. Thomas for providing us with calculations on the medium modification effects of the form factor ratio in ^{16}O. I would also like to thank Wally Van Orden and Jan Ryckebusch for providing me with

their theoretical calculations. I would like to thank Paul Ulmer for answering many of my questions regarding his simulation code MCEEP. MCEEP was invaluable during planning and analysis of this experiment.

I would like to thank my friends whose friendship, support and kindness sustained me through many difficult times and helped me get through graduate school. Some of them are Vajeera and Kamal Dorabavilla, Selaka Bulumulla, Vipuli Wijetunge, Nalantha Amarasekara, Udaya and Shiroma Liyanage, Charles and Margeret Halisey, Lotta Ekberg, Jessica Clark, Julie Grossen, Gina Hoatson, D.J. Woolard and Paalo Armore.

I would also like to thank my fellow graduate students and post docs at CEBAF who made my life bearable during this period. Some names (but not all) are: Kevin Fissum, Juncai Gao, Wenxia Zhao, Gilles Quemener, Sergey Malov, Mark Jones, Justin McIntyre, Michael Kuss, Steffen Strauch, Xiadong Jiang, Riad Suleiman, David Prout, Kathy Mccormick, Liminita Todor, and Bill Khal.

I would like to acknowledge the efforts of the William and Mary Physics Department staff: Paula Perry for putting up with my endless excuses for not registering on time and helping me in many other ways, Sylvia Stout for dealing with my travel vouchers and payroll, and Diane Fannin for helping me get Dirk's free times and reserving the conference room whenever I needed it. I would also like to thank all three of them for their friendship and support. I would also like to thank Bill Hersman, my advisor during my time at the University of New Hampshire, for his guidance, support and understanding.

I would like to thank my mother Mrs. Dhanapali Wijesooriya and my father the late Mr. H.P.S. Wijesooriya, for all they have done for me. The best of what I am is what they have given me. I still remember when I was in grade five in elementary school, my mother who was a teacher in the upper-school decided to transfer to the elementary school, because she wanted to make sure that I got the best available education from the beginning. My parents always thought that a good education is

the best thing one can give to their children. I would like to thank my sister Ira and my two brothers Chintaka and Timothy for their encouragement, love, and support. I have to say that Chintaka was the best brother one can ever have. He was unselfish, kind, a person full of principle and was my idol from my childhood.

I would like to mention my son Seth who made a complete change of the way I look at things.

Last but not least, I would like to thank my husband Nilanga for not only being my life partner but also my partner in physics. None of this would have been possible, if not for Nilanga's love and support. I benefited tremendously from his sharp knowledge in physics as well as in data analysis. I remember at a time of software alignment when everyone else had failed to give any suggestions to improve the system he came up with bright ideas!!. I would also like to thank him for reading my thesis several times and giving me important comments.

Finally I would like to acknowledge the NSF grants PHYS-93-11119 and PHYS-98-04343 for funding me during this thesis work and as well as the DOE.

List of Tables

List of Figures

Abstract

The first polarization transfer measurement in the (e,e'p) reaction on a complex nucleus, a study of the exclusive reaction $^{16}O(\vec{e}, e'\vec{p})^{15}N^*$, is discussed in this thesis. This experiment was performed at Jefferson Lab, using the Hall A Focal Plane Polarimeter. This was the first experiment to use polarized beam at Jefferson Lab. Simultaneous measurements were also made for the $H(\vec{e}, e'\vec{p})$ reaction allowing a precise comparison between the form factor ratios for free and bound protons. Since the helicity-dependent, longitudinal (P_l') and transverse (P_t') components of the polarization of the recoil proton are sensitive to the electromagnetic form factors G_E and G_M of the proton inside the nuclear medium, these polarization transfer observables can be used to look for possible medium modification effects on the form factor ratio for the bound proton. The systematic uncertainties involved in performing a recoil polarimetry measurement are minimal, and the theoretical uncertainty (mainly corrections to the Impulse Approximation) are also small. Therefore this measurement provides a sensitive test of the predictions of medium-induced changes in the form factor ratio. Results were obtained for two recoil momentum points, 85 and 140 MeV/c, at a Q^2 of 0.8 $(GeV/c)^2$ in quasielastic, perpendicular kinematics. Within statistical uncertainties, the results are in good agreement with theoretical calculations for the polarization observables obtained assuming free values for the form factors, *i.e.*, the results are consistent with the absence of medium modifications of the nucleon electromagnetic structure. This experiment provides a strong basis for the forthcoming high precision measurements of the ratio G_E/G_M in the nuclear medium.

First $(\vec{e}, e'\vec{p})$ Measurement of Polarization Transfer in a Complex Nucleus: ^{16}O

Chapter 1

Introduction.

With the newly commissioned Focal Plane Polarimeter (FPP) at Jefferson Lab, Hall A, we are able to access the spin degrees of freedom of the electromagnetic interaction of the nucleon via the recoil polarization technique. This thesis discusses the results for the first polarization-transfer experiment in the (e,e'p) reaction performed on a complex nucleus (a nucleus heavier than deuterium). This experiment studied the medium modification effects on the nucleon by comparing the polarization-transfer observables measured for the three valence states of the ^{16}O nucleus, $1p_{1/2}$, $1p_{3/2}$ and $1s_{1/2}$, to those measured for the free proton. This is the first experiment to use the recoil polarimetry technique to look for medium modification effects on the electromagnetic form factor ratio G_E/G_M for the proton inside a medium.

This thesis is separated into six chapters and several appendices, as follows. The present chapter discusses the advantages of using the electromagnetic probe as opposed to hadronic probes, exclusive scattering (e,e'p), as opposed to inclusive scattering (e,e'), and the use of recoil polarimetry methods to measure form factor ratios as opposed to the Rosenbluth separation technique. The chapter concludes with a brief introduction of the present experiment.

The second chapter describes the formalism for coincident polarized electron scattering with a special emphasis on the coincident A$(\vec{e}, e'\vec{p})$B reaction. We introduce

the 18 independent response functions used to describe this reaction and discuss the response functions in the two cases of the Plane Wave Impulse Approximation (PWIA) and the Distorted Wave Impulse Approximation (DWIA). The third chapter discusses the theoretical calculations relevant to the present results. It also contains a discussion on the past evidence from the quest for medium modification effects and takes us to the more recent calculations on this subject leading to the present study of medium modification effects. The fourth chapter gives a detailed discussion of the experimental setup used for this measurement. The fifth chapter deals with the details of the data analysis and includes a description of how the polarization observables were extracted, starting from the raw event data in the detectors used. Finally the sixth chapter contains the results for both the H and the ^{16}O data with a comparison to the available theories. The chapter concludes with a discussion of the results, and the outlook for future experiments.

1.1 The electromagnetic probe.

One of the fundamental problems of nuclear physics has been to develop a complete understanding of the electromagnetic structure of the nucleus. Electron scattering allows us to investigate the electromagnetic structure of the relevant nuclear (hadronic) states with confidence, since certain properties of the electromagnetic interaction make electron scattering a special tool [1]:

- The electromagnetic interaction is very well described by the fundamental theory of Quantum Electrodynamics (QED). Thus, in considering electron scattering from hadrons, the leptonic part of the reaction can be presumed to be very well known, allowing one to probe the nuclear current. In the case of hadronic probes (protons and pions), the effects of the reaction mechanisms are difficult to separate from those of the underlying nuclear structure.

- The electromagnetic coupling, characterized by the fine structure constant $\alpha = e^2/\hbar c \approx 1/137.036$, is relatively small, and thus the reaction can be described by the one photon exchange approximation.

- Since the electromagnetic interaction is not so weak as the weak interaction (for example, neutrino scattering), typical cross sections are not so small. However, since the coupling constants for strong interactions are larger than for the electromagnetic interaction, the use of a hadronic probe will allow the experimenter to utilize a higher cross-section (requiring less beam time and luminosity) than with an electron beam.

- The hadronic probes, due to the relatively large non-perturbative coupling, only sample the surface of the nucleus while the electrons penetrate the entire nuclear volume.

However, one disadvantage of using electrons as a probe is that, due to the small mass of the electron, even at relatively low energies one has to worry about radiative corrections in the analysis.

1.2 Inclusive vs. exclusive electron scattering.

There are two general types of electron scattering experiments: inclusive scattering and exclusive scattering. In the case of inclusive experiments, (e,e'), one detects only the scattered electron, which means that the final state of the nucleus can be one of many possible final states. Figure 1.1 shows the variation of the cross section as a function of the energy transfer, ω, for a typical inclusive electron scattering experiment, [2].

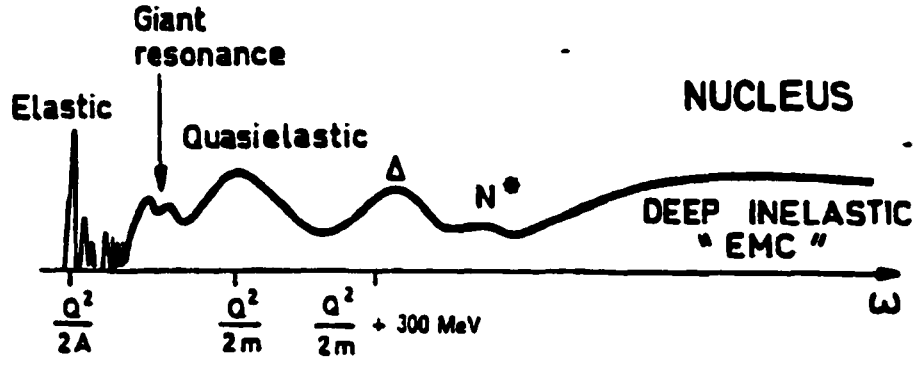

Figure 1.1: A typical spectrum for inclusive scattering at fixed Q^2.

At the lowest value of the energy transfer, ω the first sharp peak in this spectrum at ω=Q^2/2A (where A is the mass of the nucleus, and Q^2 is the four momentum transfer where $\hbar$=c=1.) corresponds to elastic scattering of electrons off of the nucleus. The discrete states immediately above the elastic peak correspond to the target nucleus being excited to nuclear excited states following the scattering. At still higher ω, the "giant resonance" peaks correspond to collective excitation of the nucleus. The bump centered around ω=$Q^2/2M_N$, (where M_N is the mass of the nucleon) the quasielastic peak, corresponds to scattering of the electrons off individual nucleons. This is the region at which the present data were collected. In this region the energy transfered by the electron matches the energy required to elastically scatter off a single nucleon. Thus, in this region, it is most likely that the energy transfer given by a single photon is absorbed by a single nucleon which is knocked out without disturbing the rest of the nucleus. The width of the quasielastic peak is experimentally shown to be due to the Fermi motion of the nucleons inside the nucleus [3], [4], [5]. At yet higher values of ω come two broad bumps corresponding to nucleon excitations to higher Δ and N* resonances. Finally comes the deep inelastic region where the quark scaling behavior (*i.e.*, the quark-gluon behavior of the nucleon becomes dominant) is expected to play a role.

In the case of unpolarized (e,e′) scattering off a nucleon, the differential cross section depends only on two response functions, R_L and R_T:

$$\frac{d\sigma}{d\Omega} = \frac{\sigma_M}{1+2E_i\sin^2(\theta_e/2A)}[\frac{Q^4}{\vec{q}^4}R_L + (\frac{Q^2}{2\vec{q}^2} + \tan^2(\theta_e/2))R_T] \quad (1.1)$$

$$\sigma_M = \frac{\alpha^2\cos^2(\theta_e/2)}{4E_i^2\sin^4(\theta_e/2)}, \quad (1.2)$$

where σ_M is the Mott cross section, α is the fine structure constant, θ_e is the electron scattering angle, and E_i is the initial electron energy. R_L and R_T are the longitudinal and transverse response functions which can be expanded in terms of multi-pole operators of the charge and current density of the nucleus. R_L and R_T are the only two response functions that can be determined from an analysis of unpolarized inclusive scattering data. This R_L, R_T separation is made by varying the kinematics of the incident and scattered electrons (such as the incident energy and the scattering angle) while keeping the energy transfer (ω) and the three-momentum transfer ($\vec{q}$) fixed (Rosenbluth separation for inclusive scattering [7]).

Figure 1.2 shows the charge distribution for ^{16}O nucleus obtained from a Fourier transform of experimental data [8], compared to theoretical calculations. The agreement is reasonable.

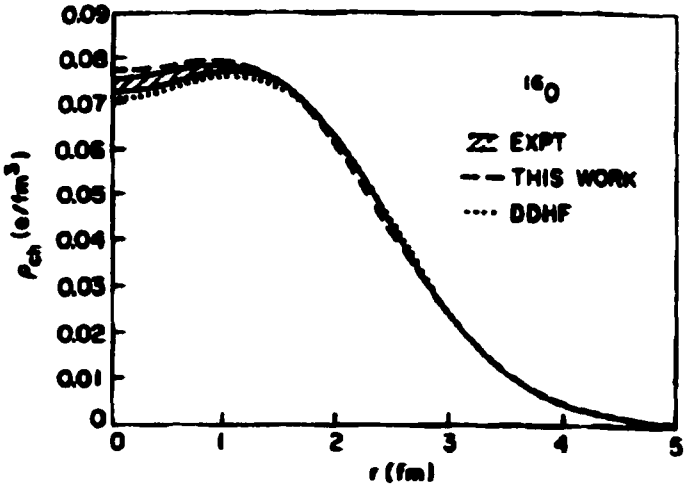

Figure 1.2: Charge density distribution for ^{16}O taken from Ref. [6]. The experimental results are from [8]. the curve labelled "This work" is from Ref. [9] and the Density Dependent Hatree-Fock, "DDHF" curve is from Ref. [10].

In order to probe nuclear structure further, one has to use exclusive (coincidence) electron scattering. In exclusive electron scattering, in addition to detecting the momentum and angle of the scattered electron, one or more other spectrometers are used in coincidence with the scattered electron to detect the knocked-out particles. In this case the final state of the nucleus can be determined or at least partially constrained. If the ejected particle is a proton, the reaction is called (e,e'p). In the case of unpolarized coincidence experiments it is possible to determine four response functions (R_L, R_T, R_{LT} and R_{TT}), where the response function separation is achieved by varying the electron kinematics in analogy with the Rosenbluth separation. Additional spin degrees of freedom enter into polarized coincidence electron scattering, which is the technique used to obtain the present data, is described in detail in Chapter 2.

1.3 Form factors.

The form factors of the nucleon give information about the internal structure of the nucleon. Particularly, the Sachs form factors, G_E and G_M are the Fourier transforms of the nucleon charge and magnetic moment distributions respectively. In the case of a proton, as Q^2 goes to zero, $G_E \rightarrow 1$ and $G_M \rightarrow \mu$. Here μ is the magnetic moment of the proton. Another set of form factors, commonly used by theorists, the Dirac (F1) and Pauli (F2) form factors are related to G_E and G_M by

$$G_E = F_1 - \frac{kQ^2}{4M_N^2}F_2 \tag{1.3}$$

$$G_M = F_1 + kF_2. \tag{1.4}$$

Here k is the anomalous magnetic moment of the proton and is related to the magnetic moment of the proton, μ by

$$\mu = F_1(0) + kF_2(0). \tag{1.5}$$

As Q^2 goes to zero, $F_1 \rightarrow 1$, $F_2 \rightarrow 1$ in the case of a proton.

1.4 Rosenbluth separation technique and the recoil polarization technique.

Until now all studies have used the conventional Rosenbluth separation technique to measure medium modification effects on the nucleon. The experimental results obtained from this method will be discussed in Chapter 3.

1.4.1 Rosenbluth separation technique.

For the specific case of elastic (e,e') scattering from the nucleon the inclusive cross section, Eq. 1.1 can be expressed as

$$[\frac{d\sigma}{d\Omega_e}]_{Rosenbluth} = [\frac{d\sigma}{d\Omega_e}]_{ns} \times [\frac{G_E^2(Q^2)}{1+\tau} + \tau G_M^2(Q^2)(\frac{1}{1+\tau} + 2\tan^2(\theta_e/2))]. \quad (1.6)$$

Here $\tau = Q^2/4M_N^2$, $[\frac{d\sigma}{d\Omega_e}]_{ns}$ is the Mott cross section times a target recoil factor. The above equation can be simplified as

$$[\frac{d\sigma}{d\Omega_e}]_{Rosenbluth} = [\frac{d\sigma}{d\Omega_e}]_{ns} \times [\frac{1}{1+\tau}[G_E^2(Q^2) + \frac{\tau}{\epsilon}G_M^2(Q^2)]]. \quad (1.7)$$

Here,

$$\epsilon(\theta_e) = [1 + 2(1+\tau)\tan^2(\theta_e/2)]^{-1}, \quad (1.8)$$

where ϵ is the virtual photon's longitudinal polarization which ranges from 0 to 1 as θ_e goes from π to 0 in radians. For Rosenbluth separation, it is convenient to define a reduced cross section which is a function of Q^2 and ϵ:

$$[\frac{d\sigma}{d\Omega_e}]_{reduced} = \frac{\epsilon(1+\tau)}{[\frac{d\sigma}{d\Omega_e}]_{ns}}[\frac{d\sigma}{d\Omega_e}]_{Rosenbluth} \quad (1.9)$$

$$\times [\tau G_M^2(Q^2) + \epsilon G_E^2(Q^2)]. \quad (1.10)$$

Using this equation, a set of measurements at fixed Q^2 but different values of E_i and θ_e can be used to determine the form factors. The reduced cross sections are usually plotted against ϵ with τG_M^2 as the intercept and G_E^2 as the slope.

Since data taken under different kinematical conditions are used in the extraction of the form factors from the Rosenbluth separation technique. the extracted form factors are sensitive to systematic errors in electron beam energies, the angles of both the scattered electron and the ejected proton, and the spectrometer acceptances. Furthermore, at high Q^2, $\tau G_M^2 \gg G_E^2$. Thus determination of the Rosenbluth slope (G_E^2) is very difficult. As will be shown in Chapter 2, the form factor ratio can be determined using spin degrees of freedom as in the case of the present experiment. In this way, the systematic error can be reduced since this determination is performed at only one kinematical configuration. As will be shown in Chapter 3, since theoretical calculations show that polarization-transfer coefficients are insensitive to Final State Interaction (FSI), and Meson Exchange Current (MEC) effects, (in contrast to an R_L, R_T separation, where the contributions due to these effects are significant) the interpretation of a polarimetry measurement will be much cleaner.

1.4.2 Principles of recoil polarimetry.

In the recoil polarimetry technique, the spin dependence of the nuclear interaction is determined by measuring the polarization of particles in their final state. At intermediate energies, an asymmetry measured from a secondary scattering analyzer (polarimeter) is used to calculate these final state polarizations. In most laboratories, ^{12}C is used as this secondary scatterer. A Focal Plane Polarimeter (FPP) contains the secondary scatterer and the detectors to measure particle tracks before and after the secondary scattering. The Jefferson Lab, Hall A FPP is described in greater detail in Chapter 4. Due to the spin-orbit force, proton-^{12}C scattering is azimuthally asymmetric. The degree of this asymmetry is a measure of the polarization of the proton. A sketch of this scattering reaction indicating the two angles of interest is

shown in Fig 1.3.

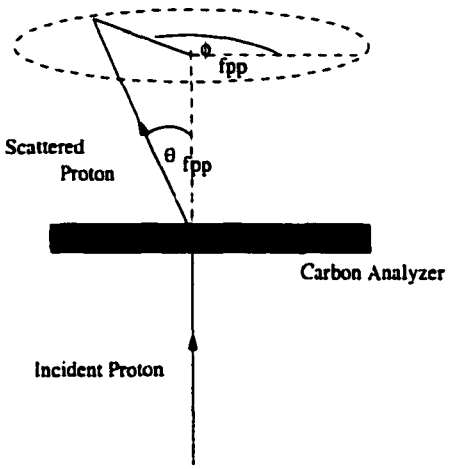

Figure 1.3: Schematic diagram showing the two angles of interest, θ_{fpp} and ϕ_{fpp}, measured by the FPP.

The probability that a proton scattering off a ^{12}C nucleus with a spin dependent asymmetry is defined as the analyzing power of the FPP. The analyzing power of the secondary scatterer (A_c) is a function of the scattering angle θ_{fpp} and the kinetic energy of the incident proton (T_p). A_c has been determined for a considerable range of angles and kinetic energies at several laboratories using protons with known polarizations [15], [16], [17], [18], [19]. A typical distribution of A_c as a function of the scattering angle θ_{fpp} is shown in Figure 1.4, taken from [18].

As the figure shows, for small angle scattering events of θ_{fpp} (about 90% of the scattered events) have no analyzing power. This is the main drawback of the recoil polarimetry technique: in spite of all the advantages, the efficiency of the FPP, which is the ratio of the number of nuclear scattered events to that of incident events on the carbon analyzer, is only around 10%. The statistical error on the measured polarization P of N_{inc} incoming particles is given by

$$\Delta P = \frac{\sqrt{2}}{F\sqrt{N_{inc}}}. \tag{1.11}$$

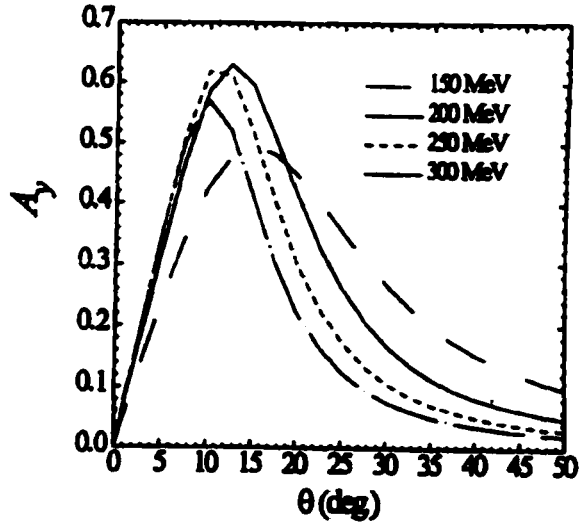

Figure 1.4: Analyzing power vs θ_{fpp} for p-^{12}C reaction obtained for different proton kinetic energies [18].

Here the constant F, the figure of merit, is a quantity characteristic of the polarimeter. F is defined via

$$F^2 = \int_{\theta_{fpp}^{min}}^{\theta_{fpp}^{max}} A_c^2(\theta_{fpp})\epsilon(\theta_{fpp})d\theta_{fpp}. \tag{1.12}$$

Here ϵ is the efficiency of the FPP.

From an FPP we can measure two polarization components, the normal component (P_n^{fp}) and transverse component (P_t^{fp}) at the focal plane. Due to rotational invariance, the longitudinal component, which is along the momentum direction of the incident proton, cannot be determined. (P_n^{fp}) and (P_t^{fp}) are measured by the azimuthal distribution of the events scattered from the secondary scatterer. The variation of the cross section is related to the polarization observables at the focal plane, (P_n^{fp}) and (P_t^{fp}) by the functional form:

$$\sigma^{\pm}(\theta_{fpp}, \phi_{fpp}, T) = \sigma_0^{\pm}(\theta_{fpp}, T)[1 + A_c(\theta_{fpp}, T)\,((P_t^{fp})\sin\phi_{fpp} - (P_n^{fp})\cos\phi_{fpp})]. \tag{1.13}$$

Here, σ^+ and σ^- are the azimuthal angle distributions of the protons rescattered in the analyzer corresponding to helicity + and helicity - electrons respectively, while σ_0^+ and σ_0^- are the total number of rescattered protons for + and - helicity

state respectively. By fitting this functional form in the equation below to the $\sigma^{\pm}$ distribution, one can determine (P_n^{fp}) and (P_t^{fp}) at the focal plane. Then knowing how the spin precesses when the proton travels through the magnetic elements of the spectrometer, one can generally determine all three components of the final state polarizations at the target. This procedure is described in more detail in Chapter 5.

For the determination of the polarization observables from the focal plane asymmetries, a favorable value for the spin precession angle χ has to be chosen. For illustrative purposes, consider the simple dipole case (where the spectrometer is approximated to a pure dipole), in which the polarization observables at the target are related to the focal plane asymmetries by

$$P_t' = \frac{(b)_{difference}}{A_c h} \tag{1.14}$$

$$P_l' = \frac{(a)_{difference}}{A_c\, h \sin\chi} \tag{1.15}$$

$$P_n = \frac{(a)_{sum}}{A_c\, h \cos\chi}. \tag{1.16}$$

Here a and b are the coefficients of the $\sin\phi_{fpp}$ and $\cos\phi_{fpp}$ terms of the ϕ_{fpp} distributions respectively. For the polarization transfer observables, sin χ should be as large as possible. However, this was not much of a problem for us since in our case $\chi \sim 117^0$, which gives a value of 0.89, close to the maximum of 1, making the focal plane asymmetries large, thereby reducing the statistical uncertainties.

1.5 The present experiment.

This thesis discusses the data for the polarization-transfer observables (P_t' and P_l') from Jefferson Lab experiment E89033 [20]. The induced polarization (P_n) results will be discussed in another thesis [21]. This experiment used the recoil polarization technique for the first time to look for medium modification effects in a complex nucleus. Comparison of H and ^{16}O data taken from the same setup and at the same

kinematics, allows for a cleaner interpretation. The measurement was performed at $Q^2 = 0.8$ (GeV/c)^2 and at quasielastic, perpendicular kinematics. The kinematics for the experiment are detailed below.

- Throughout the experiment,
  - The beam energy was 2.445 GeV.
  - The electron spectrometer was at θ_e =23.4^0.
    - central value of energy transfer, ω = 430 MeV, and momentum transfer, q=1000 MeV/c.
- H$(\vec{e}, e'\vec{p})$ calibration data

Kinematic setting	θ_{pq}
parallel	0^0
85 MeV/c pmiss of ^{16}O	3.2^0

- ^{16}O$(\vec{e}, e'\vec{p})$ production data

Kinematic setting	θ_{pq}
85 MeV/c pmiss	3.2^0
140 MeV/c pmiss	7.9^0

Here θ_{pq} is the angle between the $\vec{q}$ and the outgoing proton momentum, and pmiss is the nucleon initial momentum in the simplistic Plane Wave Impulse Approximation (PWIA) case. These are defined in Chapter 3.

Chapter 2

The reaction A $(\vec{e}, e'\vec{p})$ B.

In this chapter we will discuss the formalism for coincident polarized electron scattering. We will obtain the differential cross section in terms of 18 independent response functions and relate individual polarization observables for a complex nucleus at the target to the particular response functions. Then we will discuss the individual polarizations and how they are related to the electromagnetic form factors for the simple case of a free proton. This relationship allows us to obtain an experimental value for $\mu \frac{G_E}{G_M}$ (which goes to 1 as Q2 goes 0) for the free proton. The impact on the extracted response functions from the use of the Plane Wave Impulse Approximation (PWIA) and the Distorted Wave Impulse Approximation (DWIA) is also discussed in this chapter.

Exclusive experiments go beyond their inclusive counterparts in that they provide important additional information which is unavailable when only the scattered electron is detected. In exclusive reactions we focus on a particular final state channel corresponding to the particle detected in coincidence with the scattered electron. The reaction A($\vec{e}$,e'$\vec{p}$)B, where polarized electrons are used to eject polarized protons from an unpolarized target, has several advantages over an unpolarized reaction:

1. The additional measurable quantities are discrete spin degrees of freedom which can be accessed by providing a polarized electron beam and using a polarimeter

for the ejected proton.

2. The discreteness of the spin degrees of freedom in polarization transfer to an ejected proton allows one to minimize systematic uncertainties (experimentally) by allowing all of the continuous kinematical variables to be fixed while the spin of the beam is flipped.

3. The A($\vec{e}$,e'$\vec{p}$)B reaction allows one to gain more information about the nuclear response in trying to understand the electromagnetic structure of the nucleus.

4. From the theoretical standpoint, the ($\vec{e}$,e'$\vec{p}$) reaction provides direct access to the spin response of the nuclear system, which is important since the strong interaction of the nuclear system as well as the electromagnetic interaction of the electrons with the hadrons in the nucleus are explicitly spin dependent.

5. The spin-dependent response functions can impose more severe constraints on theoretical models of quasielastic electron scattering.

2.1 Formalism.

The formalism for polarization in exclusive electron scattering from a nucleus, A($\vec{e}$,e'$\vec{p}$)B, was originally developed by several authors including Picklesimer and Van Orden [22], Raskin and Donnelly [23], and Giusti and Pacati [24].

Since the electromagnetic interaction is relatively weak, we only need to consider the one photon exchange approximation. The diagram relevant for this reaction, where the ejected proton polarization is also detected, is shown in Figure 2.1.

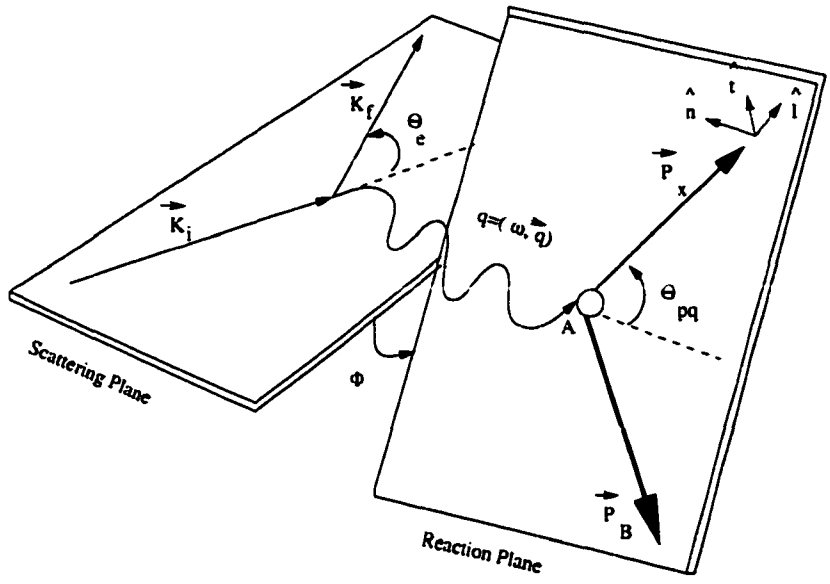

Figure 2.1: Kinematic definitions for A($\vec{e}$,e'$\vec{p}$)B reaction.

In Figure 2.1, $k_i = (E_i, \vec{k_i})$ and $k_f = (E_f, \vec{k_f})$ are the initial and final electron four momenta, and q = $k_i - k_f = (\omega, \vec{q})$ is the momentum transfer carried by the virtual photon. The detected proton emerges with momentum p_x $(E_x, \vec{p_x})$ at an angle θ_{pq} with $\vec{q}$, leaving the residual nucleus with recoil momentum, $\vec{p_B} = \vec{q} - \vec{p_x}$. There are two planes of interest in this figure: the scattering plane which is defined by the incoming and the scattered electron momenta, $\vec{k_i}$, $\vec{k_f}$, and the reaction plane which is defined by the momentum of the ejected proton $\vec{p_x}$ and the momentum of the virtual photon $\vec{q}$. $\vec{p_B}$ also lies in the reaction plane along with the recoiling A-1 nuclear system. The azimuthal angle, ϕ is the angle between the scattering plane and the reaction plane. In coplanar kinematics ϕ is either 180^0 or 0^0. In both experiment and theory we define $\phi = 180^0$ when $\theta_{pq} < 0$. Both θ_{pq} and ϕ play an important role in comparing experimental results which are obtained for a finite acceptance to theory which is normally given for a point acceptance (this is discussed in more detail in Chapter 6).

The missing momentum $\vec{p}$miss is defined as the negative of the recoil momentum, $\vec{p}$miss = $-\vec{p}_{recoil} = -\vec{p}_B$. In the case of the Plane Wave Impulse Approximation

(PWIA) $\vec{pmiss}$ is the proton momentum when it is struck inside the nucleus. In coplanar quasi-perpendicular kinematics (discussed below) as in the case of this experiment, positive missing momenta are obtained for $\theta_{pq} > 0$ or $\phi = \pi$. In this thesis we present results for two positive missing momenta (pmiss) settings of 85 MeV/c and 140 MeV/c.

As shown in the Figure 2.1, the three components of the polarization for the outgoing proton at the target are expressed in the $(\vec{t}, \vec{n}, \vec{l})$ helicity basis (baricentric) where $\vec{l}$ is in the direction of the proton momentum $P_x, \vec{n}$ is perpendicular to the reaction plane ($\vec{n}$ is vertically down for positive missing momenta as in our case) and $\vec{t} = \vec{n} \times \vec{l}$.

In $(e, e'p)$ experiments, two types of kinematical conditions, shown in Fig 2.2, are often utilized. In parallel kinematics the ejected proton momentum is parallel to $\vec{q}$ so that the missing momentum is positive for $p_x >$ q or negative for $p_x <$ q. In the case of a Hydrogen target there is no missing momentum (two body kinematics, $p_x =$ q), so this is essentially parallel kinematics data. In quasi-perpendicular kinematics the magnitude of the ejected nucleon momentum is close to $|\vec{q}|$; ($p_x \approx$ q and is kept constant while varying θ_{pq} within a small range around 0^0). In such cases $\vec{pmiss}$ is almost perpendicular to both $\vec{q}$ and $\vec{p_x}$. One advantage of this kinematic setting is that the FSI of the proton with the residual nucleus will be the same for different $\vec{p}_{miss}$ values since the proton momentum is held constant. Our ^{16}O data were obtained in quasi-perpendicular kinematics.

The invariant scattering cross section for the coincidence reaction shown in Figure 2.1 above can be expressed in the lab frame, following the Bjorken and Drell [25] conventions,

$$d\sigma = \frac{1}{\beta} N_i N_A \bar{\sum_i} \sum_f |M_{fi}|^2 N_f \frac{d^3k_f}{(2\pi)^3} \left(\prod_{j=1}^{n} N_j \frac{d^3p_j}{(2\pi)^3} \right) (2\pi)^4 \delta^4(p_f - q - p_A). \quad (2.1)$$

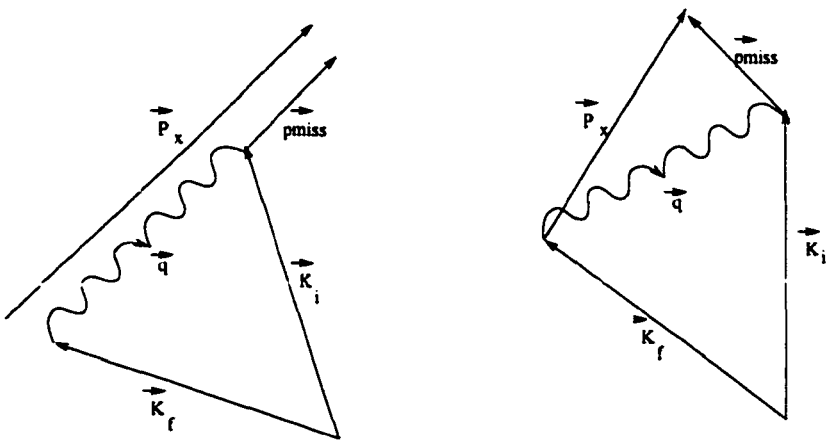

Figure 2.2: Kinematical conditions, parallel (left) and quasi-perpendicular (right).

Here β is the relative velocity for collinear collisions which is almost unity, $\bar{\sum}_i$ denotes an average over initial states and $\sum_f$ denotes a sum over final states. p_j, j=1, n gives the number of hadrons detected in the phase space. n=1+number of hadrons, and $p_f = \sum_i^n p_j$. Here, using the Bjorken normalization, N =m/ϵ for hadrons or N = $1/2\epsilon$ for massless electrons (here m stands for mass and ϵ stands for total energy). In the One Photon Exchange (OPE) approximation, the invariant matrix element M_{fi} can be factorized into an electron tensor and a nuclear tensor as follows,

$$M_{fi} = \frac{4\pi\alpha}{Q^2} < k_f\lambda_f|j_\mu|k_i\lambda_i >< B_f\vec{p_x}|j^\mu|A_i > . \tag{2.2}$$

Here α is the fine structure constant, $Q^2 = \vec{q^2} - \omega^2$ is the space-like invariant mass of the virtual photon, λ_i, λ_f are the initial and final spinors of the electron, and A_i, B_f are the initial and final states of the nucleon including the spinors.

After some steps the cross section becomes

$$d\sigma = (2\pi)^{-3}\frac{E_f}{E_i}\frac{\alpha^2}{Q^4}\eta_{\mu\nu}\omega^{\mu\nu}dE_f d\Omega_e d^3p_x. \tag{2.3}$$

Here $\eta_{\mu\nu}$ and $\omega^{\mu\nu}$ are the electron tensor and the nuclear response tensor (which carries all the information about the electromagnetic properties of the target) respectively, and Ω_e is the solid angle for the scattered electron.

By substituting

$$d^3p_x = E_x p_x dE_x d\Omega_x. \tag{2.4}$$

the six-fold differential cross section becomes

$$\frac{d^6\sigma}{dE_f d\Omega_e dE_x d\Omega_x} = \frac{p_x E_x}{(2\pi)^3}\frac{E_f}{E_i}\frac{\alpha^2}{Q^4}\eta_{\mu\nu}\omega^{\mu\nu}. \tag{2.5}$$

For exclusive reactions this reduces to a five-fold differential cross section since the target is excited to a single discrete state (a peak in the missing energy spectrum). After defining a recoil factor R,

$$R = \int dE_x \delta(E_x + E_B - \omega = m_A) = \left|1 - \frac{E_x}{E_B}\frac{\vec{p_x}\cdot\vec{p_B}}{\vec{p_x}\cdot\vec{p_x}}\right|^{-1}. \tag{2.6}$$

we have

$$\frac{d^5\sigma}{dE_f d\Omega_e d\Omega_x} = R\frac{p_x E_x}{(2\pi)^3}\frac{E_f}{E_i}\frac{\alpha^2}{Q^4}\eta_{\mu\nu}\omega^{\mu\nu}. \tag{2.7}$$

2.1.1 Electron response tensor.

In the case of polarized incident electrons, the electron tensor consists of two parts: an unpolarized symmetric, real part $\eta^u_{\mu\nu}$ and a helicity-dependent anti-symmetric, imaginary part $\eta^h_{\mu\nu}$. The formalism was first developed by Dombey [26].

$$\eta_{\mu\nu} = \frac{1}{2}[\eta^u_{\mu\nu} + \eta^h_{\mu\nu}]. \tag{2.8}$$

Note that in the extreme relativistic limit, only the longitudinal part of the polarization of the incident electrons is important since the contribution due to the transverse component is suppressed by a factor γ (see [26] for details). Therefore here we are considering only the longitudinal part of the electron helicity (projection of the polarization along the direction of the momentum) h.

The helicity independent and dependent terms of the electron tensor are given by the following equations:

$$\eta^u_{\mu\nu} = k_\mu k_\nu - q_\mu q_\nu - Q^2 g_{\mu\nu} \tag{2.9}$$

$$K = k_i + k_f \tag{2.10}$$

$$\eta^h_{\mu\nu} = -i\varepsilon_{\mu\nu\alpha\beta} q_i^\alpha K_f^\beta. \tag{2.11}$$

Here $\varepsilon_{\mu\nu\alpha\beta}$ is the completely antisymmetric Levi-Civita tensor.

2.1.2 Nuclear Response Tensor.

The nuclear response tensor can be decomposed into two parts, a symmetric part $W_S^{\mu\nu}(\hat{S}'_R)$ and an anti-symmetric part $W_A^{\mu\nu}(\hat{S}'_R)$

$$W^{\mu\nu}(\hat{S}'_R) = W_S^{\mu\nu}(\hat{S}'_R) + W_A^{\mu\nu}(\hat{S}'_R). \tag{2.12}$$

Here $\hat{S}'_R$ is the rest frame spin vector of the ejectile.

Furthermore, after imposing the constraint of parity invariance, this $(\vec{e},e'\vec{N})$ electro-production tensor can be written in terms of 18 independent tensor elements:

$$\begin{aligned} W_S^{\mu\nu}(\hat{S}'_R) =& (W_1^u + W_1^N \hat{n}\cdot\hat{S}'_R)G^{\mu\nu} + (W_2^u + W_2^N \hat{n}\cdot\hat{S}'_R)V_i^\mu V_i^\nu + (W_3^u + W_3^N \hat{n}\cdot\hat{S}'_R)V_j^\mu V_j^\nu \\ &+ (W_4^u + W_4^N \hat{n}\cdot\hat{S}'_R)[V_i^\mu V_f^\nu]_S + (W_5^t \hat{t}\cdot\hat{S}'_R + W_5^l \hat{l}\cdot\hat{S}'_R)[V_i^\mu \xi^\nu]_S \\ &+ (W_6^t \hat{t}\cdot\hat{S}'_R + W_6^l \hat{l}\cdot\hat{S}'_R)[V_f^\mu \xi^\nu]_S \end{aligned} \tag{2.13}$$

$$\begin{aligned} W_A^{\mu\nu}(\hat{S}'_R) =& (W_7^u + W_7^N \hat{n}\cdot\hat{S}'_R)[V_i^\mu V_f^\nu]_A + (W_8^t \hat{t}\cdot\hat{S}'_R + W_8^l \hat{l}\cdot\hat{S}'_R)[\xi^\mu V_i^\nu]_A \\ &+ (W_9^t \hat{t}\cdot\hat{S}'_R + W_9^l \hat{l}\cdot\hat{S}'_R)[\xi^\mu V_f^\nu]_A. \end{aligned} \tag{2.14}$$

Here $\hat{n}$, $\hat{l}$ and $\hat{t}$ were defined in Figure 2.1. The W's are defined in the next

section, and V_i, V_f and ξ^μ are defined as follows:

$$V_i = p_A - \frac{\vec{p_A} \cdot \vec{q}}{q^2} q \tag{2.15}$$

$$V_f = p_x - \frac{\vec{p_x} \cdot \vec{q}}{q^2} q \tag{2.16}$$

$$\bar{V_f} = V_f - \frac{\vec{V_f} \cdot \vec{V_i}}{V_i^2} V_i \tag{2.17}$$

$$\xi^\mu = \varepsilon_{\mu\nu\rho\sigma} q_\nu (\bar{V_f})_\rho (V_i)_\sigma. \tag{2.18}$$

2.1.3 18 independent response functions.

Now combining the electron and the nuclear tensors,

$$\eta_{\mu\nu} W^{\mu\nu}(\hat{S_R}') = \eta^S_{\mu\nu} W_S^{\mu\nu}(\hat{S_R}') + \eta^A_{\mu\nu} W_A^{\mu\nu}(\hat{S_R}') \tag{2.19}$$

$$= \Sigma_S + \Sigma_A. \tag{2.20}$$

The contraction of the symmetric part Σ_S depends on only four components (in the lab frame)

1. $W_S^{00}(\hat{S_R}')$
2. $W_S^{11}(\hat{S_R}') + W_S^{22}(\hat{S_R}')$
3. $W_S^{11}(\hat{S_R}') - W_S^{22}(\hat{S_R}')$
4. $W_S^{02}(\hat{S_R}') + W_S^{20}(\hat{S_R}')$

Due to the anti-symmetric nature of $\eta_A^{\mu\nu}$, the only components needed to construct Σ_A are

1. $W_A^{10}(\hat{S_R}') - W_A^{01}(\hat{S_R}')$
2. $W_A^{12}(\hat{S_R}') - W_A^{21}(\hat{S_R}')$

These again can be expressed in terms of a set of 18 independent response functions, R_i (for the case where the final state of the system is specified) by the following set of equations,

$$R_L + R_L^N \hat{n} \cdot \hat{S_R}' = W^{00}(\hat{S_R}') \tag{2.21}$$

$$R_T + R_T^N \hat{n} \cdot \hat{S_R}' = W^{11}(\hat{S_R}') + W^{22}(\hat{S_R}') \tag{2.22}$$

$$(R_{TT} + R_{TT}^N \hat{n} \cdot \hat{S_R}')\cos 2\phi + (\mathrm{R_{TT}^T}\hat{t} \cdot \hat{\mathrm{S_R}}' + \mathrm{R_{TT}^L}\hat{l} \cdot \hat{\mathrm{S_R}}')\sin 2\phi = W^{22}(\hat{S_R}') - W^{11}(\hat{S_R}') \tag{2.23}$$

$$(R_{LT} + R_{LT}^N \hat{n} \cdot \hat{S_R}')\sin\phi + (\mathrm{R_{LT}^T}\hat{t} \cdot \hat{\mathrm{S_R}}' + \mathrm{R_{LT}^L}\hat{l} \cdot \hat{\mathrm{S_R}}')\cos\phi = W^{02}(\hat{S_R}') + W^{20}(\hat{S_R}') \tag{2.24}$$

$$(R'_{LT} + R'^N_{LT} \hat{n} \cdot \hat{S_R}')\cos\phi + (\mathrm{R'^T_{LT}}\hat{t} \cdot \hat{\mathrm{S_R}}' + \mathrm{R'^L_{LT}}\hat{l} \cdot \hat{\mathrm{S_R}}')\sin\phi = i(W^{10}(\hat{S_R}') - W^{01}(\hat{S_R}')) \tag{2.25}$$

$$(R_{TT}^T \hat{t} \cdot \hat{S_R}' + R_{TT}^L \hat{l} \cdot \hat{S_R}' = i(W^{12}(\hat{S_R}') - W^{21}(\hat{S_R}')). \tag{2.26}$$

Here the subscripts on R refer to the components of the virtual photon polarization, primes denote helicity dependent polarizations, superscripts denote the ejectile polarization vector components. These response functions are independent of the azimuthal angle ϕ and depend only on $|\vec{p_x}|$, θ, $|\vec{q}|$ and ω. It had been shown [27] that the response functions become smaller as Q^2 increases, mostly due to the Q^2 dependence of the electromagnetic form factors of the nucleon. These 18 independent response functions completely determines the hadronic tensor. 13 of these response functions depend on the ejectile spin. Thus, for a complete determination of the nuclear response, one needs to study the polarization of the ejectile.

2.1.4 Differential cross section for the reaction A($\vec{e}$,e'$\vec{N}$)B.

Now we can combine the response functions to write the differential cross section for the coincidence reaction A($\vec{e}$,e'$\vec{N}$)B when the detected ejectile is a spin

1/2 particle

$$\frac{d^3\sigma}{dE_f d\Omega_e d\Omega_x} = \frac{m_N|\vec{p_x}|}{2(2\pi)^3}\left[\frac{d\sigma}{d\Omega_f}\right]_{mott}$$
$$[V_L(R_L + R_L^N\hat{S}_n) + V_T(R_T + R_T^N\hat{S}_n)$$
$$+ V_{TT}[(R_{TT} + R_{TT}^N\hat{S}_n)\cos 2\phi + (\mathrm{R_{TT}^T\hat{S}_t} + \mathrm{R_{TT}^L\hat{S}_l})\sin 2\phi]$$
$$+ V_{LT}[(R_{LT} + R_{LT}^N\hat{S}_n)\cos\phi + (\mathrm{R_{LT}^T\hat{S}_t} + \mathrm{R_{LT}^L\hat{S}_l})\sin\phi]$$
$$+ hV'_{LT}[(R'_{LT} + R'^N_{LT}\hat{S}_n)\sin\phi + (\mathrm{R'^T_{LT}\hat{S}_t} + \mathrm{R'^L_{LT}\hat{S}_l})\cos\phi]$$
$$+ hV'_{TT}(R'^T_{TT}\hat{S}_t + R'^L_{TT}\hat{S}_l)]. \tag{2.27}$$

Here $\hat{S}_i$ are the projections of the spin unit vector onto the basis vectors $\hat{n}, \hat{l}, \hat{t}$ as defined in Figure 2.1. The Mott cross section and the V terms depend solely on the electron kinematics as defined below:

$$(\frac{d\sigma}{d\Omega_f})_{mott} = \frac{\alpha^2\cos^2\theta_e/2}{4\mathrm{E_i^2}\sin^4\theta_e/2} \tag{2.28}$$
$$V_L = \frac{Q^4}{q^4} \tag{2.29}$$
$$V_T = \frac{Q^2}{2q^2} + \tan^2\theta_e/2 \tag{2.30}$$
$$V_{LT} = \frac{Q^2}{q^2}[\frac{Q^2}{q^2} + \tan^2\theta_e/2]^{1/2} \tag{2.31}$$
$$V_{TT} = \frac{Q^2}{2q^2} \tag{2.32}$$
$$V'_{LT} = \frac{Q^2}{q^2}\tan\theta_e/2 \tag{2.33}$$
$$V'_{TT} = [\frac{Q^2}{q^2} + \tan^2\theta_e/2]^{1/2}\tan\theta_e/2. \tag{2.34}$$

2.1.5 Polarization Observables.

Bound nucleon.

The differential cross-section for a coincidence $(\vec{e},e'\vec{N})$ reaction in which the ejectile polarization is measured was given in the previous section. This cross-section can be written in terms of an unpolarized cross-section and recoil polarization observables using the formalism developed by J.W. Van Orden and A. Picklesimer [22] and C. Giusti and F.D. Pacati [24]:

$$\frac{d^6\sigma}{dE_f d\Omega_e dE_x d\Omega_x} = \frac{\sigma_0}{2}[1 + \vec{P}\cdot\hat{S}_x{}' + h(A + \vec{P}'\cdot\hat{S}_x{}')]. \tag{2.35}$$

Here σ_0 is the unpolarized cross-section, A is the beam analyzing power which can be measured only by an out-of-plane measurement, $\vec{P}$ are the induced polarizations, $\vec{P}'$ are the polarization-transfer coefficients and h is the longitudinal beam polarization.

We can think of the polarization of the ejectile (Π) as constituting of two parts: a helicity dependent part, $(\vec{P}')$ and a helicity independent part, $(\vec{P})$, where

$$\vec{\Pi} = \vec{P} + h\vec{P}' \tag{2.36}$$

$$\vec{P} = \vec{P}_n + \sum_{m=l,t} \vec{P}_m \tag{2.37}$$

$$\vec{P}' = \vec{P}'_n + \sum_{m=l,t} \vec{P}'_m. \tag{2.38}$$

Here, m can be either t or l. Comparison of Equations 2.27 and 2.35 gives

$$\sigma_0 = K\sigma_M(V_L R_L + V_T R_T + V_{TT} R_{TT}\cos 2\phi + \mathrm{V_{LT}R_{LT}}\cos\phi) \quad (2.39)$$

$$\sigma_0 P_n = K\sigma_M(V_L R_L^N + V_T R_T^N + V_{TT} R_{TT}^N \cos 2\phi + \mathrm{V_{LT}R_{LT}^N}\cos\phi) \quad (2.40)$$

$$\sigma_0 P_m = K\sigma_M(V_{TT} R_{TT}^m \sin 2\phi + \mathrm{V_{LT}R_{LT}^m}\sin\phi) \quad (2.41)$$

$$\sigma_0 P_n' = K\sigma_M(V_{LT}' R_{LT}'^N \sin\phi) \quad (2.42)$$

$$\sigma_0 P_m' = K\sigma_M(V_{LT}' R_{LT}'^m \cos\phi + \mathrm{V'_{TT}R'^m_{TT}}). \quad (2.43)$$

Here σ_M is the Mott cross-section, $K = \frac{p_z E_z}{(2\pi)^2}$, P_n, P_n' are normal to the hadronic reaction plane, P_m, P_m' are on the hadronic reaction frame, P_l' is along the direction of the ejectile momentum and P_t' is transverse to that. The V's were defined in the previous section.

In the case of in-plane kinematics ($\phi = 0^0$ or 180^0), only 3 of the polarizations will survive:

$$\sigma_0 P_N = K\sigma_M(V_L R_L^N + V_T R_T^N + V_{TT} R_{TT}^N \pm V_{LT} R_{LT}^N \quad (2.44)$$

$$\sigma_0 P_l' = K\sigma_M(\pm V_{LT}' R_{LT}'^L + V_{TT}' R_{TT}'^L) \quad (2.45)$$

$$\sigma_0 P_t' = K\sigma_M(\pm V_{LT}' R_{LT}'^T + V_{TT}' R_{TT}'^T). \quad (2.46)$$

Here +(-) corresponds to $\phi = 0^0(180^0)$.

This is mostly the case for one of the kinematic settings of this experiment (pmiss = 140 MeV/c). However at the 85 MeV/c setting, since the $\vec{q}$ vector was within the acceptance, there was a considerable out-of-plane contribution. In that situation we have to take into account the mixing of other polarization observables which become non-zero when ϕ goes out-of-plane. This is discussed in detail in Chapter 6.

Free nucleon.

In the case of a free nucleon there is no recoiling system and the reaction is always co-planer. This makes the kinematics much simpler (elastic scattering from a stationary nucleon). The derivation of the polarization observables for the free nucleon case was first done by Akhiezer and Rekalo [29], and discussed in more detail by R.G. Arnold, C.E. Carlson and F. Gross in 1980 [30]. A review of this derivation is also available in [31].

The only non-zero polarizations for this case are the two polarization-transfer observables, P_l' and P_t' which are accessible only when the incident electron beam is polarized. They can be written in terms of the Sachs form factors G_E and G_M

$$P_l' = \frac{E_i + E_f}{M_N} \frac{[\tau(1+\tau)]^{1/2} G_M^2 \tan^2\theta_e/2}{G_E^2 + G_M^2 \tau(1 + 2(1+\tau)\tan^2\theta_e/2)} \tag{2.47}$$

$$P_t' = -\frac{2[\tau(1+\tau)]^{1/2} G_M G_E \tan\theta_e/2}{G_E^2 + G_M^2 \tau(1 + 2(1+\tau)\tan^2\theta_e/2)}. \tag{2.48}$$

Here θ_e is the electron scattering angle, E_i is the incident electron energy, E_f is the scattered electron energy and M_N is the nucleon mass. These polarizations are also defined in the baricentric reaction frame. The form factor ratio for the free nucleon, G_E/G_M is thus directly related to the ratio of the polarization-transfer observables P_t'/P_l' as follows:

$$\frac{G_E}{G_M} = \frac{P_t'}{P_l'} \frac{(E_i + E_f)}{2M_N} \tan\theta_e/2. \tag{2.49}$$

Thus the value of μ times the ratio, $\mu G_E/G_M$, can be determined explicitly for the free proton by measuring the ratio, P_t'/P_l'. The beam polarization and the analyzing power of the secondary scatterer (which are described later) cancels in the calculation of G_E/G_M. Because P_l' and P_t' are measured from the asymmetry of the normalized difference distributions of positive and negative helicity events (this is also described in detail later), measured simultaneously, absolute normalization of

the beam and target system is also not relevant. In fact the systematic uncertainties in the measurement of G_E/G_M using recoil polarimetry are reduced greatly compared to a Rosenbluth separation technique. Therefore this is a cleaner way of measuring the form factor ratio for the free proton. Since there exist only two polarization observables there is no possibility of mixing from other components when dealing with the finite acceptance of a spectrometer.

The knowledge of the form factor ratio for the free nucleon is extremely important for the evaluation of models of nucleon structure. Lack of knowledge of the free value of G_E/G_M will directly affect the calculations or predictions for the bound proton. Since the goal of this experiment is to observe any medium modification effects on the form factors, we need to know how the proton form factors behave in free space for the comparison. This is discussed in more detail in the next chapter. Fortunately, since we had a waterfall target, we could obtain the free form factor values (at the same value of Q^2 as the ^{16}O data) from the H data taken. This result will be compared with the available theoretical predictions and with a more precise measurement performed later [124] in Chapter 5.

2.2 Plane Wave Impulse Approximation.

The Plane Wave Impulse Approximation (PWIA) is the simplest framework that can be used to calculate scattering amplitudes for complex nuclei. PWIA provides a reasonable approximation especially in the case of quasielastic kinematics. However, the PWIA does not predict the normal component of the polarization correctly since distortions due to final state interactions are not taken in to account by the PWIA calculations. The A($\vec{e}$,e'$\vec{p}$)B reaction in the PWIA is shown in Figure 2.3.

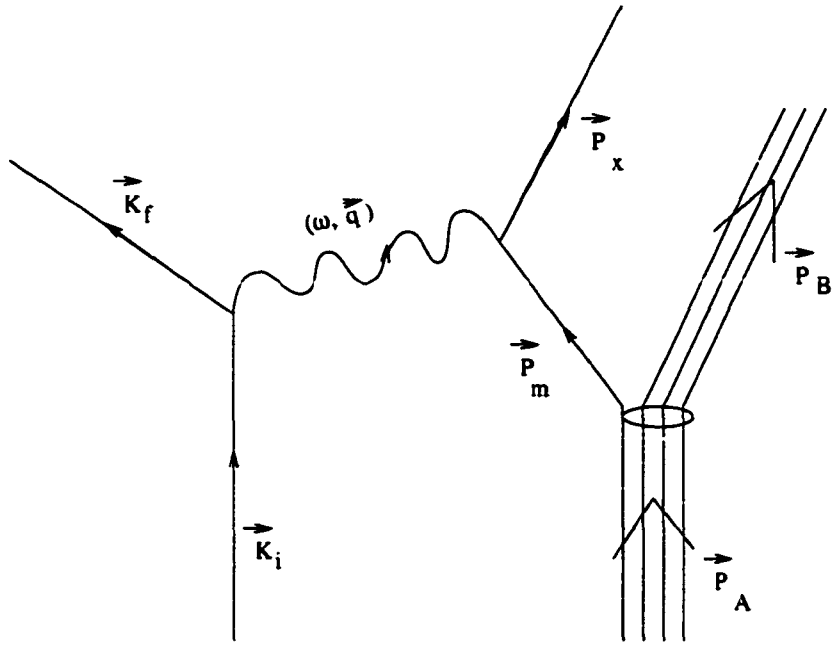

Figure 2.3: Kinematics for PWIA for A($\vec{e}$,e'$\vec{p}$)B reaction.

The following are the assumptions made in PWIA:

- A single virtual photon $(\omega, \vec{q})$ is absorbed completely by one nucleon.
- The struck nucleon leaves the nucleus without interacting with the rest of the nucleus (spectator model). Therefore the outgoing nucleon can be described by a plane wave.
- The nucleus can be described by an independent particle model (one assumes a mean field such as a Hartree-Fock, for the nucleus).

In the non relativistic PWIA, the cross section can be further factorized into a single nucleon part and a part describing the rest of the nucleus:

$$\frac{d\sigma}{dE_f d\Omega_e dE_x d\Omega_x} = K\sigma_{ex} S(E_m, pmiss). \tag{2.50}$$

Here K is a phase space factor same as in Eq. 2.39 and σ_{ex} is the half-off-shell electron-proton cross section, related to the struck nucleon rather than to the full nucleus. S is the spectral function and gives the probability that a nucleon with initial momentum p_i and binding energy E_m can be removed from a target of initial state A leaving it in a final state B. The missing momentum $\vec{pmiss}$ and missing energy (binding energy) E_m are defined as

$$\vec{pmiss} = \vec{p_x} - \vec{q} \tag{2.51}$$

$$E_{miss} = \omega - T_x - T_B. \tag{2.52}$$

Here T_x and T_B are the final kinetic energies of the nucleon and the residual nucleus respectively. In the PWIA, the initial momentum of the struck nucleon, $\vec{p_i}$, is equal to the missing momentum $pmiss$. The conservation of energy and momentum requires

$$E_{miss} = \omega - T_x - T_B = M_B + M_x - M_A \tag{2.53}$$

$$\vec{p_i} = \vec{p_x} - \vec{q} = \vec{pmiss} = -\vec{P_B}. \tag{2.54}$$

In the non relativistic PWIA the 18 independent response functions are given by the following set of equations [28]

$$R_L = F_1^2(Q^2) n_{nlj}(|\vec{p_x} - \vec{q}|) \tag{2.55}$$

$$R_L^N = 0 \tag{2.56}$$

$$R_T = [F_1^2(Q^2) \frac{\vec{p}_x^2}{M^2 \sin^2\theta_{pq} + G_M^2(Q^2) \frac{\vec{q}^2}{2M_N^2}}] n_{nlj}(|\vec{p_x} - \vec{q}|) \tag{2.57}$$

$$R_T^N = 0 \tag{2.58}$$

$$R_{TT} = F_1^2(Q^2) \frac{\vec{p}_x^2}{M_N^2} \sin^2\theta_{pq} n_{nlj}(|\vec{p_x} - \vec{q}|) \tag{2.59}$$

$$R_{TT}^N = R_{TT}^L = R_{TT}^T = 0 \tag{2.60}$$

$$R_{LT} = -2F_1^2(Q^2) \frac{\vec{p}_x}{M_N} \sin^2\theta_{pq} n_{nlj}(|\vec{p_x} - \vec{q}|) \tag{2.61}$$

$$R_{LT}^N = R_{LT}^L = R_{LT}^T = 0 \tag{2.62}$$

$$R'_{LT} = 0 \tag{2.63}$$

$$R'^N_{LT} = F_1^2(Q^2) G_M^2(Q^2) \frac{\vec{q}}{M_N} n_{nlj}(|\vec{p_x} - \vec{q}|) \tag{2.64}$$

$$R'^L_{LT} = -F_1^2(Q^2) G_M^2(Q^2) \frac{\vec{q}}{M_N} \sin\theta_{pq} n_{nlj}(|\vec{p_x} - \vec{q}|) \tag{2.65}$$

$$R'^T_{LT} = -F_1^2(Q^2) G_M^2(Q^2) \frac{\vec{q}}{M_N} \sin\theta_{pq} n_{nlj}(|\vec{p_x} - \vec{q}|) \tag{2.66}$$

$$R'^L_{TT} = [G_M^2(Q^2) \frac{\vec{q}^2}{2M_N^2} \cos\theta_{pq} + F_1^2(Q^2) G_M^2(Q^2) \frac{|\vec{p}_x||\vec{q}|}{M_N^2} \sin^2\theta_{pq}] n_{nlj}(|\vec{p_x} - \vec{q}|) \tag{2.67}$$

$$R'^T_{TT} = [-G_M^2(Q^2) \frac{\vec{q}^2}{2M_N^2} \sin\theta_{pq} + F_1^2(Q^2) G_M^2(Q^2) \frac{|\vec{p}_x||\vec{q}|}{2M_N^2} \sin 2\theta_{pq}] n_{nlj}(|\vec{p_x} - \vec{q}|). \tag{2.68}$$

Here n_{nlj} is the momentum density distribution for a nucleon in the nlj subshell, and $F_1(Q^2)$ is the nucleon Dirac form factor. As mentioned above, the expressions for the response functions, $R_L^N, R_T^N, R_{TT}^N, R_{LT}^N$ show that they go to zero in the PWIA limit, making the helicity-independent normal component of the polarization P_n identically equal to zero.

2.3 Distorted Wave Impulse Approximation.

The assumption that the ejected nucleon suffers no interactions with the residual nuclear system is not necessarily valid since the nucleons are strongly interacting particles. In the Distorted Wave Impulse Approximation (DWIA) these Final State Interactions (FSI) are taken into account while keeping the other assumptions made in the PWIA. The A($\vec{e}$,e'$\vec{p}$)B reaction in the DWIA case is shown in Figure 2.4. The usual approach to handle the distortions due to final state interactions is to model them with a complex optical potential. A brief discussion of the optical potentials used for the DWIA calculations discussed in this thesis is given in Chapter 3.

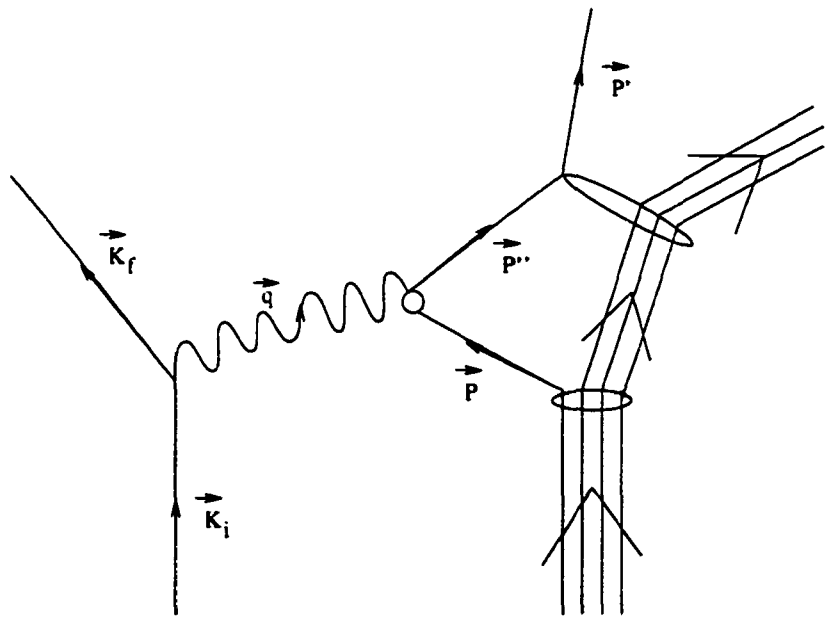

Figure 2.4: Kinematics for the DWIA for the A($\vec{e}$,e'$\vec{p}$)B reaction.

Due to the FSI the measured (asymptotic) value of the nucleon momentum is not equal to the nucleon momentum acquired just after the (e,e'p) reaction. Therefore the proton's initial momentum is not simply equal to the missing momentum.

The 18 independent response functions calculated in PWIA and DWIA for the $1p_{1/2}$ state of ^{16}O at a proton kinetic energy of 0.5 GeV, Q^2 of 1.0 (GeV/c)^2 and a

momentum transfer of 1 GeV/c are shown in Figures 2.5 and 2.6 Ref. [27]. These kinematics are very close to the kinematics of this thesis data.

The solid curves are the DWIA results using the Dirac eikonal formalism to account for the FSI and the dotted curves for the PWIA results. The dashed curve here gives the DWIA results without the spin-orbit potential. For the DWIA calculations a Hartree mean field wave function of the Walecka model [32] for the bound state proton was used. It is also noted that the results obtained using a partial wave formalism by J.W. Van Orden [22] agree with the eikonal approximation calculations to better than 10% (both calculations assume Höhler parameterization for the free values of the form factors). Again PWIA calculations give $R_L^N, R_T^N, R_{TT}^N, R_{LT}^N$ all identically equal to zero making P_n zero. The response functions that vanish in the PWIA case are quite sensitive to distorted wave effects or the optical potential used. Therefore different response functions are sensitive to different reaction mechanisms, allowing us to separately determine them. 0.43 fm^{-1} and 0.71 fm^{-1} $|p' - q|$ values in this figure correspond to 85 MeV/c and 140 MeV/c pmiss points of the present experiment respectively. The polarization response functions shown here will be used in the discussion on P_l' and P_t' obtained for point and full acceptance effects in Chapter 6.

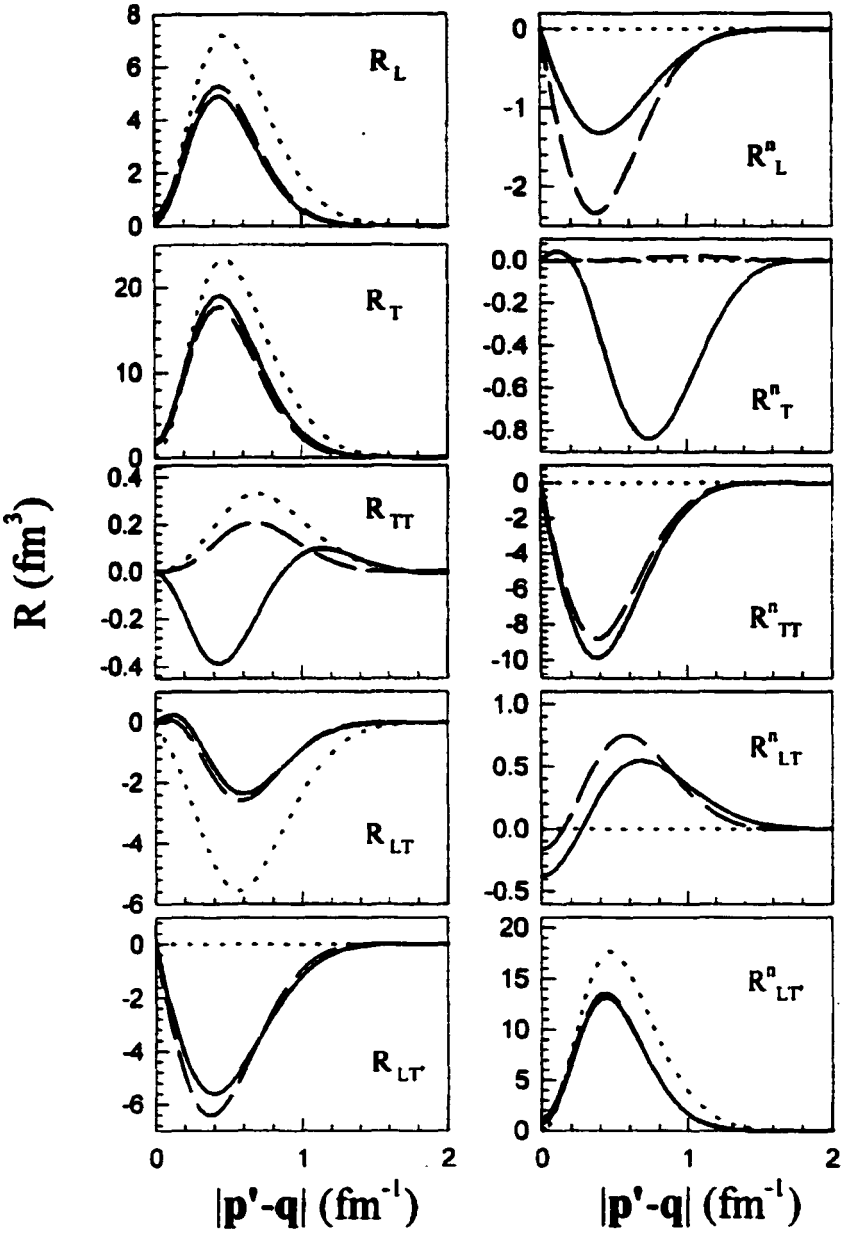

Figure 2.5: Comparison of response functions vs. missing momentum for the two cases PWIA and DWIA at kinematics close to those of this experiment, Reference [27]. The solid curves are the DWIA results using the Dirac eikonal formalism to account for the FSI and the dotted curves for the PWIA results. The dashed curves give the DWIA results without spin-orbit potential. All the calculations use the Höhler parameterization for the form factors, at Q^2=0.8(GeV/c)^2 this gives a value of 0.9 for the form factor ratio.

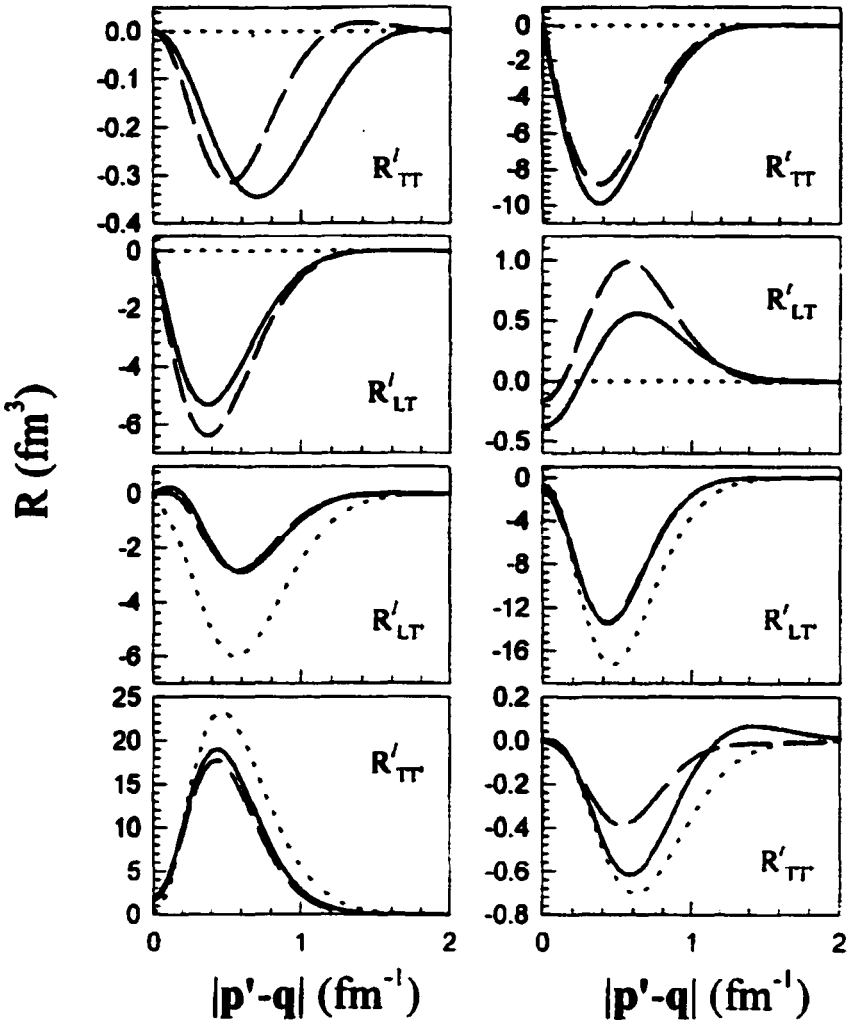

Figure 2.6: Same as in Figure 2.5, but for polarization response functions.

Chapter 3

Theoretical predictions and motivation.

In this chapter we discuss the theoretical calculations used to compare with the experimental results obtained from E89033. The DWIA calculations were performed by J.J. Kelly and J.W. Van Orden. Only a brief overview of these calculations is presented here. Since both the above mentioned calculations use the one body current operator, next we discuss two body currents. Since we are looking for medium modification effects on the form factor ratio for the proton, part of this chapter is devoted to the past experimental evidence supporting and opposing the idea of medium modifications. We conclude this chapter with more recent calculations performed by the Adelaide group on possible suppression of the form factor ratio on ^{16}O even at Q^2 of 0.8 $(GeV/c)^2$.

3.1 Non relativistic DWIA calculations by J.J. Kelly (LEA).

The computer program LEA (Linear Expansion Analysis) written and maintained by J.J. Kelly was used to perform acceptance-averaged non-relativistic DWIA

calculations for the kinematics of this experiment. Since the present experiment was performed at Bjorken x ($\frac{Q^2}{2m\omega}$) of 0.96, *i.e.*, in quasifree kinematics, the distorted wave impulse approximation using effective one-body operator is a good approximation.

Though LEA was originally used for the scattering off of nucleons by nuclei, it has been modified for electron scattering off nucleons. LEA is based on a non-relativistic Schrödinger formalism.

Single Nucleon Overlap function.

The single nucleon overlap function used in LEA is described by an eigen function of the mean field (Hartree-Fock) of the residual nucleus. A Woods-Saxon potential is used with a Perey factor (Perey factor is used to account for the non-locality nature of the nuclear mean field) which can be modified according to the radius and the width of the potential well. Both long-range and short-range correlations are accounted by the quasi-particle Hamiltonian model of Ma and Wamback [34] [35]. For these calculations the single particle wave functions were adjusted to reproduce the p shell ^{16}O(e,e'p) data of Leuschner *et al.* [36]. It should be noted that the effects of long-range and short-range correlations are minimal for the valence states we are interested in and for the modest size of missing momentum we are dealing with in this experiment.

One has to convolute the theory with the effects due to the nuclear medium before comparing to data. Namely, one has to take into account electron distortions (initial state interactions), final state interactions, modifications to the electromagnetic vertex function for bound particles (off-mass-shell effects) and many-body effects like Meson Exchange Currents (MEC) and Isobar Configurations (IC). In LEA the mentioned effects, except MEC and IC, are dealt with as explained below. Calculations have shown that MEC and IC have little impact (less than 15%) on the polarization transfer observables [58].

Electron Distortions.

Electron distortions and final state interactions were handled in this calculation by the Distorted Wave Impulse Approximation (DWIA). In DWIA, the electron wave function is distorted by a Coulomb potential. The electromagnetic transition amplitude for a single-nucleon knockout reaction in the DWIA can be written as

$$\mathrm{M} = \int \frac{\mathrm{d}^3\mathrm{q}'}{(2\pi)^3}\, \mathrm{J}^{\mathrm{e}}_{\mu}(\mathrm{q}')\, \frac{1}{\mathrm{Q}'^2}\, \mathrm{J}^{\mu}_{\mathrm{N}}(\mathrm{q}'). \tag{3.1}$$

Here $J^e_\mu(q')$ and $J^\mu_N(q')$ are the electron and nuclear currents, and q', Q' are the local three momentum and four momentum transfers supplied by the electron respectively. In the absence of Coulomb distortions, the electron current will be proportional to a unique value of momentum transfer (q') which in turn can be used for the calculation of the nuclear current. However in the presence of the Coulomb interaction, the local electron current and the asymptotic electron current differ. In order to account for this effect the LEA calculation utilized the Effective Momentum Approximation (EMA). Here, the effective momentum transfer, $q_{eff} = \overline{k_i} - \overline{k_f}$, is obtained by replacing the asymptotic momenta k by local momenta $\overline{k}$ accelerated by the mean electric potential.

Final State Interactions.

Final State Interactions (FSI) were modeled in LEA using the EDAD1 (Energy Dependent A Dependent) optical potential fitted to proton elastic scattering data by Cooper *et al.* [39] using Dirac phenomenology.

As was shown by J.J. Kelly [40], for quasi-free kinematics like ours, P'_l, P'_t are insensitive to the optical potentials used (FSI) or the current operators used (gauge dependence) and insensitive to variations of the off-shell extrapolation of the vertex function. This suggests that polarization transfer observables are insensitive to variations in the one-body current operator. Therefore, as several calculations suggest, if two-body currents affect P'_l and P'_t [41] [42], the polarization transfer technique is a sensitive method to investigate two-body current effects.

Gauges and off-mass-shell effects.

The extrapolation of the electromagnetic vertex function to off-shell conditions, *i.e.* to deal with a bound nucleon, were obtained by the de Forest prescription. Here free spinors were employed with momentum $\vec{p}$ and mass m, but the energy E used within the vertex function is replaced by the value $\overline{E}$ it would have had if the nucleon were on-shell in the initial state. The off-shell vertex functions derived by de Forest are called $\overline{\Gamma}_{cc1}$, $\overline{\Gamma}_{cc2}$ and $\overline{\Gamma}_{cc3}$ where cc stands for the current conservation. For the calculations used in this thesis $\overline{\Gamma}_{cc1}$ vertex function was used.

However, non of the DWIA calculations conserve current explicitly. Thus the current conservation was restored in an ad-hoc manner using the de Forest prescription [37] [38]. There is no evidence that the de Forest prescription is better than other off-mass-shell extrapolations, but it has the virtue of being commonly used. In this approach, the longitudinal component of the nuclear current was equated to its charge (this prescription is associated with the Coulomb gauge).

Due to the current non-conservation in the DWIA formalism, the calculations performed using different gauges produce different results. However, as shown in Figure 3.1 for the final state proton polarizations, the effect of these gauge ambiguities are negligible for our kinematics (pmiss $<$ 150 MeV/c). Unlike the case of cross section experiments, this makes the polarization measurements easy to compare to theory. The figure shows the polarization transfer observables for three gauges, Landau, Coulomb and Weyl. For the LEA calculations used in this thesis we used the Coulomb gauge.

Form factors used.

In LEA, assuming free values for the form factors for the proton inside ^{16}O nucleus, we calculated P_t' and P_t' after correcting for all the above mentioned effects and compared to the data to study possible medium modifications of the form factors for the proton. The H$(\vec{e}, e'\vec{p})$ data available in the acceptance was used to calculate the form factor ratio $\mu G_E/G_M$ for the free proton at the Q^2 value of this experiment.

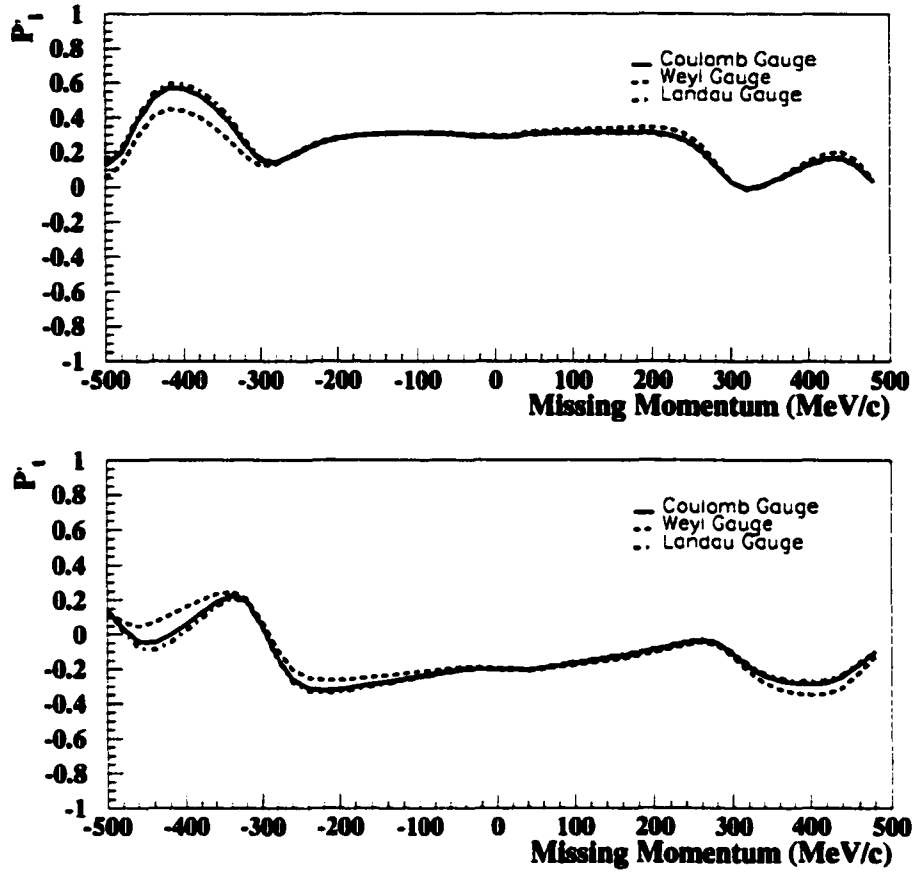

Figure 3.1: Gauge ambiguities in polarization transfer observables.

As shown later, this measurement indicated that the Mergell, U.G. Meissner and D. Drechsler [121], [122] (MMD) form factor model explain these data best. Thus this model was used in the LEA calculations to obtain the form factors.

The Figure 3.2 shows the two polarization observables P_l' and P_t' calculated using LEA.

3.2 Calculations by J.W. Van Orden.

Two DWIA calculations by J. W. Van Orden, a relativistic calculation and a non-relativistic calculation, were also compared to the present data. Both these calculations are discussed in detail in Ref. [22] and [28].

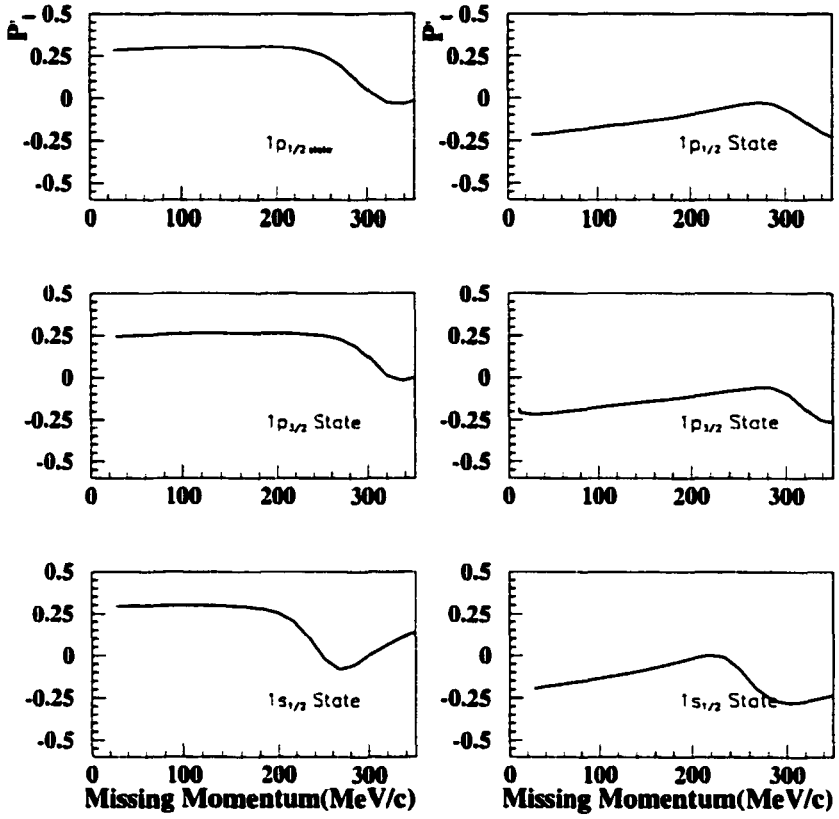

Figure 3.2: Non-relativistic DWIA calculations of P_l' and P_t' by J.J. Kelly's code LEA, assuming free values for the bound nucleon form factors.

3.2.1 Dirac DWIA calculation.

The Dirac DWIA calculation uses the single particle Dirac current operator with the Höhler 8.2 parameterization [43] for the nucleon form factors:

$$J^{\mu}(q) = F_1(Q^2)\gamma^{\mu} + \frac{F_2(Q^2)}{2M_N} i\sigma^{\mu\nu}q_{\nu}. \tag{3.2}$$

Here F_1 and F_2 are the Dirac and Pauli form factors.

For the bound state wave functions Van Orden uses the relativistic independent-particle Hartree type model which is derived from full quantum field theory [44] (Walecka model). The FSI are handled by a Dirac optical potential model using a Love-Franey parameterization [45].

3.2.2 Non relativistic DWIA calculation.

The non-relativistic DWIA calculation is described in detail in Ref. [46].

Figure 3.3 shows the relativistic and non-relativistic Van Orden calculations of the two polarization transfer observables P_l' and P_t' at Q^2 =0.8(GeV/c)^2 and a proton kinetic energy of 435 MeV. As the figure indicates, the relativistic effects are negligible at missing momentum less than 275 MeV/c, again showing the model independence of the polarization transfer observables.

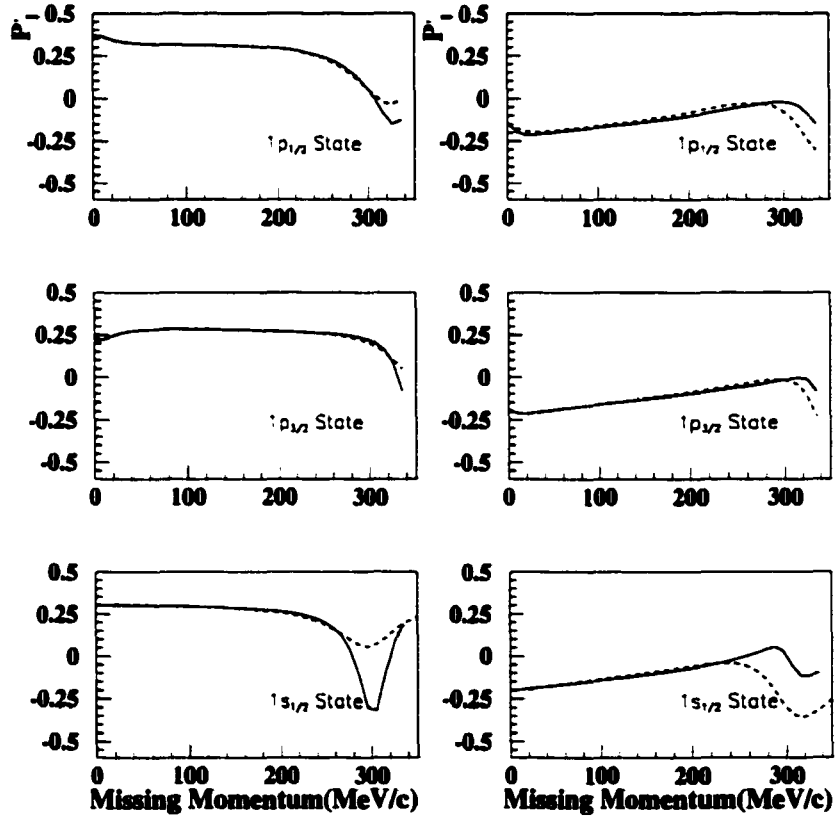

Figure 3.3: P_l', P_t' calculations by Van Orden. The dashed curve represents the Dirac DWIA calculation and the solid curve shows the non-relativistic DWIA calculation.

3.3 Two body currents.

Although there are strong arguments for the fact that the IA is a reasonable theory in the case of quasielastic kinematics, (e, e'p) measurements performed in quasielastic conditions suggest that the nuclear medium can be described as consisting of about 70% mean field behavior and about 30% correlations [47].

For a many body system, polarization response functions can be dependent upon the effects of two body and higher order electromagnetic currents because their spin structure can be different from that of the one body current. The Feynman diagrams corresponding to Meson Exchange Current (MEC) and Isobar Current (IC) contributions to the two body current operator in the nucleon knockout reaction are shown in Figure 3.4.

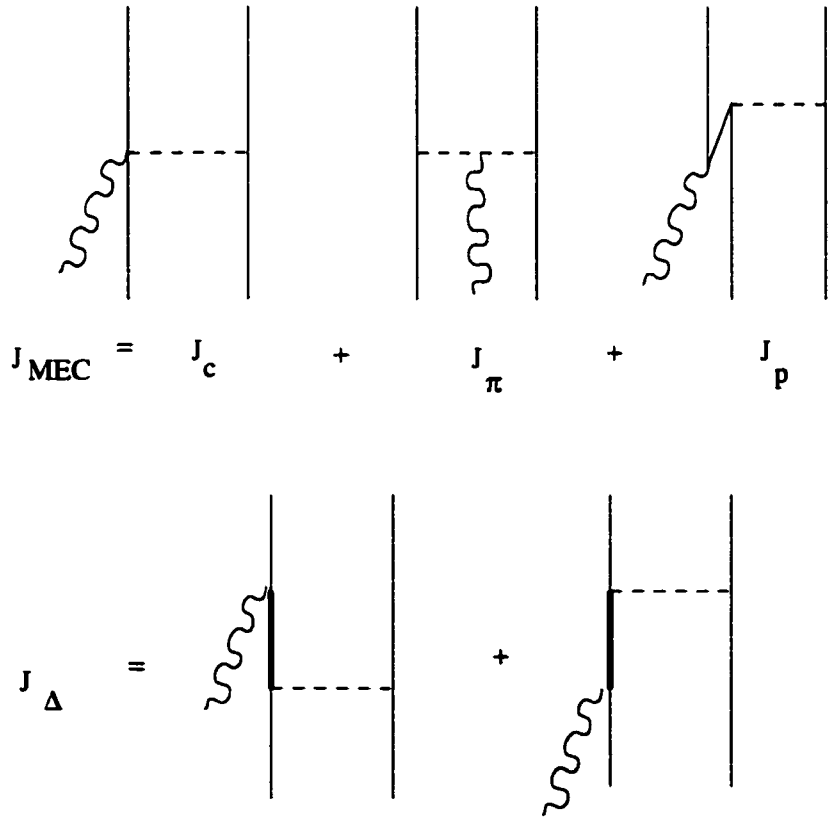

Figure 3.4: Feynman diagrams for MEC and IC contributions to the two body current operator. The top row represents the MEC's and the bottom row represents the IC's.

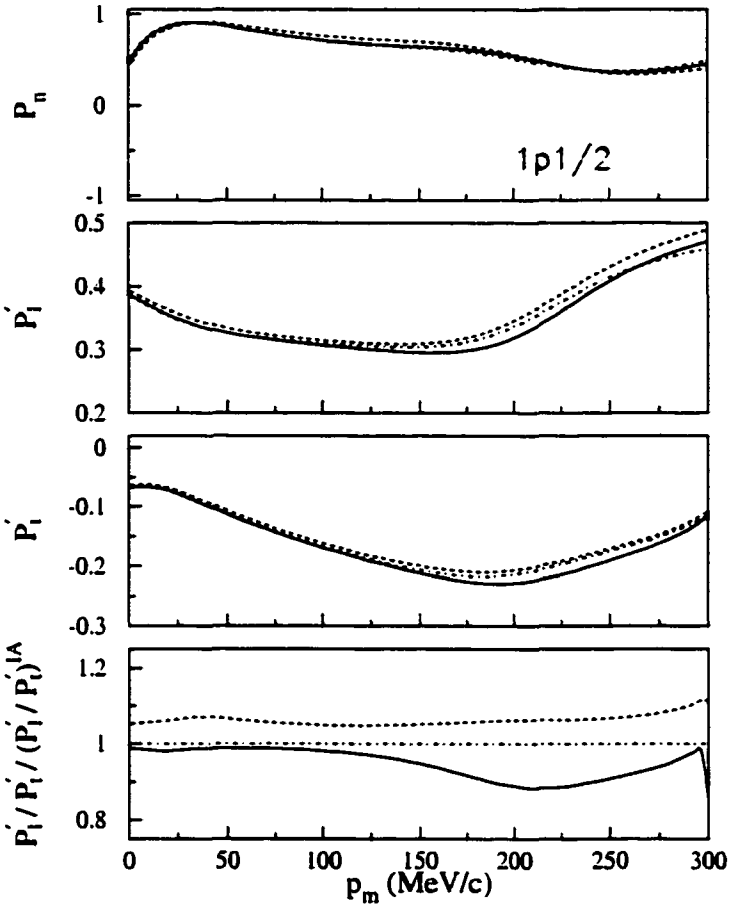

Figure 3.5: Effects of two body currents on the polarization observables calculated by Ryckebusch *et al.* [58]. The calculations are for the ^{16}O $(\vec{e}, e'\vec{p})$ reaction. The recoil polarization observables are given as functions of missing momentum for the $1p_{1/2}$ state, with beam energy at 2.445 GeV, ω=445 MeV and q=1 GeV/c. The dot-dashed curves show the results for the impulse approximation; in the dashed curves MEC effects are also included, and the solid curves represent the full calculation including also IC.

Recently MEC and IC calculations have been performed specifically for the kinematics of the present experiment for ^{16}O by Ryckebusch *et al.*, from the Gent group [58]. The results for the recoil polarization observables for the three states $1p_{1/2}$, $1p_{3/2}$ and $1s_{1/2}$ are shown in Figure 3.5, Figure 3.6 and Figure 3.7 respectively. This calculation includes MEC and Δ IC contributions and the effects of central Short Range Correlations (SRC). This is a Hartree-Fock, random phase approximation (HF-RPA) calculation [54], [55], [56], [57].

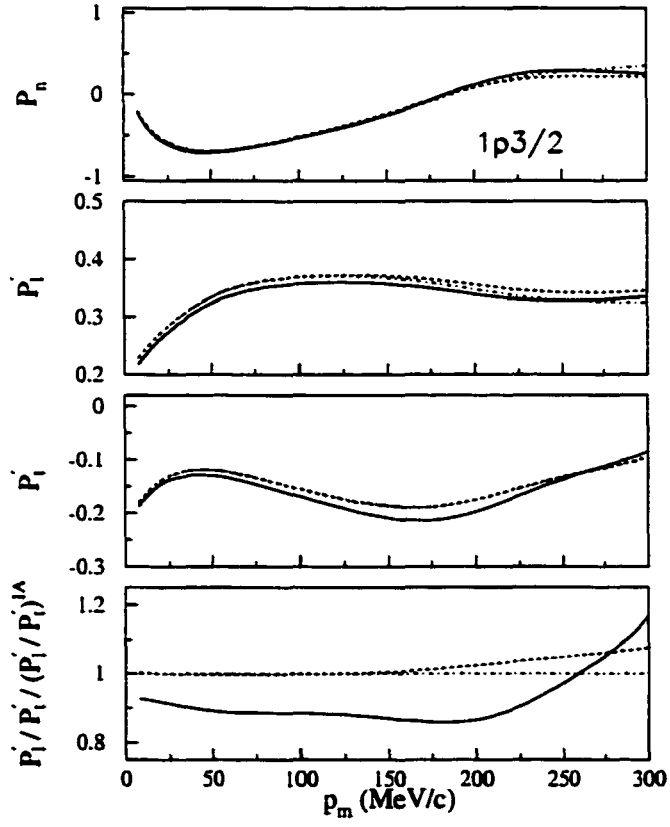

Figure 3.6: Same as in Figure 3.5 but for the $1p_{3/2}$ state [58].

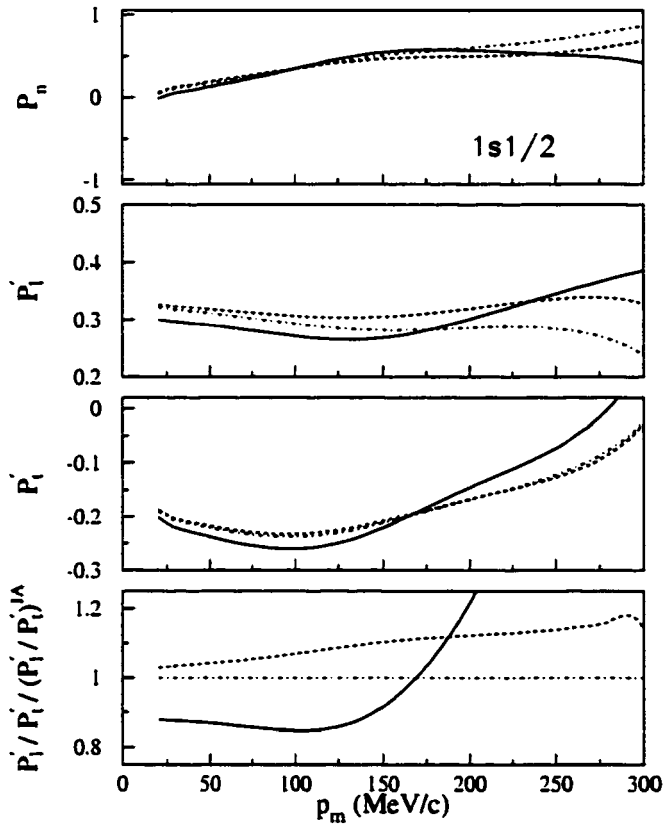

Figure 3.7: Same as in Figure 3.5 but for the $1s_{1/2}$ state [58].

As Figure 3.5 indicates, the effects of two body currents on P_l' and P_t' for the $1p_{1/2}$ state are very small within the momentum range covered by this experiment; the effects are only at the couple of percent level. Gent model calculations show quite different effects on $1p_{1/2}$ and $1p_{3/2}$ states, suggesting strong nuclear structure effects. The effect is largest for the $1p_{3/2}$ state. Still, the deviations from the IA is only about 15% within the relevant range (85-140MeV/c).

3.4 Medium modification of the nucleon form factors.

In order to consider possible changes in the properties of the nucleon, such as its size, due to the nuclear environment, in this experiment we investigate the change in the form factor ratio for the proton inside the ^{16}O nucleus compared to the same ratio for a free proton via the recoil polarimetry technique. This is the first experiment to look for medium modification effects via this technique.

In an average nucleus, the inter-nucleon distance is only about 20% larger than the sum of the nucleon radii. There is strong evidence that the nucleon bound in an atomic nucleus experiences very strong effective scalar and vector fields [59], [60], [61], [62], [63]. Furthermore, since the nucleon has internal degrees of freedom, the individual quarks of a nucleon can couple to the mesons outside the nucleon changing the nucleon size and the charge and magnetic radii. It is a fundamental issue in nuclear physics to understand whether these strong fields alter the internal structure of the nucleon and if so, by how much. In the past, there had been experimental evidence supporting and opposing this idea of a change in the properties of the nucleon inside the nuclear medium.

All of the past experiments used the Rosenbluth separation technique to obtain the G_E/G_M ratio for a bound nucleon. From the ratio of separated response functions, a ratio R_G is formed which is interpreted as the ratio of magnetic to charge form factors for a bound proton. These results, obtained from (e,e'p) reactions, are shown in Figure 3.8 for ^{6}Li [12], ^{12}C [11], [12], [13], ^{40}Ca [13]. This figure suggests that the value for $\mu G_E/G_M$ for the in medium nucleon is approximately 0.81.

Unlike in polarimeter measurements, in cross section experiments it is theoretically shown that the results depend heavily on the reaction mechanism used, *i.e.*, depend heavily on the type of optical potentials used to model the FSI's, type of

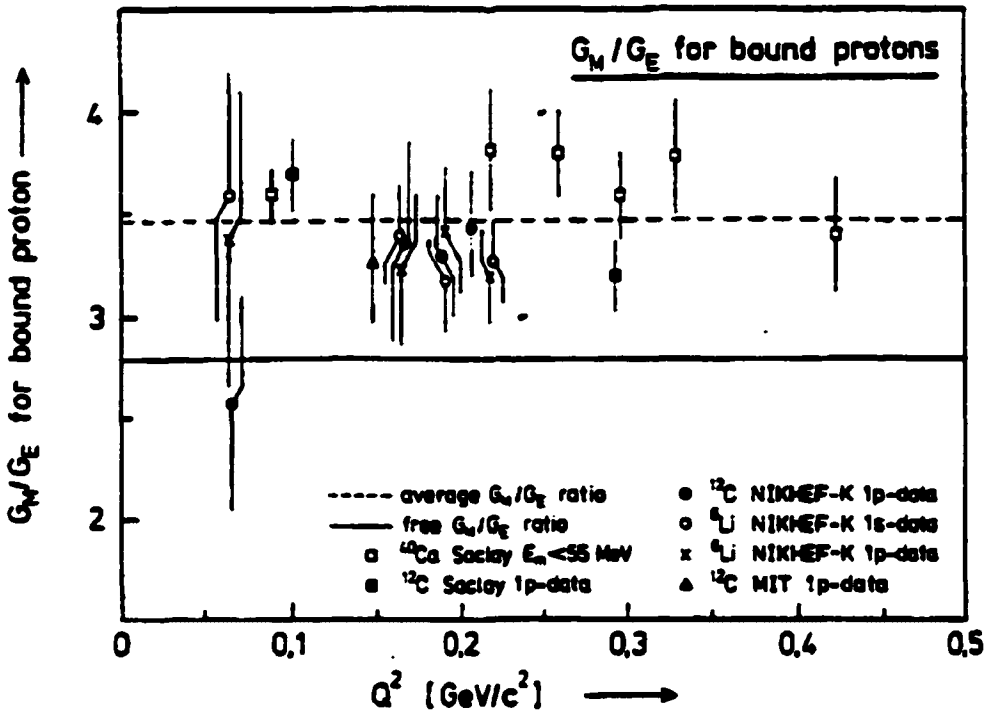

Figure 3.8: R_G or ratio of form factors for a bound proton,as a function of Q^2 from exclusive quasi-elastic experiments using the Rosenbluth separation technique on ^{6}Li, ^{12}C and ^{40}Ca. Results from MIT [11], NIKHEF [12] and Saclay [13] are displayed. Taken from [14].

gauge used to enforce the current conservation, or whether or not the MEC corrections are taken in to account in the analysis. Therefore, the effects of a possible medium modification of the virtual photon-proton coupling are so intertwined with reaction mechanism effects as Final State Interactions (FSI) and Meson Exchange Currents (MEC), that these studies do not permit an unambiguous interpretation of the data. Further more, later in this thesis we will show that the present technique has lower systematic uncertainties than the methods used in the past.

3.4.1 Evidence supporting medium modifications.

EMC effect.

The response functions of the nucleon (deep inelastic scattering) depends on the nucleus in which the nucleon is bound. It is reasonable to expect that the quarks

inside a nucleus may play an important role in some contexts, and their wave functions could be strongly modified by the surrounding nuclear environment. The EMC effect has indicated that the momentum distributions of quarks in bound nucleons differ from those of the free nucleons [64].

Lack of strength in the longitudinal response function.

There has been a number of experiments performed with the aim of separating the longitudinal and transverse contributions to the quasielastic cross section from the inclusive electron-nucleus (e e′) scattering data. Good agreement with Impulse Approximation (IA) predictions was found for nuclei with A < 4 [65], [66], [67], [68]. However, for heavier nuclei ^{12}C [69], ^{40}Ca [70], [71], [72], ^{48}Ca [71], [72], ^{56}Fe [71], [73] this was not the case.

A common feature observed in all these experiments was that $R_L(q,\omega)$ was significantly lower (up to 40% at q $\approx$ 550 MeV/c) than the Fermi-gas model predictions. This "quenching" of $R_L(q,\omega)$ was particularly disturbing in regards to the model independent Coulomb sum rule [74],

$$S_L(q) = \frac{1}{Z}\int d\omega \frac{R_L(q,\omega)}{\tilde{G}_E^2(Q^2)}. \qquad (3.3)$$

Here Z is the atomic number of the nucleus, Q is the four momentum transfer and $\tilde{G_E}$ is an effective nucleon charge form factor which is an appropriate sum of neutron and proton charge form factors. In the absence of any "missing strength", for a system of non-relativistic nucleons, the sum, $S_L(q)$ should approach to 1 as q$\rightarrow\infty$.

Swollen nucleon hypothesis.

The missing strength of the R_L motivated a large theoretical effort. The most common interpretation was that the charge radius (but not the magnetic radius) of the nucleon increases in the nuclear medium, as a consequence of the partial deconfinement of the quarks inside the nucleon [75], [76], [77]. An increase in size would modify the nucleon charge form factor $\tilde{G_E}(Q^2)$, thus leading to a reduced $R_L(q,\omega)$.

3.4.2 Evidence opposing medium modifications.

Reanalysis of world data on inclusive quasielastic scattering.

Although there is a wide range of inclusive quasielastic scattering data, the consistency between them is rather poor. A more recent measurement on ^{40}Ca [78], together with the data of Deady *et al.*, [72] gives a R_L which differs markedly from previous determinations. Measurements on ^{208}Pb [79] show a reduction of 50% in $S_L(q)$ at a q of 550 MeV/c suggesting an A-dependent "quenching" whereas no reduction was found for ^{238}U [80].

Furthermore, a reanalysis of the Coulomb sum for ^{12}C and ^{56}Fe by J. Jourdan [81] using all the world data which cover most of the virtual photon polarization range finds complete agreement with conventional model predictions. No A-dependent "quenching" is observed. A yet more recent analysis by J. Morgerstern, however disputes this finding [82].

In this reanalysis by Jourdan, Coulomb distortion effects which have been neglected in the analysis of [69] and [71] are included. The use of the world data covering the full range of virtual photon polarization (a standard procedure in the determination of precise elastic form factors [84], [83]) enhances the sensitivity to $R_L(q,\omega)$ by a factor of two. Since $R_L(q,\omega)$ is mainly determined by the inclusion of the high-energy/low-angle data, the larger range in energy makes the results less dependent on the use of the maximum range of scattered energies as imposed by measurement using a single facility. Therefore this analysis enhances the sensitivity to $R_L(q,\omega)$ and allows a more reliable determination of the Coulomb sum rule. This article puts experimental limits on the change of the electric form factor to about 4%. Figure 3.9 shows the data set for highest q (=570 MeV/c) (where Pauli correlations are the smallest, and an interpretation in terms of a model independent sum rule makes sense), from the reanalysis of the Coulomb sum rule $R_L(q,\omega)$ for ^{56}Fe compared to two conventional theoretical calculations.

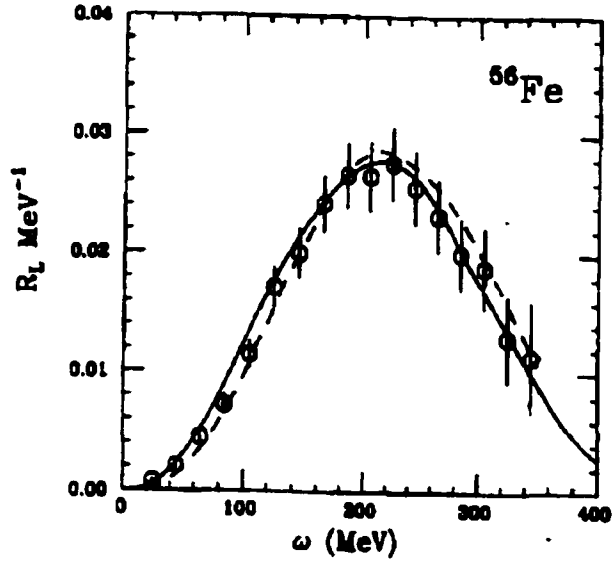

Figure 3.9: Results for $R_L(q,\omega)$ from ^{56}Fe at q = 570 MeV/c using the world data, compared to the calculations of Fabrocini *et al.* (solid) [85] and Jin *et al.* (dashed) [86]

Constraints from Y-scaling data from inclusive scattering.

In general, the inclusive scattering cross section for a nucleus is a function of two variables: $\vec{q}$ and ω. In the impulse approximation $\vec{q}$ and ω are related by

$$\omega = \frac{\vec{q}^2}{2M_N} + \frac{\vec{q}\cdot\vec{p_i}}{M_N}. \tag{3.4}$$

Here $\vec{p_i}$ is the initial nucleon momentum and M_N is the nucleon mass.

The scaling variable y is defined as the component of the initial nucleon momentum along $\vec{q}$. In the limit q very much greater than the component of the initial momentum perpendicular to $\vec{q}$, ω very much greater than nuclear binding energy, and in the non-relativistic limit, y can be written as

$$y_{nr} = \frac{\vec{p_i}\cdot\vec{q}}{M_N} = \frac{\omega}{|\vec{q}|} - \frac{|\vec{q}|}{2M_N}. \tag{3.5}$$

Here y_{nr} is the y scaling variable in the non-relativistic limit.

In the impulse approximation, for quasielastic scattering the inclusive cross section factors into an elementary in-medium electron-nucleon cross section for a

moving nucleon summed over all nucleons, $\sum \sigma_{eN}(q)$, times a structure function $f(y)$, at constant q^2:

$$\frac{d\sigma}{d\Omega}(q,\omega)d\omega = \sum(\sigma_{eN}(q))\, f(y)dy \tag{3.6}$$

$$\frac{\frac{d\sigma}{d\Omega}(q,\omega)}{\sum \sigma_{eN}(q)} \frac{d\omega}{dy} = f(y). \tag{3.7}$$

Thus, the inclusive cross section depends on a single variable y rather than depending on $\vec{q}$ and ω separately. The cross section is then said to scale in the variable y, hence the term y-scaling.

This can be used to look for medium modification effects on the form factors, since the function $f(y)$ will not scale, if one uses an in-medium cross section that does not have the correct q dependence. The work done by many people [87], [88], [89], [90] shows a striking scaling behavior: the inclusive cross sections from different q, ω define a unique curve for the negative values of y (energy loss smaller than for the maximum of the quasielastic peak). The scaling of inclusive cross-sections for longitudinal and transverse components in y is shown in Figure 3.10. One surprising result is that although the longitudinal and transverse response functions of ^{12}C appear to scale separetely, they do not have the same universal scale. Moreover, the longitudinal response appears to scale in both positive and negative y, whereas the transverse response scales only for negative y. At positive y other reaction mechanisms such as two-body currents and delta production dominate.

Sick *et al.* [91] used this y-scaling behavior to quantify the change in the in-medium form factors. They fit the values of $f(y)$ for y<-50 MeV/c using different e-N cross-sections corresponding to different bound-nucleon sizes. Good χ^2 implies good scaling. The results are shown in Figure 3.11. The left hand side gives $f(y)$ calculated using the free e-N cross-section. The right hand side gives a χ^2 of the fit obtained using different bound nucleon form factors. As the figure indicates, the minimum (best scaling) χ^2 corresponds to 2% change in radius for the bound nucleon. Therefore they predict that the bound nucleon form factors have the same q-dependence as those of

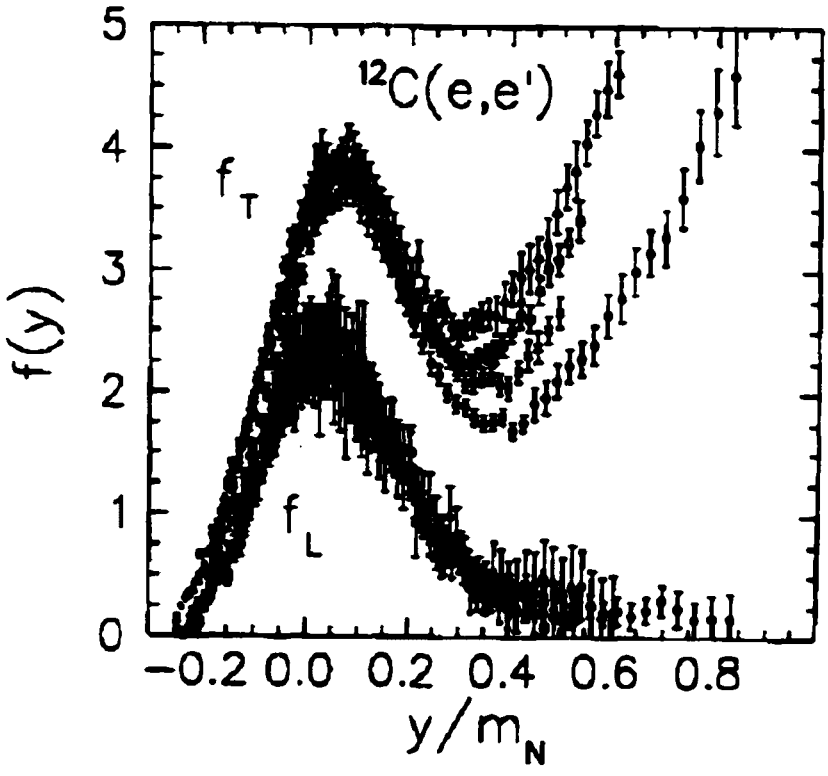

Figure 3.10: The longitudinal and the transverse components of the inclusive cross-section scale in y for different values of q using the relativistic Fermi gas y-scaling variable. Scaling analysis of separated data for ^{12}C(e,e'). Circles, crosses, squares, triangles and diamonds correspond to q = 400, 450, 50, 550 and 600 MeV/c respectively. From Finn *et al.* [88].

a free nucleon. It should be noted, however, that these data are dominated by the behavior of G_M with little strength from G_E. So this result has few implications for G_E/G_M.

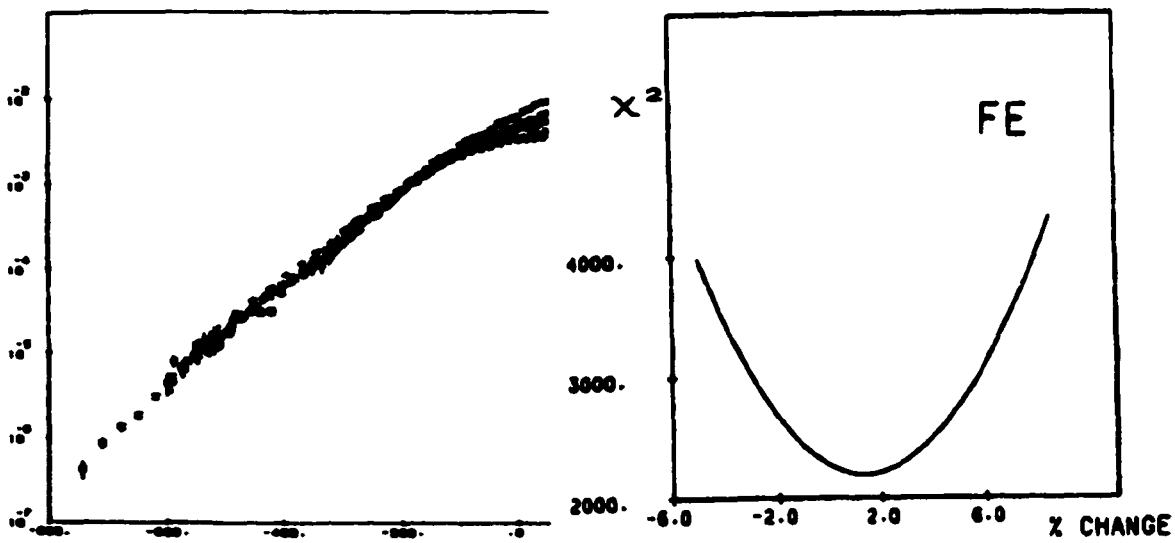

Figure 3.11: Left: ^{56}Fe(e,e') data (q=3-12 fm^{-1}) plotted in terms of $f(y)$ as a function of the scaling variable y (MeV/c). Right: χ^2 of fit to $f(y)$ as a function of the assumed change of radius of the bound nucleon.

Superscaling data from inclusive scattering.

T.W. Donnelly *et al.*, [92], [93] have studied the Super-scaling function ψ of different nuclei with mass number A$\geq$4. This is an alternative to the y-scaling function and is derived from the IA which uses the Relativistic Fermi Gas model (RFG) [94], [95]. We refer the reader to the above references for more detail.

A dimensionless scaling variable ψ is defined:

$$\psi = \frac{1}{\sqrt{\xi_F}} \frac{\lambda - \tau}{\sqrt{(1+\lambda)\tau + k\sqrt{\tau(1+\tau)}}}. \tag{3.8}$$

Here $\xi_F = \sqrt{1+\eta_F^2} - 1$ and $\eta_F = k_F/M_N$ are the dimensionless Fermi kinetic energy and momentum respectively. The other dimensionless variables are defined as, $k = q/2M_N$, $\lambda = \omega/2M_N$ and $\tau = k^2 - \lambda^2 > 0$. Then ψ is changed to ψ' by accounting for the fact that nucleons are knocked out of all shells in the nucleus. Then within the RFG model a function F(k, ψ) can be defined

$$F(k,\psi') \simeq \frac{k_F d^2\sigma/d\Omega_e d\omega}{\sigma_M(V_L(k/2\tau)\tilde{G}_E^2 + V_T(\tau/k)\tilde{G}_M^2)} \tag{3.9}$$

$$\tilde{G}_E^2(\tau) = ZG_{Ep}^2 + NG_{En}^2 \tag{3.10}$$

$$\tilde{G}_M^2(\tau) = ZG_{Mp}^2 + NG_{Mn}^2. \tag{3.11}$$

Here n and p subscripts in G_E and G_M correspond to neutron and proton respectively. Using the above formalism, Donnelly *et al.*, have analyzed data on electron-nucleus quasielastic scattering for nuclei with mass numbers A=4-208. The set of data covers a large range in q, ω. This analysis has revealed that the data on the low-ω side of the quasielastic peak ($\psi' < 0$) show scaling behavior for nuclei with different atomic mass number A, hence the term, Superscaling (see Figure 3.12). This suggests that different nuclei have a universal momentum distribution which again suggests the absence of medium modification effects for the form factors. However, scaling appear to work even for large negative ψ' values, beyond the range where one-body mechanisms should dominate. This effect is not currently understood.

As one can see from the above discussion, although there have been many experiments performed in the past with the intention of looking for medium modification effects, the available evidence does not unambiguously indicate whether or not there are medium modification effects. This is an interesting and important open question in the field of nuclear physics. A clear solution for this question is essential for a better understanding of the structure of the nucleus. The recoil polarimetry technique of studying medium modifications should prove to be a very powerful tool to resolve this long-standing controversy about the nuclear medium effects on the nucleon form factors.

3.4.3 Calculations using the Quark Meson Coupling model.

A recent theoretical calculation performed by the Adelaide group [96] has indicated that this kind of experiment is ideal to look for medium modification effects,

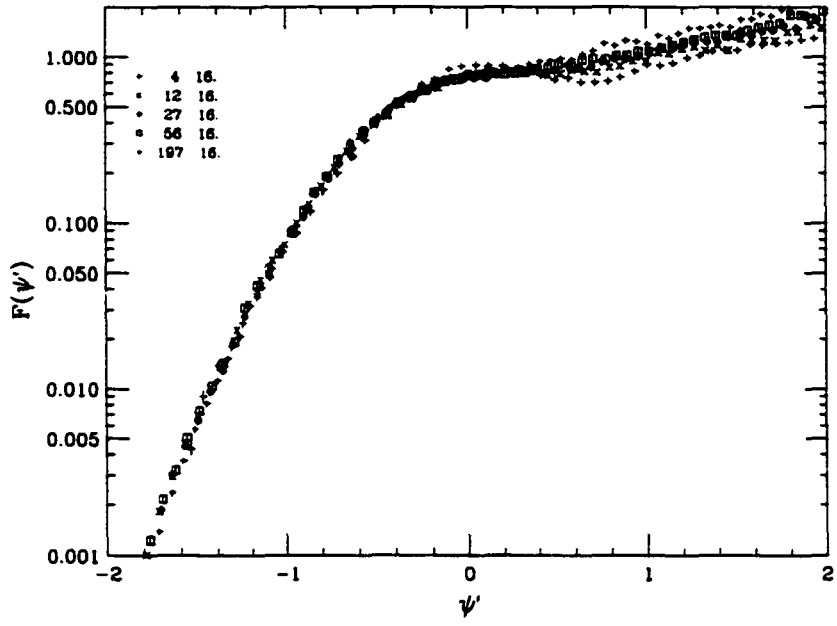

Figure 3.12: The scaling function, F(ψ') for nuclei A=4-197 and fixed kinematics, on logarithmic scale. The values of A corresponding to the different symbols are shown in the insert.

since they predict significant changes in the ratio of G_E/G_M in the medium. They use a Quark Meson Coupling (QMC) model [61], [62], [63], [98] for these calculations and predict the fractional changes in the internal structure of the bound nucleon from the free nucleon. Since they do not use any free nucleon form factor parameterization in their calculation, one can use their predicted ratios with measured values of the free form factors to obtain the predicted in-medium form factors.

In the QMC model, the nucleon is assumed to have substructure given by the MIT bag model [99], [100], [101]. As in Quantum Hadrodynamics (QHD) [59], [32], the QMC model describes the properties of the nuclear system using effective scalar (σ) and vector (ω) fields. These σ, ω fields are, however, coupled directly to the quarks within the nucleons, rather than to the nucleons themselves. This results in modification of the internal structure of the bound nucleons with respect to free ones. Furthermore, the meson cloud surrounding the nucleon is handled by the Cloudy Bag Model (CBM) [102], [103]. This model limits the meson cloud corrections to the most dominant component, the pion cloud (see Figure 3.13).

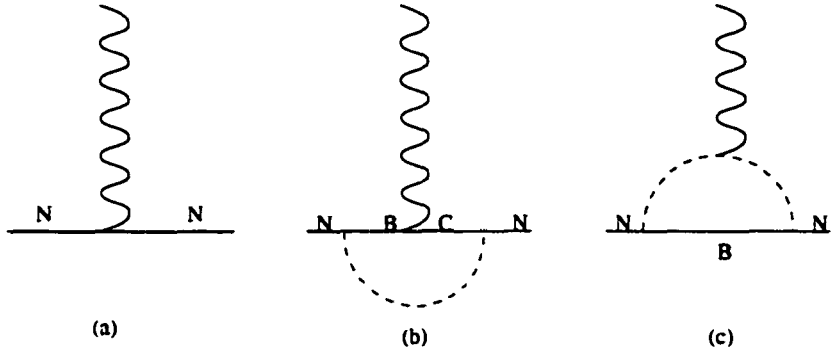

Figure 3.13: The Cloudy Bag Model calculations up to one pion loop by the Adelaide group [104] are shown here. The intermediate baryons B and C are restricted to the N and Δ.

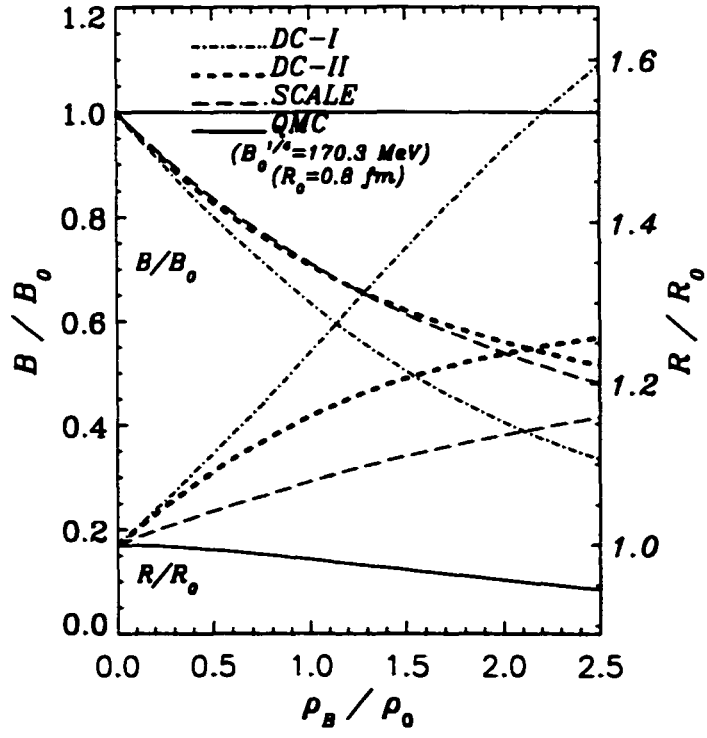

Figure 3.14: The predicted density dependence of the bag constant, B, and the bag radius, R. Calculations by the Adelaide group using the Cloudy Bag Model (CBM) [104].

This model includes relativistic corrections such as momentum projection and Lorentz contraction of the internal structure. In this calculation the off-shell effects are ignored and a density-dependent bag constant B is assumed. The in-medium bag radius is also dependent on density. In the Adelaide group calculation, the bag constant decreases in the nuclear medium and is supposed to depend on either the mean scalar field or the effective mass of the nucleon. The Figure 3.14 shows the predicted dependence of the bag constant, B, and bag radius, R with nuclear density [104]. For ^{16}O, average density is about 0.6 ρ_0 where ρ_0 is the saturation density of symmetric nuclear matter (ρ_0=0.15 fm^{-3}).

While this calculation reproduces the saturation density, density of nuclear matter and compressibility of nuclear matter, it also produces realistic form factors in free space at least at lower Q^2, as well (Figure 3.15).

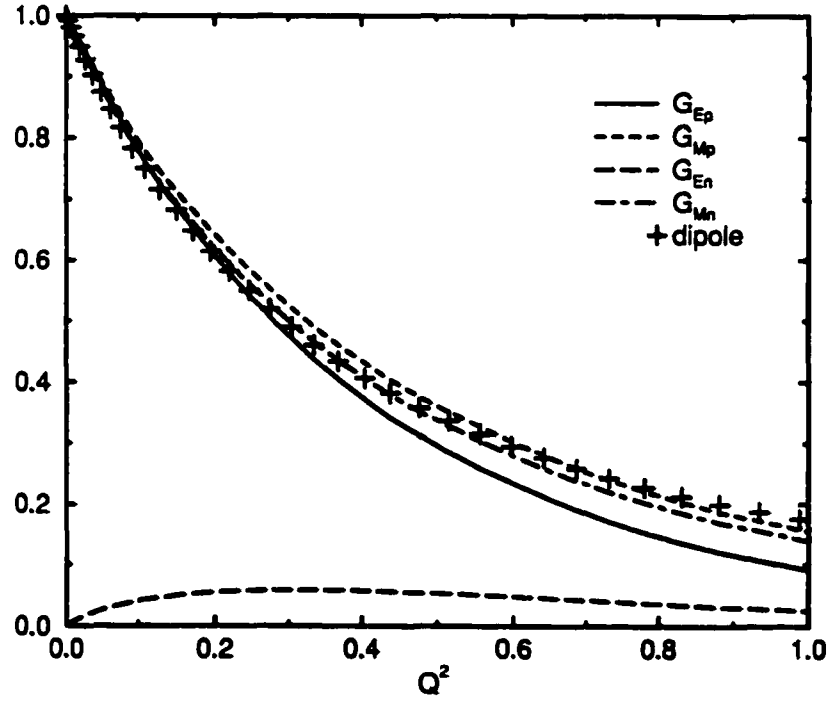

Figure 3.15: The predicted nucleon electromagnetic form factors in free space. The bag radius is chosen to be R=1 fm here. Calculations by the Adelaide group using the Cloudy Bag Model (CBM) [96].

The results of this calculation show that charge form factors are much more sensitive to the nuclear medium density than the magnetic ones. Further, increasing density suppresses the electromagnetic form factors for small Q^2. For a fixed Q^2, they notice that the form factors decrease almost linearly with nuclear density, ρ. These results are shown in the Figure 3.16.

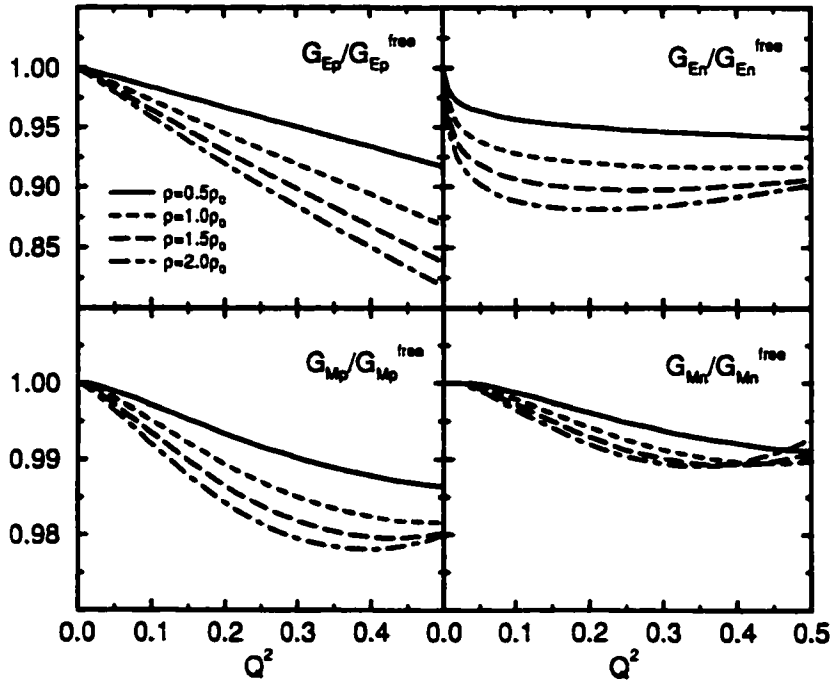

Figure 3.16: The calculated nucleon electromagnetic form factors in the nuclear medium (relative to those in free space) [96]. The free space bag radius is 1 fm and the density is quoted in units of the saturation density of symmetric nuclear matter ($\rho_0 = 0.15$ fm^{-3}).

The Lu *et al.*, calculations [97] for ^{16}O at Q^2= 0.8 (GeV/c)^2, as shown in Figure 3.17, results in a super ratio $((G_E/G_M)_{medium}/(G_E/G_M)_{free})$ of 0.89 for the p states and 0.85 for the $1s_{1/2}$ state. These numbers were used in our theoretical analysis code LEA to obtain P_l and P_t curves corresponding to these medium effects to compare with the experimental results.

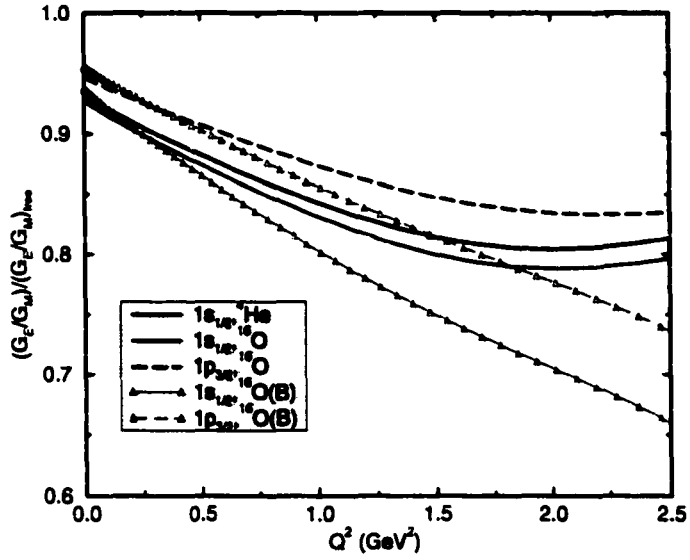

Figure 3.17: The calculated super ratio $(G_E/G_M)_{medium}/(G_E/G_M)_{free}$ for ^{16}O and ^{4}He calculated by Lu *et al.*, using the Cloudy Bag Model. (B) corresponds to a change in the bag constant B.

Chapter 4

Experimental Setup.

In this experiment we measured the two polarization transfer observables P_l' and P_t' and the induced polarization P_n of a proton inside ^{16}O nucleus. This was the first measurement ever performed of the polarization transfer observables in the (e,e'p) reaction on a complex nucleus. This was done for two pmiss (momentum of the proton inside the nucleus in the PWIA) points 85 MeV/c and 140 MeV/c. This experiment was performed during the Summer of 1997, at Hall A of Thomas Jefferson National Accelerator Facility (Jefferson Lab) located in Newport News, Virginia. This was the first experiment to use polarized beam at Jefferson Lab.

We scattered a longitudinally polarized electron beam from an ^{16}O target and detected the scattered electron and the knocked-out proton in coincidence. We used the Hall A High Resolution Spectrometer (HRS) pair for the detection of the particles. To measure the polarization of the proton at the focal plane, we used the Focal Plane Polarimeter (FPP) on the HRS hadron arm. Polarized electrons were obtained from the polarized source at the accelerator and a Mott polarimeter was used to measure the polarization of the incident beam at the injector. Little or no de-polarization of the beam is expected in the accelerator. A "spin-dance" was performed rotating the launch angle of the electrons to maximize the longitudinal component of the beam on target. Although the Molar polarimeter in Hall A was not in full operation during the

running-time of this experiment, it was used for a relative measurement to compare to the Mott measurements in the "spin-dance".

In this chapter we describe the experimental setup and data acquisition method. We briefly describe the continuous electron beam linear accelerator at the Jefferson Lab, and the Mott polarimeter. We also describe the waterfall target used for this experiment, and the two HRS spectrometers and provide a detailed description of the focal plane polarimeter. Finally, we discuss the data acquisition system.

4.1 The Accelerator.

Jefferson Laboratory, consists of two linear accelerators (linacs) that can deliver a high-quality continuous electron beam (*i.e.*, 100% duty factor) either with high intensity (100 μA) per hall or low intensity to all three experimental halls simultaneously. Both polarized and unpolarized electron beams up to 5.5 GeV are available. Figure 4.1 shows a sketch of the Continuous Electron Beam Accelerator Facility (CEBAF) at Jefferson Lab.

The injector delivers 45 MeV electrons to the race-track type accelerator which consists of two nominal 0.4 GeV linacs. Beam energies in multiples of 0.8 GeV can be obtained by recirculating the electrons through the linacs. At the beam switch-yard the beam is extracted and delivered to the three experimental halls simultaneously. Since these linacs use super-conducting cavities, the heat produced during electron circulation is minimal. This allows the machine to deliver a continuous electron beam rather than a pulsed beam.

This experiment was performed at an incident beam energy of 2.445 GeV with about 30% beam polarization. The average beam intensity was about 40 μA. The beam available time between recesiations (adding cesium) for the GaAs crystal (polarized source) was approximately 6 hours. Since the present experiment, the accelerator has demonstrated the capability of producing much higher beam polarizations,

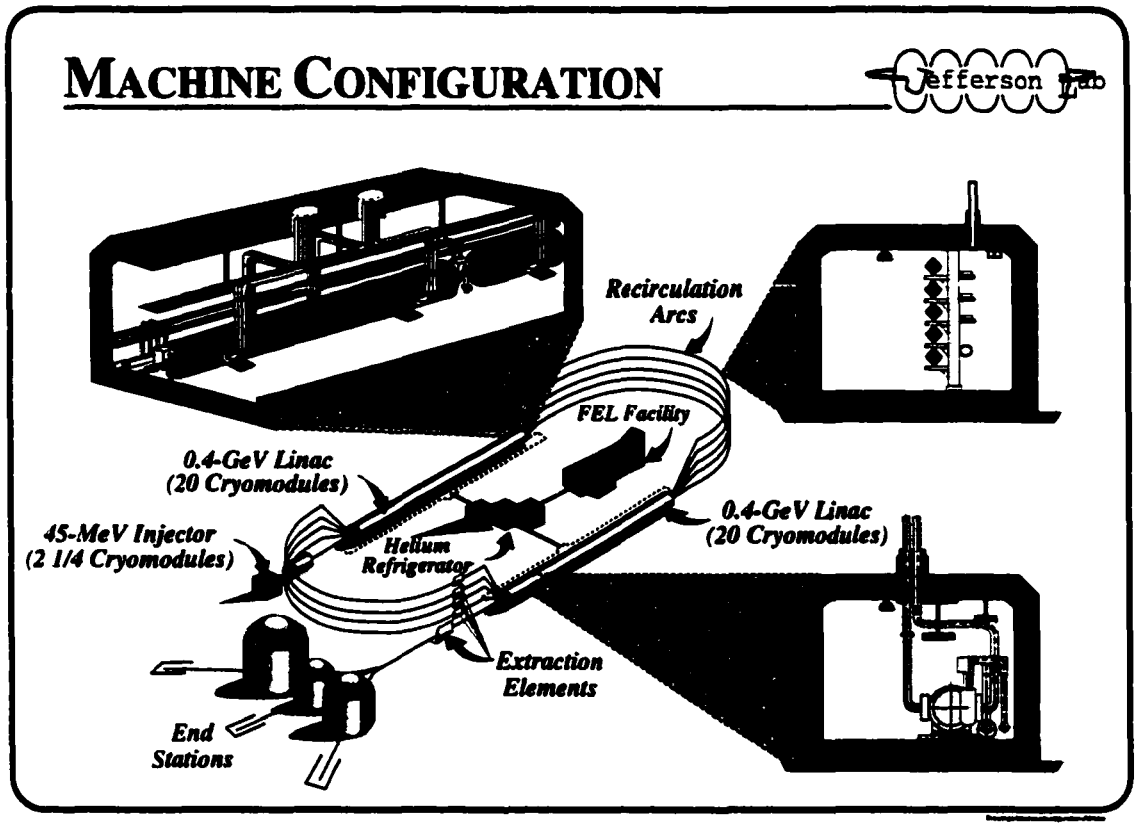

Figure 4.1: Continuous Electron Beam Accelerator Facility at Jefferson Lab.

intensities, and lifetimes.

4.1.1 Mott polarimeter.

In order to obtain the individual polarization-transfer obseravbles, we need to know the incident electron beam polarization. During the run-time of this experiment the only available technique to measure the beam polarization was to use the Mott polarimeter at the injector (the Hall A Mollar polarimeter was installed but not fully commissioned).

Formalism behind Mott scattering.

Mott scattering occurs when a high energy electron (spin 1/2 particle) scatters off a bare nucleus of charge Ze due to the $\vec{L} \cdot \vec{S}$ coupling. A magnetic field $\vec{B}$ is felt

by the moving electron in the electric field $\vec{E}$ of the nucleus

$$\vec{B} = -\frac{1}{c}\vec{v} \times \vec{E}, \tag{4.1}$$

where $\vec{v}$ is the electron velocity, and the electric field $\vec{E}$=(Ze/r^3)$\vec{r}$. Here $\vec{r}$ is the separation between the electron and the nucleus. If $\vec{r} \times \vec{E}$ is the orbital angular momentum, $\vec{L}$ of the electron, $\vec{B}$ is equal to

$$\vec{B} = \frac{Ze}{mcr^3}\vec{L}, \tag{4.2}$$

Here m is the electron mass. Since the electron spin, $\vec{S}$ is related to the magnetic moment μ by,

$$\vec{\mu} = \frac{e\vec{S}}{mc}, \tag{4.3}$$

the spin-orbit coupling potential,V_{so}, can be written as,

$$V_{so} = \frac{Ze^2}{2m^2c^2r^3}\vec{L} \cdot \vec{S}. \tag{4.4}$$

This spin-orbit potential introduces a spin-dependent asymmetry in the scattering cross section. By placing detectors perpendicular to the electron momentum direction, can measure the beam polarization.

Mott polarimeter used at Jefferson Lab.

A sketch of the Jefferson Lab 5 MeV Mott polarimeter is shown in Figure 4.2. The target used is a gold foil of 0.1 μm thickness. There are four plastic scintillator detectors placed at 173^0 to the incident beam. This configuration allows simultaneous measurement of the two beam polarizations perpendicular to the electron momentum. the angle 173^0 is chosen since this corresponds to the maximum analyzing power for the scattering process (see Figure 4.3).

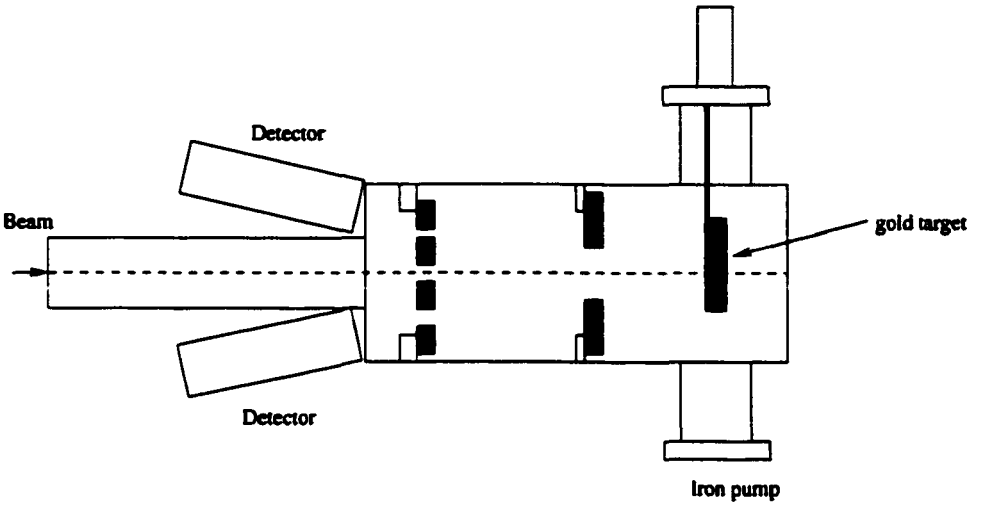

Figure 4.2: A schematic diagram of the Mott polarimeter at Jefferson Lab. Only two of the four detectors are shown. The other two are located directly opposite to these.

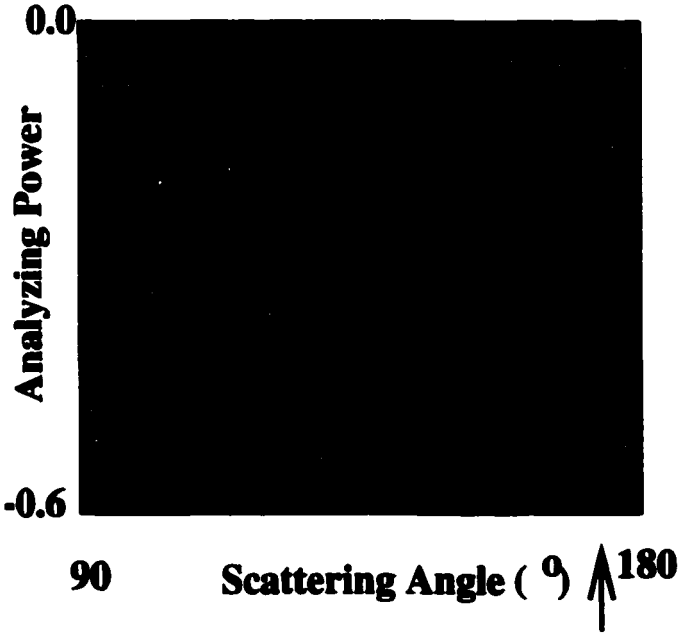

Figure 4.3: Analyzing power vs scattering angle for Mott scattering from 5 MeV electrons [105].

4.1.2 Hall A.

Figure 4.4 shows a sketch of experimental Hall A. The main portion of the hall is underground with a diameter of about 53 m. The waterfall target used for this experiment is placed in the scattering chamber located at the center of the Hall. The two high resolution spectrometers are shown in their standard configuration. Beam line equipment such as beam position monitors and beam current monitors are located along the beam line.

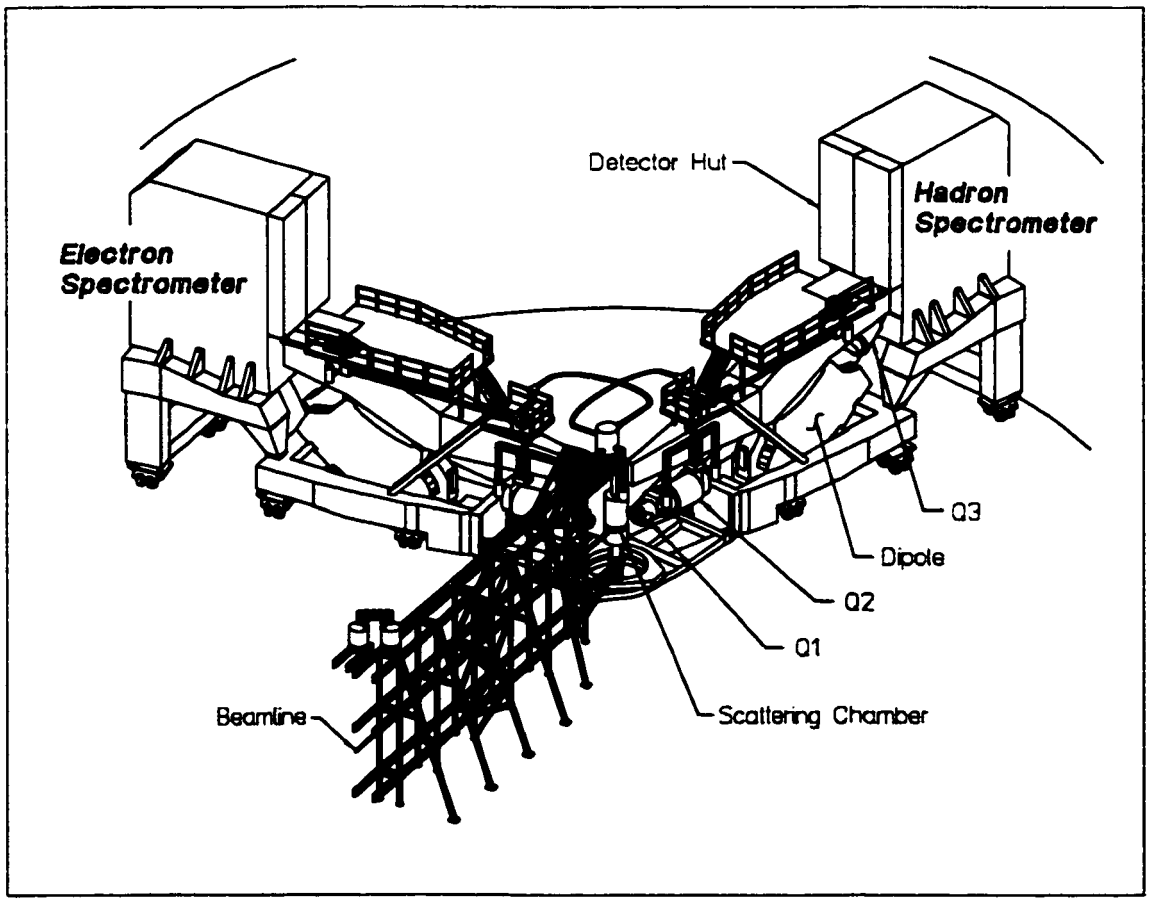

Figure 4.4: Experimental Hall A.

4.2 Target.

This experiment used a waterfall target with three identical thin water foils. By using water for the target, in addition to ^{16}O data, data from H is obtained as well. These H data were used to calibrate the FPP and also were used to measure the instrumental asymmetries of the FPP (see Chapter 5). Furthermore, we can measure the $\frac{G_E}{G_M}$ ratio for H using these data. This allows us to compare the proton form factor ratio for a proton inside the ^{16}O nucleus with that of a free proton, using the data from the same experimental setup and at the same kinematics. The waterfall target was built by a group from INFN [106]. The target ladder also contained ^{12}C, BeO and empty targets.

The three foils were at 30° to the incident beam. They were placed in such a way that scattered particles do not go through a second foil. Having three thin foils instead of one thick target had the advantage of minimizing the energy loss and straggling in the target without a loss of luminosity. The high y_{tg} (the reconstructed positions of the three foils from each spectrometer) resolution of the HRS pair allows a clear separation of the three foils (see Figure 5.9). This in turn allows us to clearly separate the states in ^{16}O. Furthermore, by reconstructing the interaction vertex to the same water foil using both spectrometers we could reduce the accidentals.

4.2.1 Design of the waterfall target.

A sketch of the waterfall target used for this experiment is shown in Figure 4.5. Three narrow slits were on top of the target chamber. Water was pumped down through these slits. When the water flows between the stainless steel poles it forms a thin foil on these poles, due to the surface tension. The entrance and exit windows of this target were made out of 3 mil Be , while the rest of the walls were made out of 1 mil stainless steel. The dimensions of the target are listed in Table 4.1.

Foil thickness	130 mg/cm^2
Foil width	12 mm
Pole size	2x2 mm
Separation of foils	22 mm

Table 4.1: Dimensions of the target.

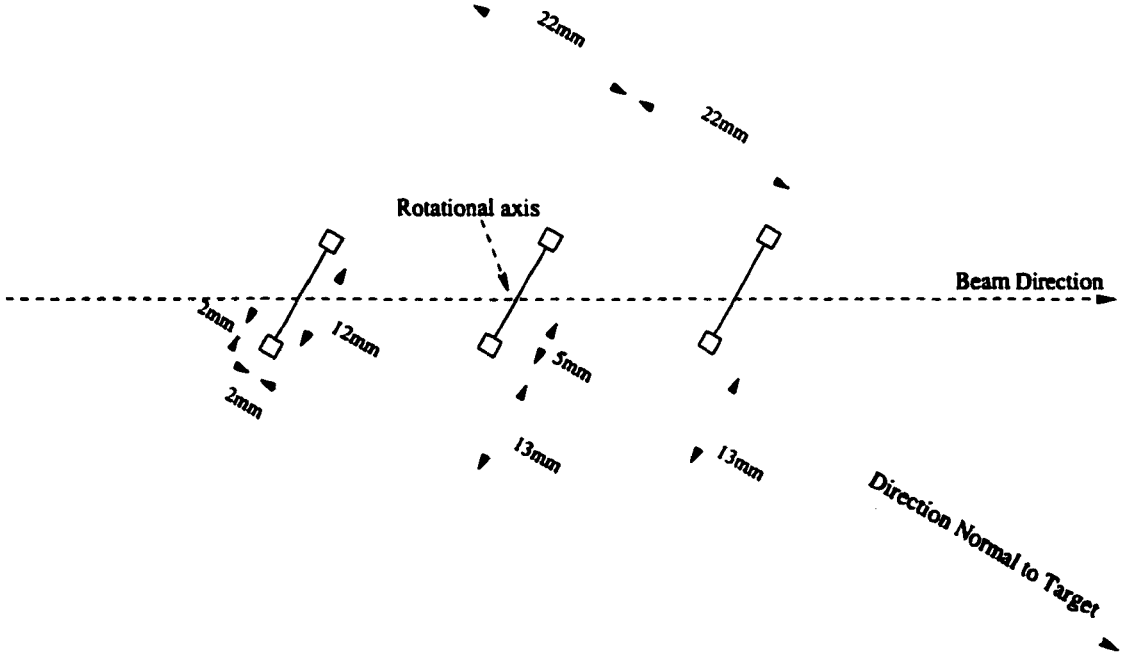

Figure 4.5: Sketch of the waterfall target configuration.

4.3 High Resolution Spectrometer (HRS) pair.

The Hall A HRS pair was used for the detection of the electrons and protons during this experiment. The two spectrometers are identical in design, each consisting of two focusing quadrupole magnets followed by a dipole magnet and then a defocusing

quadrupole magnet (Q1, Q2, D, Q3 system). Figure 4.6 shows a cross-sectional view of an HRS.

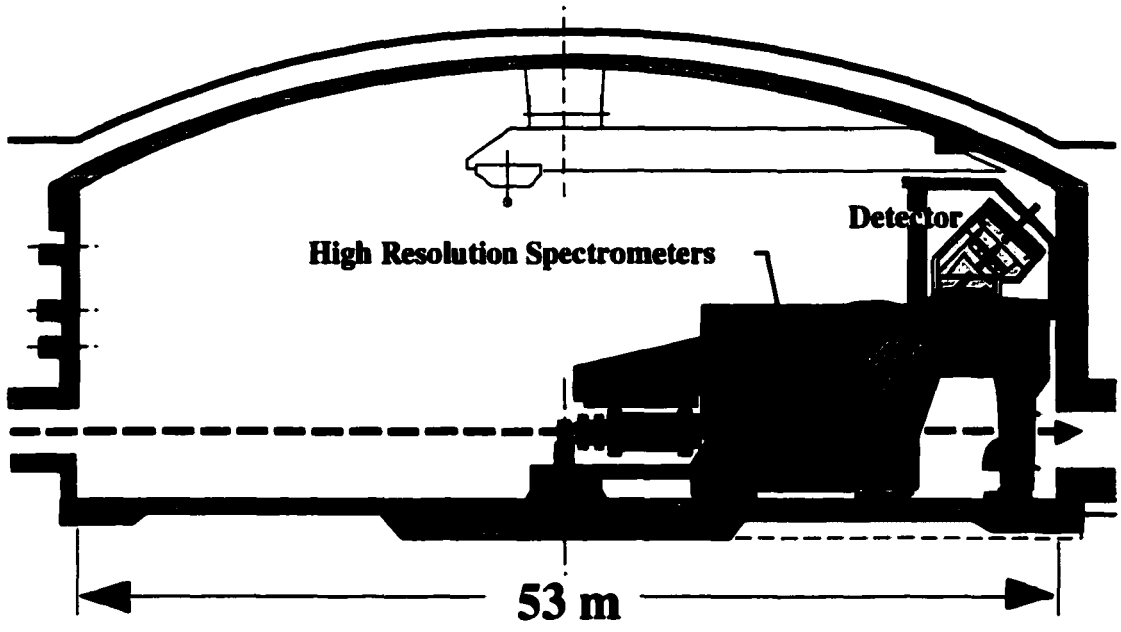

Figure 4.6: Cross-sectional view of an HRS.

Distance from the target to the sieve slit	118 cm
Momentum range	0.3 GeV/c to 4.0 GeV/c
Momentum resolution	2.5 x 10^{-4} FWHM
Momentum Acceptance	±4.5%
Angular Range (θ_e)	12^0 to 160^0
Maximum Solid Angle	7 msr
Optical length	23.4 m
Bend Angle	45^o
Angular Acceptances:	
Out of Plane (θ)	±50 mr
In Plane (ϕ)	±25 mr

Table 4.2: HRS parameters.

The magnet currents are remotely controlled by computers from the Hall A counting house. Detector packages for each of the HRS are installed inside the lead shielding house near the focal surface, after Q3. Table 4.2 lists some properties of the HRS pair.

4.3.1 HRSE focal plane array.

The electron arm focal plane detector array is shown in Figure 4.7. Of the electron arm focal plane detectors, only the Vertical Drift Chambers (VDC) and the two scintillator planes were used for this experiment. The two scintillator planes S1 and S2 were used to obtain the single arm trigger, while the VDC's were used to obtain the positions and angles of the particles at the focal plane.

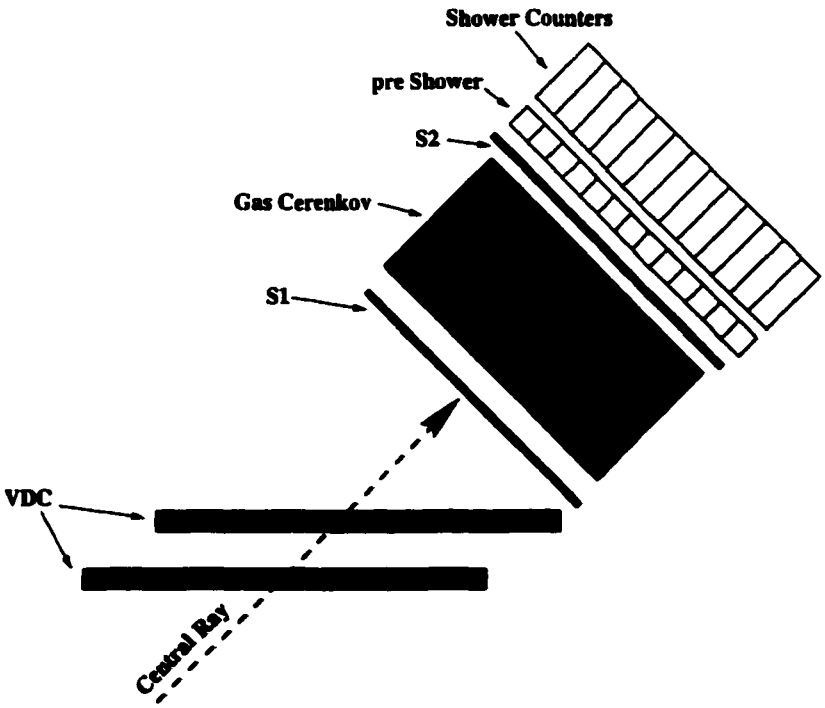

Figure 4.7: Electron-arm detector package, not to scale.

4.3.2 HRSH focal plane array.

Figure 4.8 shows the details of the hadron arm detector package. In addition to the VDC's and scintillators, we used the Focal Plane Polarimeter (FPP) in the Hadron arm to measure the polarization of the protons at the focal plane. Each of these detectors is described in the following sections.

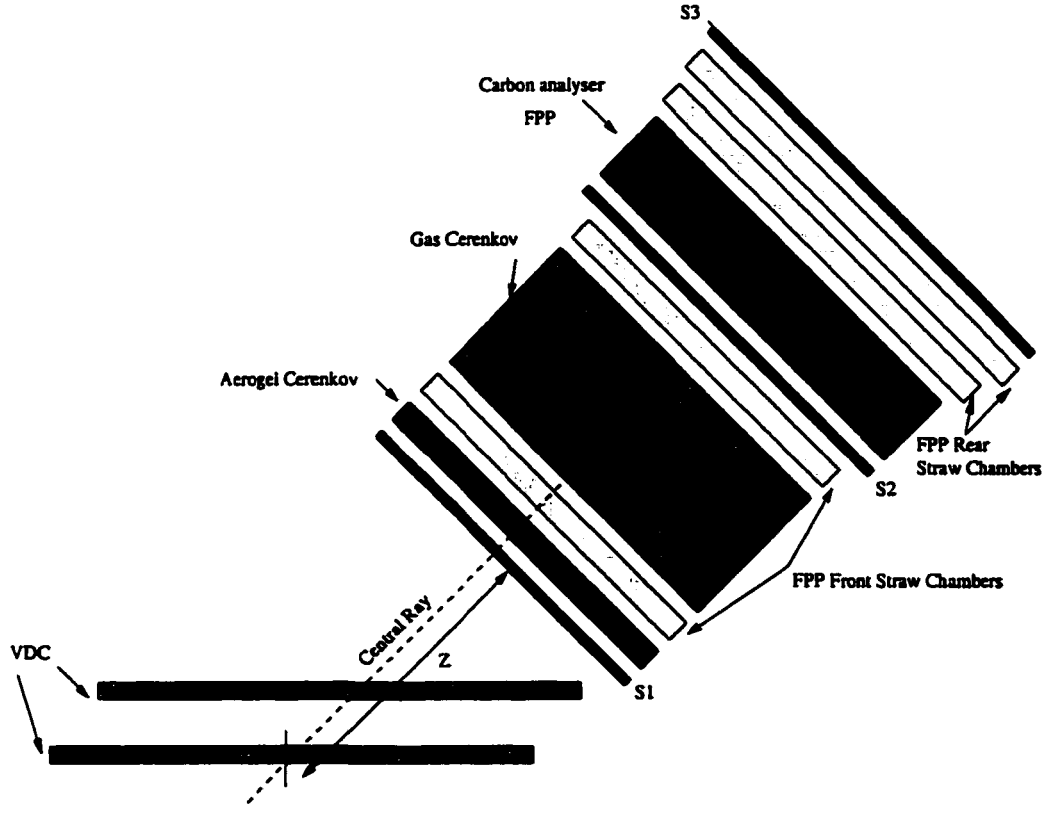

Figure 4.8: Hadron-arm detector package, showing the FPP, not to scale.

4.4 Vertical Drift Chambers for the HRS pair.

Each HRS uses an identical pair of Vertical Drift Chambers (VDC's) [107] to measure the position (x,y) and the angle (θ, ϕ) of the trajectory at the focal plane. A typical particle track passes through the VDC's at 45^0.

In each spectrometer, the lower wire plane of the lower VDC was positioned

near the ideal focal surface. The second VDC is located about 50 cm downstream of the first, offset in the dispersive direction by about 40 cm, so that the nominal central trajectory passes through the center of each VDC. The distance between the two VDC's acts as a long lever arm in the calculation of angles, resulting in high angular resolution.

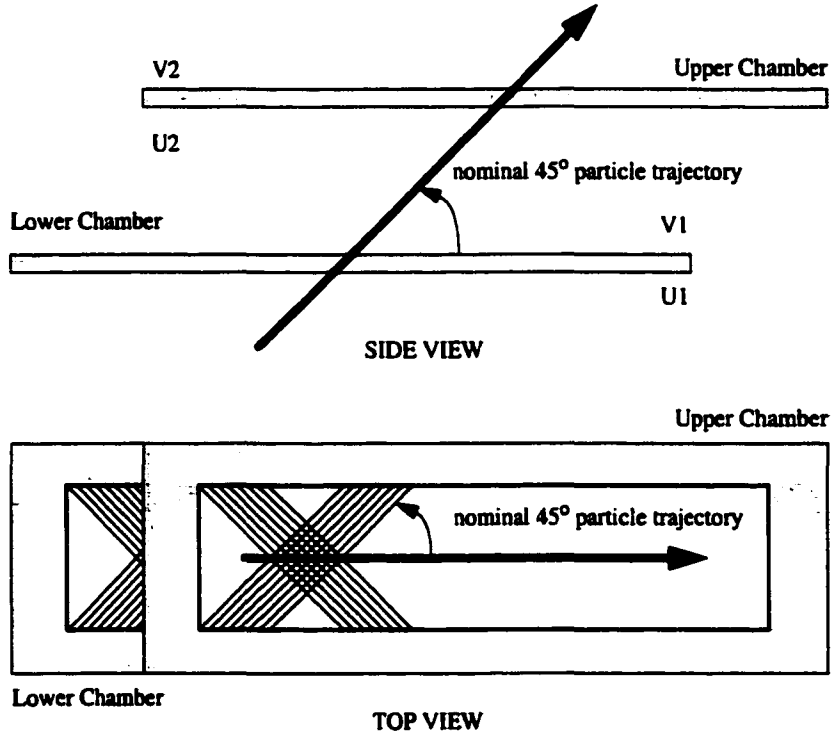

Figure 4.9: Side (top) and top (bottom) views of the VDC's.

Each VDC has two wire planes U and V which are at 45^0 to the dispersive direction as shown in Figure 4.9. These VDC's use negative high voltage for the cathode planes and the signal wires are at virtual ground. One important feature of these VDC's is that they do not have field-shaping guard wires, which allows these chambers to be operated at a lower voltage than in the case of a conventional VDC. The wire spacing and the chamber thickness are such that a 45^0 track will fire typically 5 wires of a plane, which improves the position resolution and yields a high reconstruction efficiency. Spectrometer acceptance fixes the maximum angle a

particle trajectory can have at 52^0. This extreme angle will cause at least three wires to fire.

The high voltage planes were made out of gold-plated mylar foil, and the wires were gold-plated tungsten. There are 368 wires in each plane separated by 6 mm. The wire positions were checked on a precision optical bench and found to be centered better than 50 microns for each wire. The gas mixture used was 65% Ar and 35% Ethane.

4.4.1 Read out system for VDC's.

When a charged particle passes through the VDC, it ionizes the Ar gas atoms, and leaves behind a track of electrons and ions. Due to the electric field between the high voltage plane and the wire, the electrons start drifting towards the wire. They will have a constant drift velocity until they come near the sense wire, where there is a radial 1/r field gradient. Here due to the higher kinetic energy they obtain, they ionize more gas atoms leading to an avalanche. This accumulated electron bunch is captured by the anode wire as a negative analog signal. This signal is transported to the preamp/discriminator cards where it is amplified and discriminated. The logic signal output from the discriminator is sent to multihit TDC's (time to distance converters), in common stop mode where the STOP comes from the trigger. The time data from the TDC are put into the data stream. This is depicted in Figure 4.10.

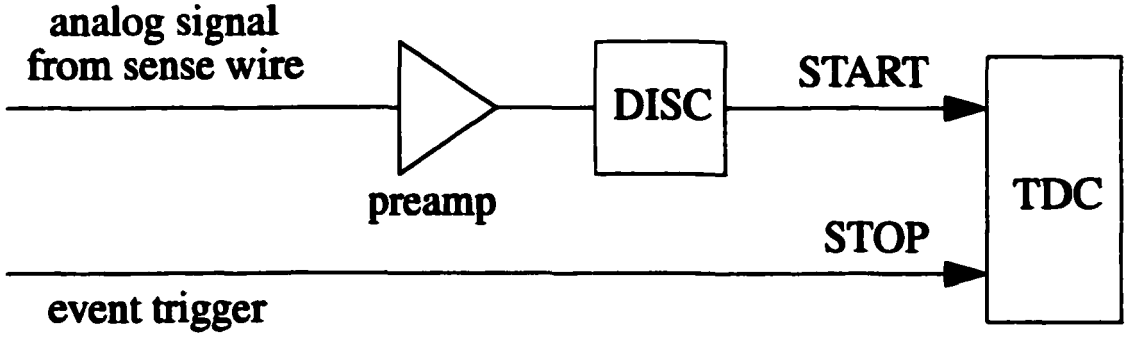

Figure 4.10: A block diagram of the electronics used for VDC's.

The drift time information is combined with the drift velocity of the electrons to calculate the perpendicular distances from the track to each wire that fired. The method of calculation is described in detail in Chapter 5.

4.5 Scintillators for the two spectrometers.

In both HRS's we used two scintillator planes S1 and S2 separated by 185 cm. Each scintillator paddle has two photo-multiplier tubes attached via light guides at each end of the paddle. The scintillator dimensions are listed in the Table below.

Scintillator plane	Number of paddles	paddle dimensions		
		Width	Length	Thickness
S1	6	29 cm	36 cm	0.5 cm
S2	6	36 cm	64 cm	0.5 cm

Table 4.3: Scintillator dimensions for the HRS.

4.6 Trigger Electronics.

When the electronics was deciding whether it was interested in an event or not, or when it was reading an event, new data needed to be inhibited so that the data being written does not get corrupted. Likewise, once the electronics had decided that an event was of interest, it needed a way to trigger the data acquisition system to read out the data. These jobs were done by the trigger electronics. Though there is a more involved trigger setup in Hall A now, for this experiment, a basic trigger was used as shown in Figure 4.11.

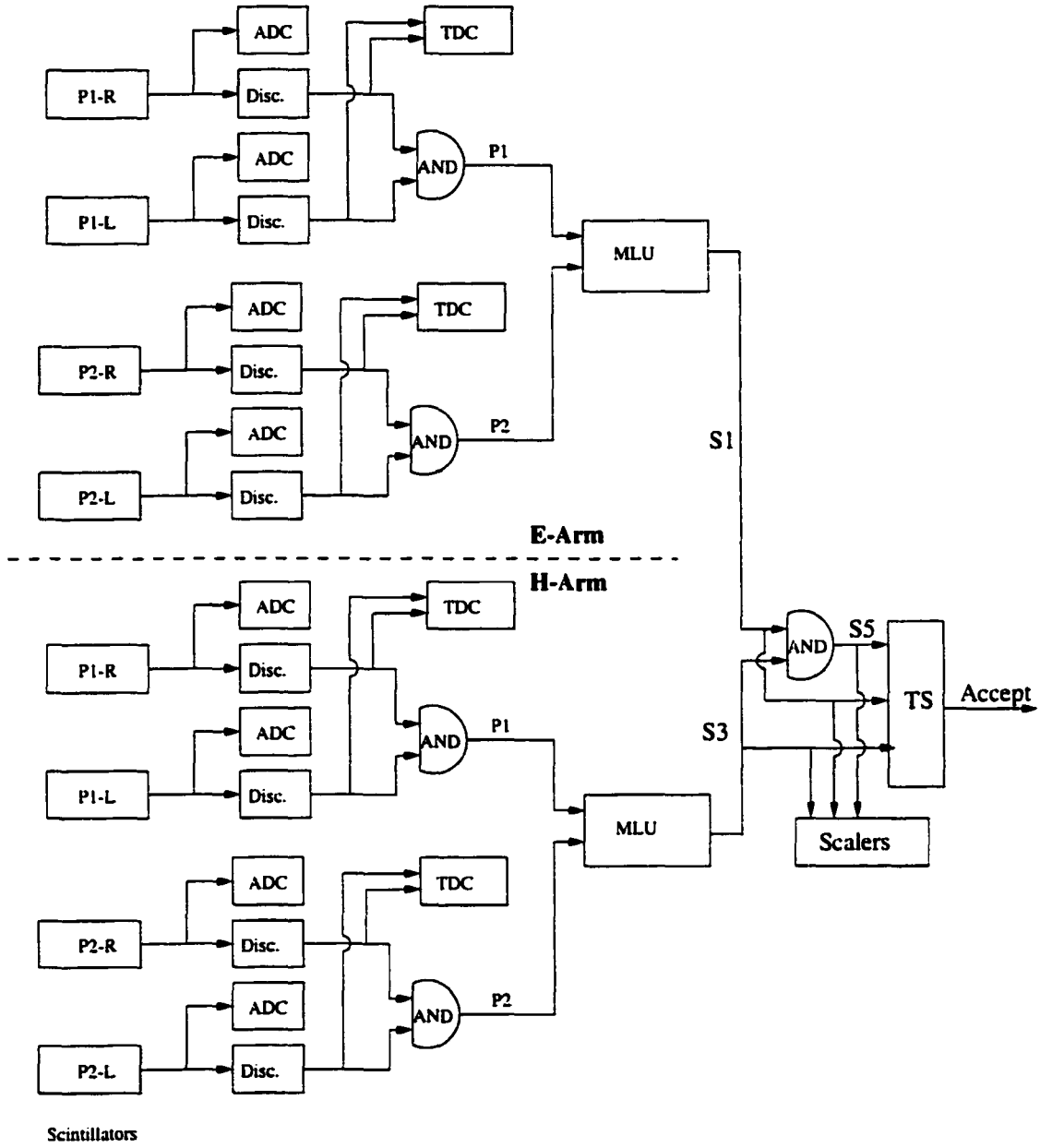

Figure 4.11: Simplified trigger electronics used for E89033. Here P1, P2 correspond to PMT's for S1 and S2 planes respectively and R and L represent right and left side of the scintillator.

4.6.1 Single arm trigger.

Single arm prescaled events are events randomly accepted from any one spectrometer, regardless of subsequent trigger logic. These are useful for diagnostic purposes and alignment of the FPP to the VDC's in the hadron spectrometer as well as to calculate focal plane efficiencies.

A single arm trigger is generated from the coincidence between the S1 and S2 planes and is used to signal the passage of a charged particle through the spectrometer. An acceptable hit from a scintillator paddle requires signals from both PMT's at each end of that scintillator paddle. The scintillator signals from the two planes are sent to a Memory Look Up Unit (MLU) which can be programmed to check whether the signals from the two planes are in coincidence and whether they correspond to a track which is approximately parallel to the central ray. If these conditions are satisfied it will generate the S1 singles trigger from the electron spectrometer and the S3 singles trigger from the hadron spectrometer.

4.6.2 Coincidence trigger.

The two singles triggers, S1 and S3 are sent to an overlap AND circuit to form a coincidence trigger, S5.

All three types of triggers are then sent to a scaler unit for counting and to a Trigger Supervisor (TS) unit. This unit has a prescale function and an MLU function. When a trigger arrives at the TS, the prescale function scales the signal by a prescale factor set by the experimenter (for example, if the prescale factor for S1 trigger type is 1000, it will ignore the first 999 S1 triggers and will accepts only the 1000^{th} S1 trigger). The MLU function of the TS acts on the prescaled events. When a trigger arrives, the TS checks whether the data acquisition system is "dead" (busy writing data) or "alive". If it is "alive", the TS accepts the trigger and signals to write data. Once a trigger is accepted, the data acquisition system is dead for about 700 μs. Thus, in the case of a coincidence event, if one of the two singles triggers arrive at the

TS before the coincidence trigger, then the singles trigger would be accepted and the coincidence information would be lost. In order to avoid this, all singles triggers are delayed by 30 ns with respect to the coincidence trigger. As a result, the coincidence trigger and not the singles triggers that generated it is guaranteed to be accepted.

4.7 HRSH Focal Plane Polarimeter.

The central piece of equipment for this experiment was the Focal Plane Polarimeter (FPP) which was located at the focal plane of the High Resolution Hadron Spectrometer. The FPP was used to measure the polarization of the proton at the focal plane. The FPP statistically measures the polarization of the proton by secondary scattering off an analyzing medium. If the proton interacted with a nucleus of the analyzer medium via the nuclear force, due to the nuclear spin-orbit force, then the proton is scattered asymmetrically. This asymmetry is proportional to the polarization of the proton. By measuring the asymmetry, we determine the components of the polarization of the proton normal to its momentum direction. A proton can scatter off a nucleus in the analyzer by a Coulomb or a nuclear interaction. We are only interested in the nuclear scattered events. However, most of the events are Coulomb scattered events which have no analyzing power. The probability of scattering a proton via the Coulomb interaction is sharply peaked at very low polar angles, *i.e.*, at about one or two degrees. In contrast, the probability of scattering a proton via the nuclear interaction has a broad angular distribution (θ_{fpp}) extending up to about 40^o in polar angle. However, the cross section drops off rapidly when you go to higher polar angles (see Figure 4.12).

The FPP in Hall A was built by a collaboration from Rutgers University, College of William and Mary, Norfolk State University, and University of Georgia. Figure 4.8 shows the FPP. It consist of a carbon analyzer and four straw chambers. The Carbon analyzer is sandwiched between the two front chambers and the two rear

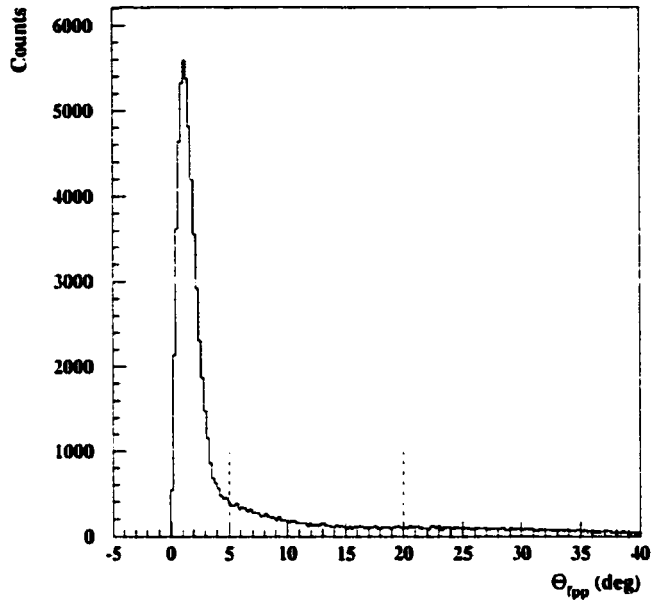

Figure 4.12: Number of counts vs. scattering angle θ_{fpp} obtained from data. The dashed lines show the θ_{fpp} angular range used for the analysis of the present data.

chambers, allowing the tracks to be determined before and after scattering from the analyzer. The FPP was commissioned in the Spring of 1997, just before the present experiment, at three different time periods.

4.7.1 Some characteristics of the Hall A FPP.

1. The angular resolution of the FPP chambers is about 4 mr.
2. Multiple scattering from graphite of thickness 9 inches is about 17 mr.
3. Due to the very large acceptance of the rear chambers, there is only a very few events that fail the "cone test" (the ability to detect the events in the full cone of the scattered track from the rear chambers) for scattering angles between 5^0 and 20^0, for about 450 MeV protons.
4. The efficiency (ratio of the number of acceptable events scattered from the carbon analyzer to that of the incident particles) is approximately 10% for 450 MeV protons with a carbon thickness of 9 inches.

4.7.2 FPP carbon analyzer.

The thickness of the carbon analyzer used depends on the energy of the incident proton and has a major effect on the efficiency of the polarimeter. The carbon analyzer must be thin enough so that the multiple Coulomb scattering angles (which lead to less certainty in the vertex reconstruction and therefore in the scattering angle) are smaller than the scattering angles for nuclear scattered events. However, we know that the thicker the analyzer, the higher is the probability to get nuclear scattered events. In our analysis we rejected events scattered at angles less than 5^0 in polar angle, which is ample to reject most of the Coulomb scattered events.

The carbon analyzer built for Hall A FPP uses 5 independent, remotely controllable carbon blocks to adjust the analyzer thickness so that the FPP can be optimized for a range of proton energies. The block thicknesses are : 9", 6", 3", 1.5" and 0.75" in order from front to back. Each block is vertically split in the middle with a 45 degree cut, and has two sections that open to the sides. These carbon blocks are operated remotely through EPICS. We used the 6" and the 3" carbon blocks combined throughout this experiment. We chose 6" and 3" carbon blocks together rather than using the 9" carbon, since the former combination is closer to the rear chambers, allowing the rear FPP chambers to detect the scattered events that lie in the full cone of the scattered tracks. We used the polar angle range of 5^0 to 20^0 for the analysis of FPP data.

4.7.3 FPP straw chambers.

A straw chamber is a set of cylindrical tubes, with a thin wire running along the central axis of each tube (straw). The Hall A FPP straw chambers have the wire at positive high voltage relative to the straw. These straws were built by wrapping a 10 micron thick aluminum foil and two 2 mil thick mylar layers with heat setting glue around a 0.5 cm radius mandril. Each tube is individually supplied with gas. The central wire is 1 mil in diameter, gold-plated tungsten with a few percent rhenium.

The centering of the wire in the straw has a precision of 3 mil (σ). The wires were strung at a tension of 43 grams. The high voltages for the wires were supplied by the Lecroy 1463 HV modules. We operated the chambers at about a high voltage of 1900 V for each wire.

When a charged particle goes through a straw, it ionizes gas atoms in the straw. The electrons then drift towards the central wire, which is at a positive HV with respect to the straw wall, while positive ions move towards the straw wall. We used a 65% Argon / 35% ethane gas mixture (same as for the VDC's). For this gas mixture the electron drift velocity is about 50 microns per ns. Therefore, for the straw radius of 0.5 cm, the maximum drift time is about 100 ns. The mean free path of electrons in this kind of gas is about 10^{-6}m. Therefore the electrons are continuously colliding with the gas atoms while moving towards the anode, giving a constant drift velocity for a large range of electric fields. When the electrons get near the wire, due to the large field gradient of the 1/r electric field, electrons accelerate giving them more energy to ionize more gas atoms, thus creating an avalanche of electrons. This gives rise to an electric signal with a considerable negative voltage. When this analog signal is received by the readout boards, it is preamplified by about 21 times, then it is discriminated to give a logic pulse. Finally the signal is multiplexed into groups of 8 as a logic pulse which has a different pulse width for each of the eight wires in the group. At the boards the pulse voltage is kept small to avoid picking up noise while being transported. Finally a pulse of amplitude 45 mV is sent in to the level shifter cards. At the level shifter this becomes a logic signal of amplitude 800 mV. This is sent to the TDC modules in the FASTBUS crate and their output is added to the data stream. A block diagram showing the electronics used for this is shown in Figure 4.13.

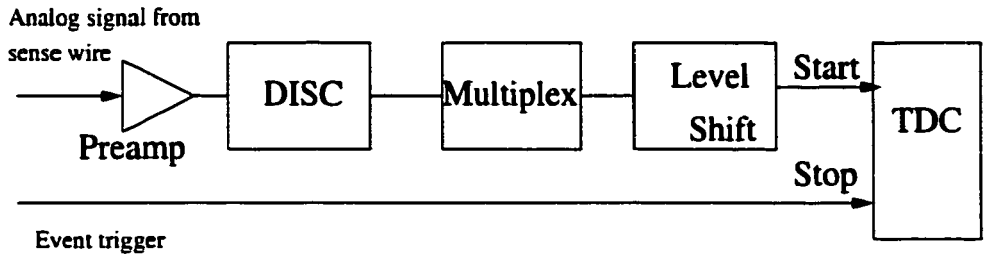

Figure 4.13: Block diagram for the logic used for FPP signals.

When the leading edge of this signal is received at the TDC, it starts the TDC clock. When the scintillator trigger signal comes the clock stops (we have common stop TDC's). The time difference between these two is the drift time. The time difference between the leading edge and the trailing edge of the chamber signal determines the wire number in that wire group of eight. Figures 5.13, and 5.11 show a typical drift time and demultiplex spectra from FPP respectively.

Physical description of the chamber.

Each chamber has 6 straw planes which are positioned normal to the spectrometer's nominal central trajectory. The two front chambers are identical in design, having three "v" planes and three "u" planes each. The "u" and "v" planes are perpendicular to each other and the "u"planes make an angle of 45^0 with the x (dispersive) direction. Chamber 3 has two "u", two "v", and two "x" planes, while chamber 4 has three "u" and three "v" planes (see Figure 4.14). In the front chambers, for both "u" planes and "v" planes, going from one layer to the next, the middle straw layer was offset by half a straw, while for the rear chambers each straw layer was offset by half a straw in the same direction.

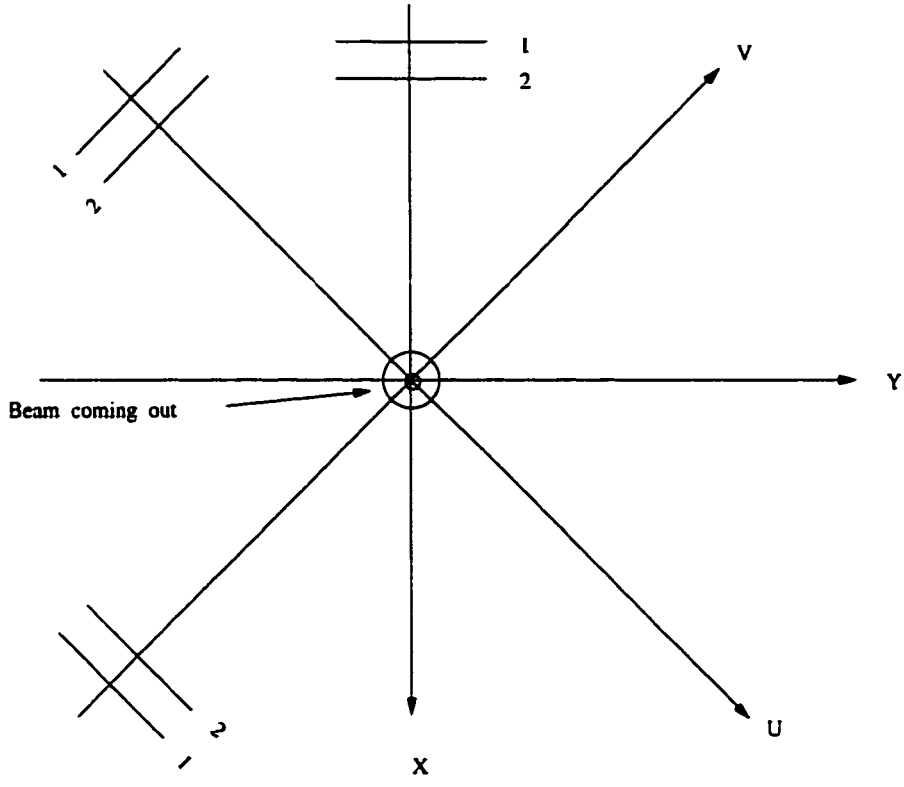

Figure 4.14: The coordinate system and the first straws of the planes.

Chamber	Ch. 1	Ch. 2	Ch. 3	Ch. 4
Active length(cm)	209.0	209.0	267.5	292.2
Active width(cm)	60.0	60.0	122.5	140.6
Wire spacing(cm)	1.095	1.095	1.0795	1.0795

Table 4.4: Dimensions of the FPP straw chambers.

Chamber	Plane	# of straws	Z distance (cm)	Distance to first straw from center(cm)
Chamber 1	FV1	160	184.867	80.777
	FV2	160	185.815	81.325
	FV3	160	186.763	80.777
	FU1	176	191.423	100.442
	FU2	176	192.371	100.990
	FU3	176	193.319	100.442
Chamber 2	FV4	160	301.247	80.506
	FV5	160	302.195	81.054
	FV6	160	303.143	80.506
	FU4	176	307.803	102.149
	FU5	176	308.751	102.696
	FU6	176	309.699	102.149
Chamber 3	RU1	239	394.767	134.422
	RU2	239	395.697	133.882
	RV1	239	396.791	123.247
	RV2	238	397.721	122.707
	RX1	246	398.815	141.381
	RX2	245	399.745	140.841
Chamber 4	RU3	276	431.577	152.937
	RU4	276	432.507	153.477
	RU5	276	433.437	154.017
	RV3	276	434.511	138.689
	RV4	276	435.441	138.149
	RV5	276	436.371	137.610

Table 4.5: Dimensions and parameters of straw planes. Note that the planes are listed in order of increasing Z coordinate.

Chapter 5

Data Analysis.

In this chapter we describe the procedure for determining physically meaningful quantities from the raw data information. We can think of the data analysis as having four principal parts:

1. Determination of the kinematics for each event.
2. Determination of asymmetries of the secondary scattering at the focal plane.
3. Placement of cuts on the data to ensure data quality.
4. Calculating the polarization observables at the target.

For each event we first calculate the coordinates and angles at the focal plane using the VDC raw wire hits and drift times. This will tell us the trajectory of the particle at the focal plane. Then we can transport this trajectory back to the target using the knowledge of the optics for the two spectrometers. Since we know the momentum and the coordinates at the target, we can determine the kinematics of the event.

Secondly, from the Focal Plane Polarimeter straw chamber information we can determine the incident and the scattered tracks from the carbon analyzer. From the front two chambers we can determine the trajectory incident on the carbon analyzer

and from the rear two chambers the scattered trajectory. From these two tracks we can determine the polar and the azimuthal angles for each event that scattered from the carbon analyzer. This can be used to calculate the asymmetry at the focal plane and therefore the polarization observables at the focal plane.

In obtaining the above-mentioned observables from the raw data, we have to apply cuts on the data to ensure the integrity of the data. Cuts such as transverse position measured at the target (y_{tg}) and corrected coincidence time of flight (tc_{cor}) to select coincident events that start from the target; and cuts like VDC-multiplicity, VDC-position to make sure they are good VDC events and polarimeter cuts such as θ_{fpp}, zclose, helicity and the cone-test to ensure good FPP events. We discuss each of these aspects of the analysis in this chapter.

5.1 Scintillator Analysis.

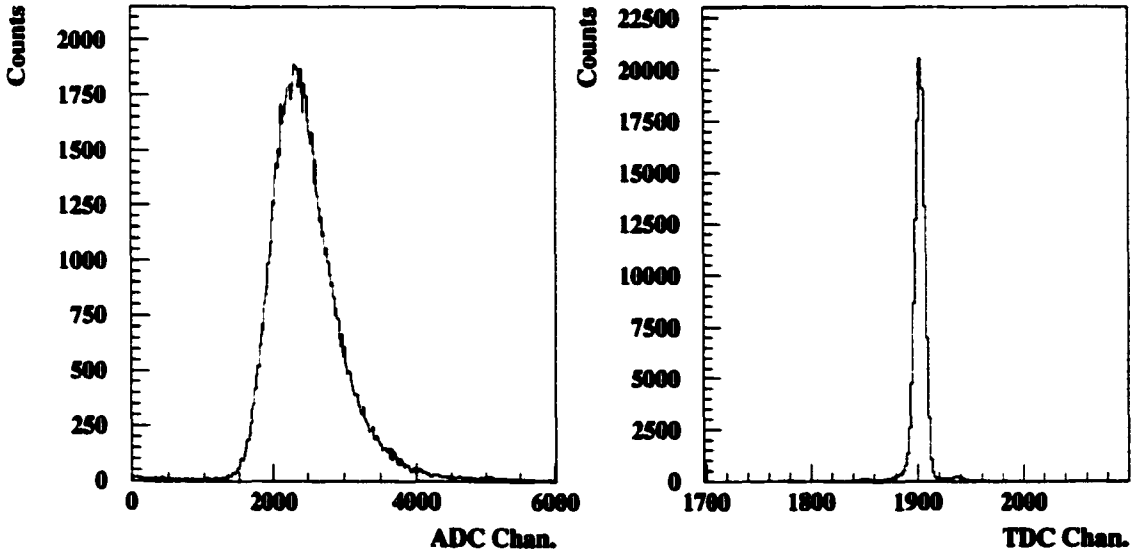

Figure 5.1: ADC and TDC spectra from a scintillator paddle.

TDC and ADC information are provided for the photo-tubes at each end of a scintillator paddle in each plane for both spectrometers. Figure 5.1 shows typical

ADC and TDC spectra for a scintillator paddle. The pulse height of the ADC signal is a measure of how much energy is deposited by the particle while passing through the scintillator material. The descriminator thresholds for the photo-multiplier tubes (PMT) were set before the experiment, so that they were high enough to eliminate noise but low enough not to lose real events. As mentioned before, the coincidence trigger was formed from the coincidence of the two single arm triggers.

5.2 VDC Analysis.

For both spectrometers, the VDC analysis was performed in the same manner. From the drift time information we first determined the perpendicular drift distance for a particular sense wire from the track. Figure 5.2 shows a standard drift time spectrum from a VDC plane.

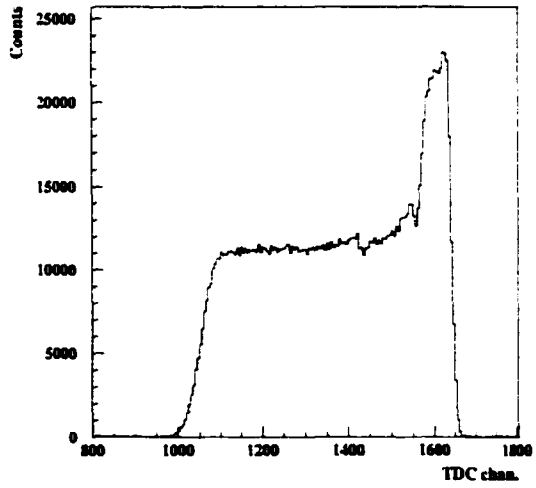

Figure 5.2: Number of counts vs. drift time.

Three regions are apparent in the spectrum; the peak, the plateau and the tail all arise due to geometric effects. The number of counts in an interval of the drift-time spectrum is given by

$$\frac{dN}{dt} = \frac{dN}{ds}\frac{ds}{dt}, \tag{5.1}$$

where s is the length of the path traveled by the drift electron. The drift velocity, ds/dt, is essentially constant, except very close to the wire. dN/ds is the effective flux through the drift line.

Let us consider that the flux of tracks through the chamber to be ϕ. Since the typical angle of tracks through Hall A VDC's is 45^0, the effective flux, (dN/ds) in the parallel field region is ϕ (sin45^0) (see Figure 5.3). Thus the number of counts per channel in the parallel field region comes out to be

$$\frac{dN}{dt} = \frac{1}{\sqrt{2}}\phi\frac{ds}{dt}. \tag{5.2}$$

In the radial field region, the closest drift path from a 45^0 track to the wire is a field line oriented at 45^0 to the wire plane. As a result, in the radial region the tracks are perpendicular to the drift paths and hence the effective flux is ϕ. This gives rise to the peak in the drift time spectrum with approximately $\sqrt{2}$ times more counts per channel in the radial field region than in the parallel region. The reason for this to appear in the highest TDC channel region in the spectrum is that we use common stop mode TDC's. The tail of the spectrum occurs from the high drift time region since the active cell volume decreases close to the high-voltage plane.

5.2.1 Determination of VDC coordinates.

For a typical track, there are about five sense wire signals. A linear fit to the corresponding five perpendicular distances allows us to determine the intersection point (cross-over point) of the track with the wire plane (see Figure 5.4).

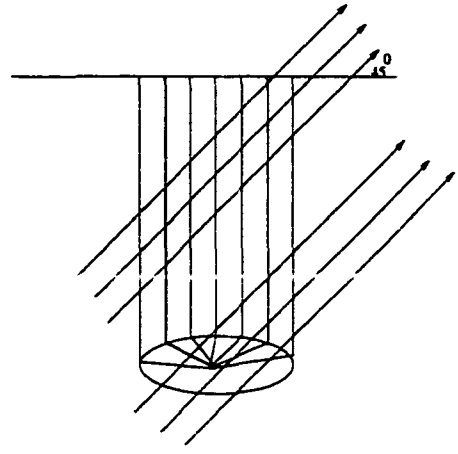

Figure 5.3: Field lines and particle tracks through a VDC plane. The incident particles come at an angle of 45^0 to the VDC wire plane.

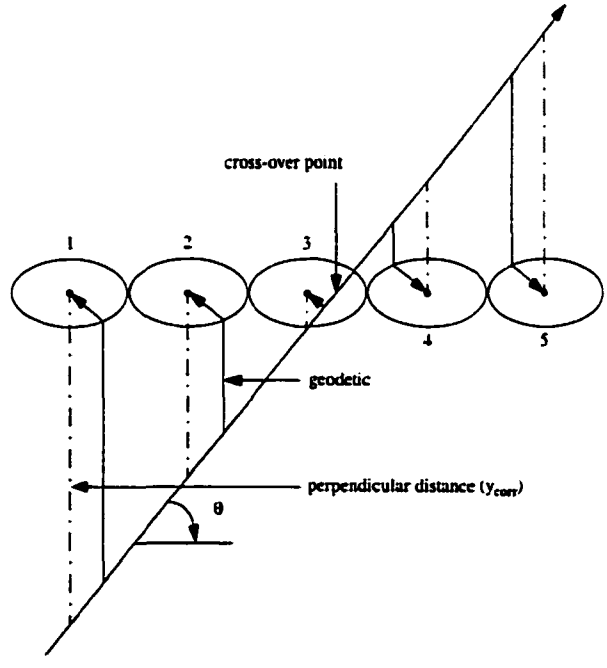

Figure 5.4: A trajectory through one of the VDC wire planes. The geodetic is the shortest drift time. See text for details.

The fit to the perpendicular distances at each plane results in a position coordinate (u or v) and an angular coordinate (du/dz, dv/dz) for the plane. Using the

long lever arm between the two chambers, global angles ($\eta 1$ and $\eta 2$) can be calculated more accurately than the local angles using,

$$\tan \eta 1 = \frac{u2 - u1}{d1} \tag{5.3}$$

$$\tan \eta 2 = \frac{v2 - v1}{d1}. \tag{5.4}$$

However, the local angles were useful in optimizing the drift velocities and as a consistency check for the global angles. The detector coordinate system is defined on the u1 plane (focal surface) as shown in Figure 5.5. Therefore, the v1 coordinate is projected onto the u1 plane by the following

$$v = v1 - d2 \tan \eta 2 \tag{5.5}$$

$$u = u1. \tag{5.6}$$

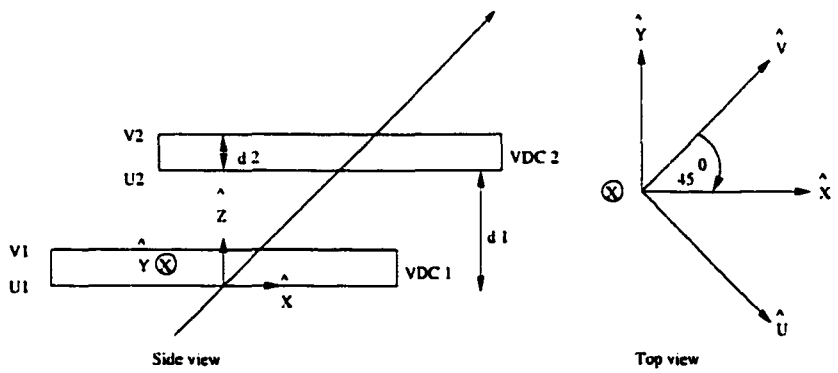

Figure 5.5: VDC coordinate system with respect to the detector hut system.

5.2.2 Determination of Focal plane coordinates.

Detector hut coordinate system.

Next we have to convert the (u, v, z) coordinates measured in the VDC system into the detector hut coordinate system (x, y, z) shown in Figure 5.5. Details of the

transformation can be found in [109]. This transformation is given by,

$$\tan\theta_{\rm det} = \frac{1}{\sqrt{2}}(\tan\eta 1 + \tan\eta 2) \tag{5.7}$$

$$\tan\phi_{\rm det} = \frac{1}{\sqrt{2}}(-\tan\eta 1 + \tan\eta 2) \tag{5.8}$$

$$x_{\rm det} = \frac{1}{\sqrt{2}}(u + v) \tag{5.9}$$

$$y_{\rm det} = \frac{1}{\sqrt{2}}(-u + v). \tag{5.10}$$

Transport coordinate system.

The transport coordinate system is obtained by rotating the detector hut system clockwise around its y axis by 45.1^0, as follows:

$$\theta_{\rm tra} = \frac{\theta_{det} + \tan\rho_0}{1 - \theta_{\rm det}\tan\rho_0} \tag{5.11}$$

$$\phi_{\rm tra} = \frac{\phi_{det}}{\cos\rho_0 - \theta_{\rm det}\sin\rho_0} \tag{5.12}$$

$$x_{\rm tra} = x_{\rm det}\cos\rho_0(1 + \theta_{\rm tra}\tan\rho_0) \tag{5.13}$$

$$y_{\rm tra} = y_{\rm det} + \sin\rho_0\phi_{\rm tra}x_{\rm det}. \tag{5.14}$$

Here ρ_0 is the rotation angle, -45.1^0; See Fig 5.6.

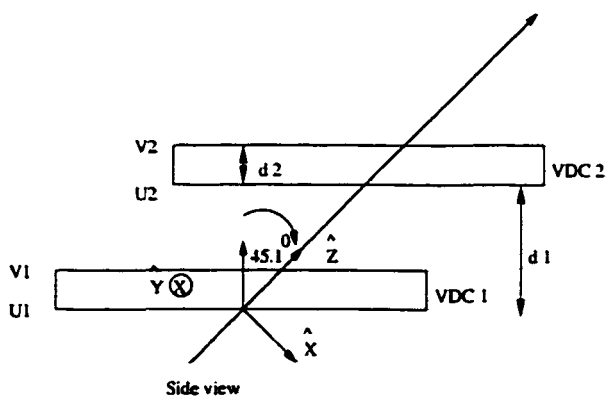

Figure 5.6: Transport coordinate system.

5.3 Focal plane to target coordinate calculation.

Having determined the focal plane coordinates (two angles and two positions) the spectrometer optics tensor is used to calculate the target coordinates. For a schematic diagram showing the target and focal plane coordinate systems, see Figure 5.7. The spectrometer optics tensor maps the focal plane coordinates $(x_{fp}, y_{fp}, \theta_{fp}, \phi_{fp})$ into the target coordinates $(x_{tg}, y_{tg}, \theta_{tg}, \phi_{tg}, \delta)$ and is generated by an optics optimization procedure described in the following section.

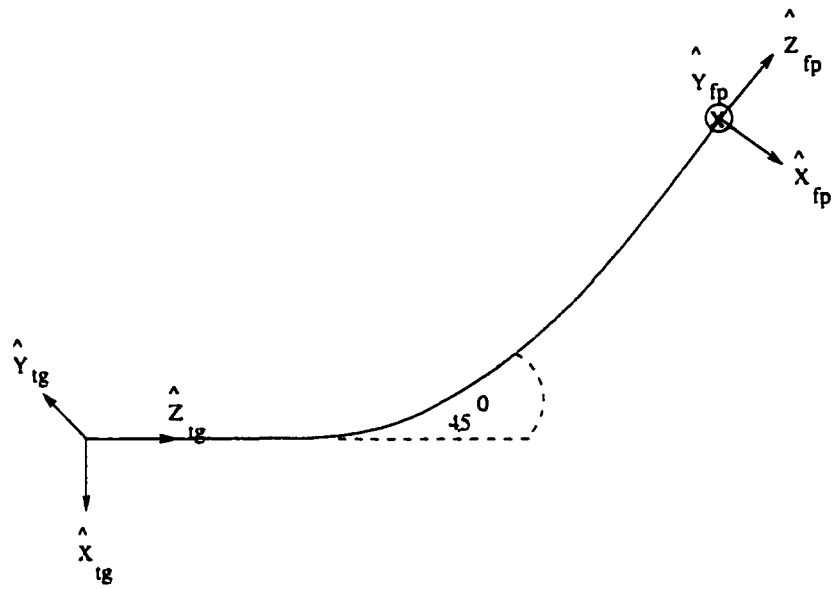

Figure 5.7: Coordinate systems at the target and at the focal plane.

The units used for these matrix elements are meters for distances (x,y), radians (rad) for angles (θ, ϕ) and units of percent for relative momentum δ.

The Focal-plane Coordinate System (FCS) is defined by the spectrometer optics. This does not necessarily coincide with the detector coordinate system based on the VDC's due to various misalignments of the VDC's. Therefore the transformation from the VDC coordinate system to the FCS includes corrections to VDC misalignments which are represented by offset matrix elements and are determined during the optics optimization procedure. The following equations are with the offsets added to

these focal plane variables.

$$y_{fp} = y_{tra} - \sum y_{i000}\, x_{fp}^{i} \tag{5.15}$$

$$x_{fp} = x_{tra} \tag{5.16}$$

$$\theta_{fp} = \frac{\theta_{det} + \tan\rho}{1 - \theta_{det}\tan\rho} \tag{5.17}$$

$$\phi_{fp} = \frac{\phi_{det} - \sum p_{i000} x_{fp}^{i}}{\cos\rho - \theta_{det}\sin\rho}. \tag{5.18}$$

Here ρ is the angle between the local central ray and the z axis of the detector hut coordinate system and is given by $\tan\rho = \sum t_{i000} x_{fp}^{i}$ (see fig 5.8).

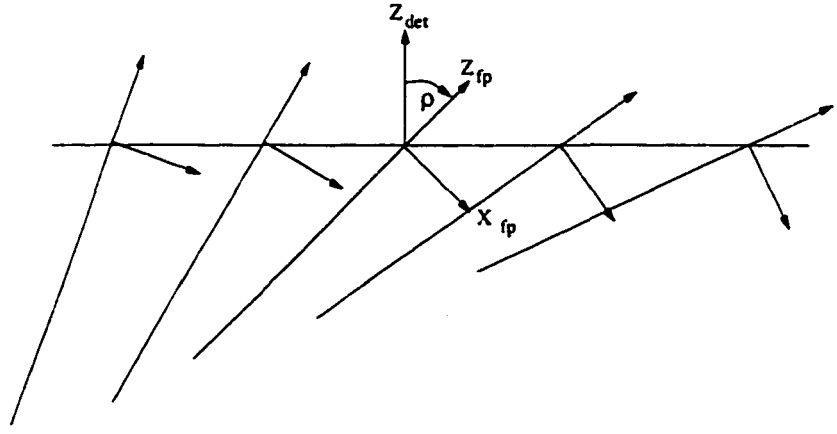

Figure 5.8: Focal plane coordinate system (rotated) along the dispersive direction.

Optics optimization.

Only a brief outline of the optics optimization is given here. For a detailed description of the calibration of the Hall A HRS pair, see Reference [112] and [113]. The tensor elements obtained for the two HRS prior to this experiment are given in Appendix E.

We measure only four quantities at the focal plane, but we have five unknowns at the target. Therefore during the optics commissioning runs the vertical position at the target (x_{tg}) was set to zero by making sure the beam position at the target

in x direction is always within 200 μm. In a first-order approximation, we can relate the target quantities to the focal plane quantities by the following matrix:

$$\begin{bmatrix} \delta \\ \theta \\ y \\ \phi \end{bmatrix}_{tg} = \begin{bmatrix} <\delta \mid x> & <\delta \mid \theta> & 0 & 0 \\ <\theta \mid x> & <\delta \mid \theta> & 0 & 0 \\ 0 & 0 & <y \mid y> & <y \mid \phi> \\ 0 & 0 & <\phi \mid y> & <\phi \mid \phi> \end{bmatrix} \begin{bmatrix} x \\ \theta \\ y \\ \phi \end{bmatrix}_{fp} . \tag{5.19}$$

Here, the null matrix elements result from the mid-plane symmetry of the spectrometer. In order to obtain the desired high resolution for Hall A spectrometers the optimization is performed to the fifth order in focal plane coordinates.

A set of tensors Y_{jkl}, T_{jkl}, P_{jkl} and D_{jkl} connect the focal plane coordinates to the target coordinates by the following equations:

$$y_{tg} = \sum_{j,k,l} Y_{jkl} \theta_{fp}^{j} y_{fp}^{k} \phi_{fp}^{l} \tag{5.20}$$

$$\theta_{tg} = \sum_{j,k,l} T_{jkl} \theta_{fp}^{j} y_{fp}^{k} \phi_{fp}^{l} \tag{5.21}$$

$$\phi_{tg} = \sum_{j,k,l} P_{jkl} \theta_{fp}^{j} y_{fp}^{k} \phi_{fp}^{l} \tag{5.22}$$

$$\delta = \sum_{j,k,l} D_{jkl} \theta_{fp}^{j} y_{fp}^{k} \phi_{fp}^{l}. \tag{5.23}$$

Here each tensor element Y_{jkl}, T_{jkl}, P_{jkl}, D_{jkl} is a polynomial in x_{fp}, for example,

$$Y_{jkl} = \sum_{i=1}^{m} C_i x_{fp}^{i}. \tag{5.24}$$

Again, the mid-plane symmetry of the spectrometer requires that for non-zero Y_{jkl} and P_{jkl}, (k+l) is odd, while for D_{jkl} and T_{jkl}, (k+l) is even.

To obtain these tensor elements, a χ^2 minimization was performed on the four

difference distributions defined by

$$\Delta(y) = \sum_{s} \frac{[\sum_{j,k,l} Y_{jkl}\, \theta_{fp}^{j}\, y_{fp}^{k}\, \phi_{fp}^{l} - y_{tg}^{0}]^2}{\sigma_y^s} \tag{5.25}$$

$$\Delta(\theta,\phi) = \sum_{s} \frac{[\sum_{j,k,l} T_{jkl}\, \theta_{fp}^{j}\, y_{fp}^{k}\, \phi_{fp}^{l} - \theta_{tg}^{0}]^2}{\sigma_\theta^s} + \sum_{s} \frac{[\sum_{j,k,l} P_{jkl}\, \theta_{fp}^{j}\, y_{fp}^{k}\, \phi_{fp}^{l} - \phi_{tg}^{0}]^2}{\sigma_\phi^s} \tag{5.26}$$

$$\Delta(\delta) = \sum_{s} \frac{[\sum_{j,k,l} D_{jkl}\, \theta_{fp}^{j}\, y_{fp}^{k}\, \phi_{fp}^{l} - \delta_{tg}^{0}]^2}{\sigma_\delta^s}. \tag{5.27}$$

Here, σ's correspond to the resolutions of the relevant difference distributions.

The optimization of optics used for this analysis was performed by the thesis students of the experiment 89003, using data taken just before the run-time of this experiment. First the y optimization was performed, then the optimization of the two angles θ and ϕ were performed, finally the relative momentum optimization was performed. The optics optimization was performed using (e e') elastic scattering from a thin ^{12}C target. For the angle optimization, a sieve slit with 49 holes each of diameter 2 mm was positioned at the entrance to the spectrometer in front of Q1. For the relative momentum optimization, the field setting of the spectrometer was tuned and the relative dipole field ΔB/B was changed from -4.5% to 4.5% in steps of 1.5%, so that the elastic peak of ^{12}C (e, e') was shifted along the dispersive direction.

Absolute momentum calibration of the HRS.

The absolute momentum calibration is described in detail in Ref. [111]. Only a brief discussion is given here. For the absolute momentum calibration, the excited states of ^{12}C(e,e'), measured with a constant field setting for the dipole were used. Since the momentum difference from the elastic peak to each excited state is known, using the following equation one can determine Γ, the spectrometer constant and P_f, the absolute momentum:

$$P_f = \Gamma\ B\ [1 + \frac{\Delta P}{P}] \tag{5.28}$$

$$P_f = \Gamma\ B\ [1 + \sum_{i=1}^{2} d_i\ x_{fp}^i]. \tag{5.29}$$

Here B is the spectrometer dipole field. We include only up to the second order term in x_{fp} since the results are not affected by including a third order term (the coefficient d_3 is the same size as its error bar). For further details see Ref. [111].

Figure 5.9 shows the reconstructed transverse position (y_{tg}) at the target for the HRSE. The three foils of the waterfall target can be resolved due to the high resolution nature of the spectrometers.

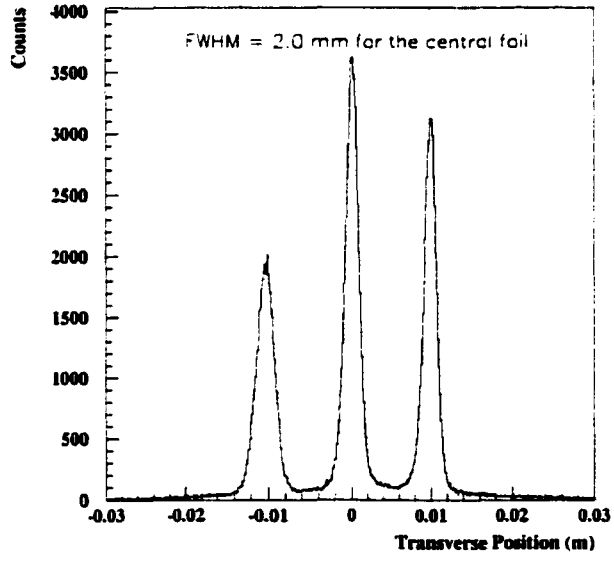

Figure 5.9: Transverse position (y_{tg}) reconstruction for the waterfall target.

The magnetic constants for the two HRS are listed in Table 5.1.

	HRSE	HRSH
Γ (MeV/kG)	253.22±0.36	270.21±0.38

Table 5.1: Magnetic constants for the two HRS.

5.4 Beam energy calculation.

Since this was one of the first physics experiments in Hall A, we did not have a reliable standard method of measuring the energy of the incident electron. Since we had elastic H(e,e'p) events from the waterfall target in our acceptance, we used the kinematically over-determined H(e,e'p) reaction to calculate the beam energy using

$$E_i = 2\,M_N\,[\frac{\sin\theta_t\ (\sin\theta_p\ -\sin\theta_t)}{(\sin\theta_p - \sin\theta_t)^2\ -\sin^2\theta_e}]. \tag{5.30}$$

Here M_N is the proton mass, θ_e and θ_p are the electron and proton scattering angles respectively, and θ_t is the sum of the two scattering angles. The derivation of this equation can be found in Appendix B.

The result of this method is shown in Figure 5.10. The width of this distribution depends on the angular resolution of the two spectrometers, energy loss due to straggling before and after scattering and on multiple scattering when the particle travels from the target to the focal plane.

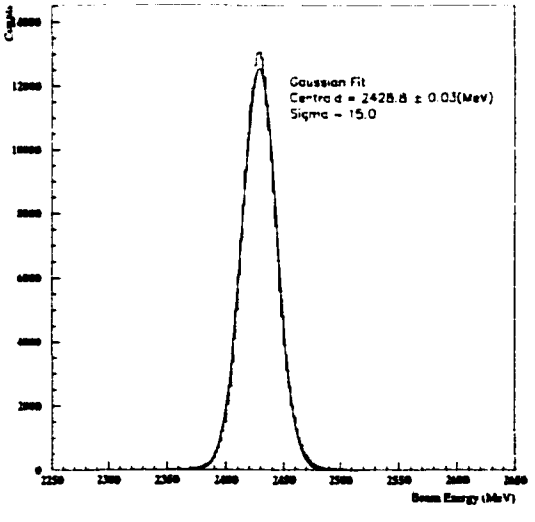

Figure 5.10: Beam energy obtained from H(e,e'p) scattering angle method for E89033.

This is only one method of determining the beam energy. A comparison of the beam energy obtained from three different methods for experiment 89003 is documented in Ref. [111]. The three different methods were: ^{12}C(e,e') differential recoil technique, the H(e,e'p) scattering angle technique, and the (e,e'p) missing energy technique. All three methods gave the same result for the beam energy within 0.2%, giving us confidence in using one method.

5.5 FPP data analysis.

In this section we present how the polarization observable amplitudes at the focal plane are determined, starting from the hit patterns obtained from the front and rear FPP straw chambers. We first determine the front track that is incident on the carbon analyzer. Then we determine the scattered track using the two rear FPP chambers. From these two proton trajectories the two scattering angles θ_{fpp} and ϕ_{fpp} were calculated. Finally fitting the ϕ_{fpp} distribution with a function, f [cos (ϕ_{fpp}), sin (ϕ_{fpp}), cos (2 ϕ_{fpp}), sin (2 ϕ_{fpp})], we obtain the polarization amplitudes at the focal plane.

5.5.1 Determination of wire number (demultiplexing).

For each hit on each FPP plane, the straw group, leading edge and trailing edge times of the TDC signal are input to the analysis code ESPACE. As mentioned in Chapter 4, all the straws in a plane are multiplexed in groups of eight. The time difference between the leading edge and the trailing edge of the TDC signal corresponds to the pulse width of the gate set by the readout board for that particular wire. There are eight such gates corresponding to each straw in the straw group. The ordering of the gates are different from plane to plane as shown in the Table 5.2.

Gate #	1	2	3	4	5	6	7	8
Straw # in Front planes	1	3	2	4	6	8	5	7
Straw # in RV1,RV2	1	3	2	4	6	8	5	7
Straw # in RU1,RU2	8	6	7	5	3	1	4	2
Straw # in RX1,RX2	1	3	2	4	6	8	5	7
Straw # in RU3,RU4,RU5	8	6	7	5	3	1	4	2
Straw # in RV3,RV4,RV5	8	6	7	5	3	1	4	2

Table 5.2: Relationship between the gate number and the straw number in a straw group.

The characteristic time width for a given straw in a group of eight may vary from the standard values. Therefore cuts corresponding to different wires are placed on time difference spectra (demux spectra) obtained from a pulser run. There are such demux spectra for each wire group in all 24 planes. These cuts are saved into a data file and were read in by ESPACE to determine the wire number in a group. One such demux spectrum is shown in Figure 5.11. Each gate has a width of 10 ns. If the time difference for a signal is greater than the highest gate, it will be assigned the highest gate, and if the time difference is less than the lowest gate, it will be assigned the first gate. Finally, the wire number is obtained using Equation 5.31.

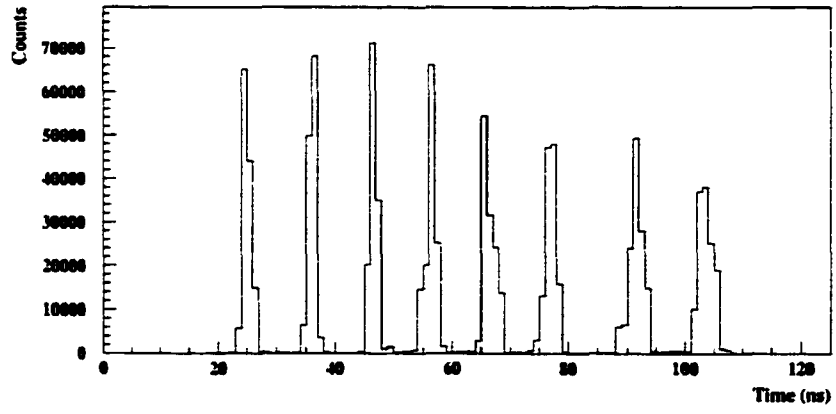

Figure 5.11: Demux spectrum from front V1 plane of FPP.

$$\text{Wirenumber} = 8 * (\text{wiregroup} - 1) + \text{IWG}. \tag{5.31}$$

Here IWG is the wire number in that wire group.

Figure 5.12 shows the raw straw chamber data taken for a Hydrogen run. The step in this figure is due to the high correlation of the H $(\vec{e}, e'\vec{p})$ data in the y direction, and the use of a target with three discrete foils.

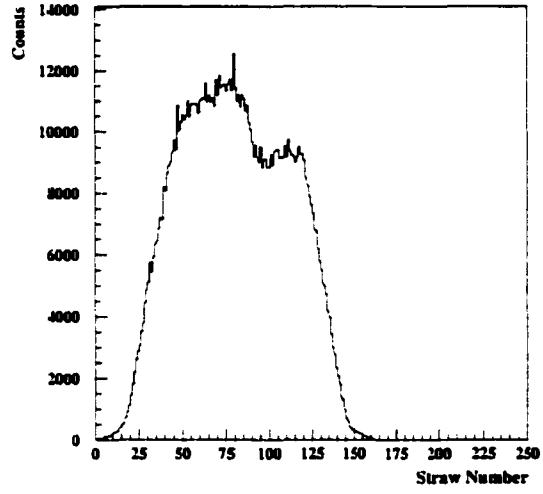

Figure 5.12: Raw straw spectrum for the front V5 plane of FPP.

5.5.2 Drift time to drift distance calculation for FPP.

To determine the exact spatial position of the proton track through the straw, we need to know the drift distance in addition to the straw number (of course there will still be a circle around the wire with the radius of this drift distance to pick from, until we compare the hits and drift distances of the other planes for a particular track).

As was described in Chapter 4, the TDC leading-edge time is proportional to the time it takes the electron bunch to travel towards the anode wire, and is in turn proportional to the drift distance. There can be an offset (t_{offset}) in time depending

on which plane and in which straw group it is from. This is due to different delays in different parts of the electronics. These offsets were obtained by shifting the leading edge time (LTDC) spectra distributions so that the shortest time corresponds to zero. Such a corrected spectrum is shown in Figure 5.13.

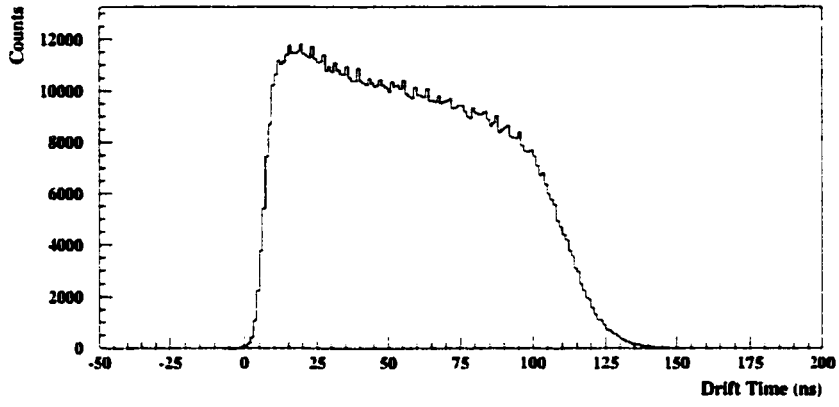

Figure 5.13: Drift time spectrum after correcting for t_{offset} for the front U1 plane of FPP.

Near the anode wire, the drift velocity changes rapidly. Thus, in this region the drift time to drift distance conversion is not linear. Instead it is obtained from a fifth-order polynomial in corrected drift time, t_c.

$$\text{Drift distance} = \sum_{n=0}^{5} \mathrm{T(j,n)}\ t_c^n. \tag{5.32}$$

The coefficients T(j,n) were obtained from fitting the integrated time spectra for a plane j. These coefficients are also stored in a data file and are read in by ESPACE. If the drift distance was larger than 0.522cm (which corresponds to the radius of the straw), it was assigned 0.522 and if it was less than zero it was assigned zero.

5.5.3 Determination of the incident and scattered tracks for the carbon analyzer.

Once the straw number and drift distance information for a given event in each plane are known, from a linear fit to these hits we can now determine the approximate front and rear trajectories. For a precise determination of the trajectory, we need to include the software alignment information.

Since we are measuring the asymmetry of the polar scattering angle distribution of the proton scattered from carbon (ϕ_{fpp}) to obtain the physics, there should not be any false or instrumental asymmetries in the detector system. False asymmetries can arise from two sources: misalignments and inefficiencies of the chambers. Therefore the proper alignment of the FPP chambers is fundamental to the extraction of the correct asymmetries. There are two kinds of alignments: internal alignment which aligns the four FPP chambers to one another, and the global alignment which aligns these four FPP chambers to the VDC's. Both of these alignments are necessary if one wishes to obtain the correct polarization observables at the target. The alignment of the FPP and the determination of the precise tracks afterwards are both discussed in Appendix A. The x and y distributions thus obtained from the FPP during ^{16}O running are shown in the Figure 5.14.

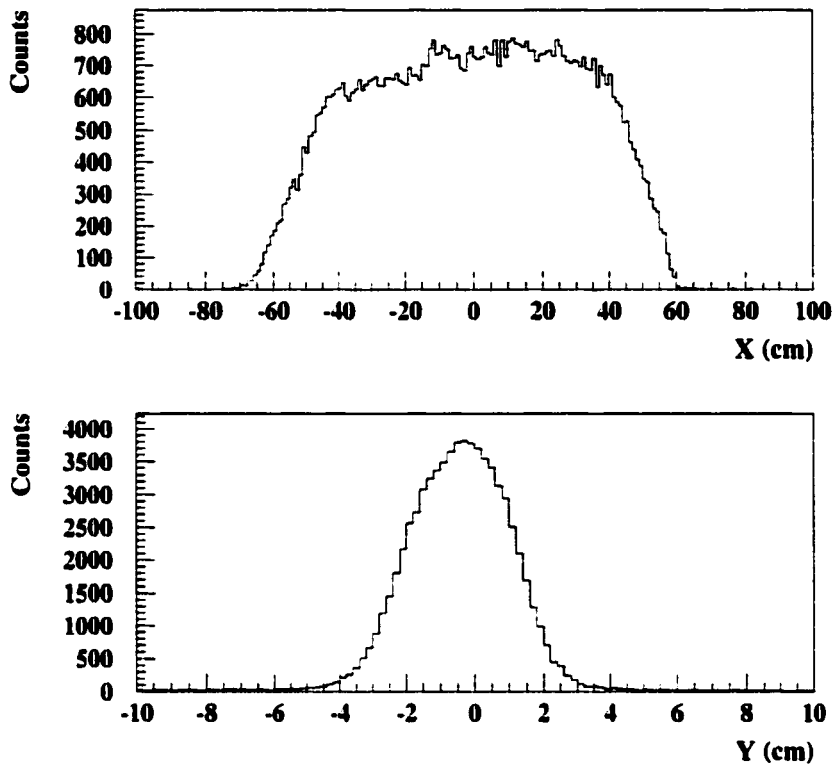

Figure 5.14: x and y positions obtained from FPP at the focal plane for the 85 MeV/c pmiss point.

5.5.4 Determination of scattering angles for the secondary scattering.

After the determination of the incident and the scattered tracks for the carbon analyzer, we can now determine the scattering angles. There are three sets of angles of interest. The first two sets are the Cartesian angles of the initial and final trajectories, $(\theta_f,\ \phi_f,\ \psi_f)$ and $(\theta_r,\ \phi_r,\ \psi_r)$. The third set is the polar and azimuthal secondary scattering angles, θ_{fpp} and ϕ_{fpp}.

Figure 5.15 shows the Cartesian angles for either the incident or the scattered track in the $\hat{x}$, $\hat{y}$, $\hat{z}$ coordinate system (this is the same transport coordinate system defined earlier). Here θ and ϕ are the Cartesian angles we already have from the

track reconstruction for either the front or the rear track, θ is the angle between the projection of the track on the yz plane and the z axis while ϕ is the angle between the projection of the track on the xz plane and the z axis.

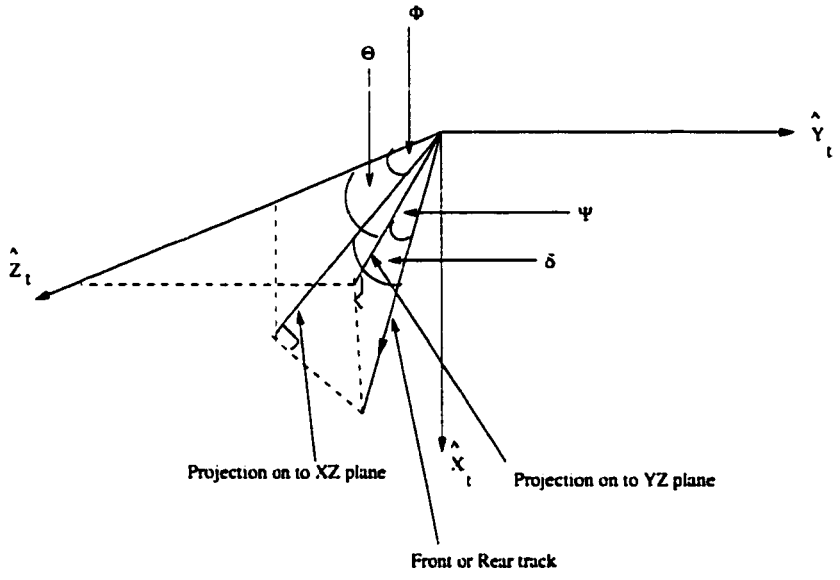

Figure 5.15: Cartesian angles shown for the front or the rear track through FPP.

If δ and ψ are the angles between the track and the xz and yz planes respectively we can write the projection of the unit track on to the x, y, z axis in terms of either (θ,ψ) or (δ,ϕ) as follows:

$$\hat{x} = \cos\delta\sin\phi = \sin\psi \quad (5.33)$$

$$\hat{y} = \sin\delta = \cos\psi\sin\theta \quad (5.34)$$

$$\hat{z} = \cos\delta\cos\phi = \cos\psi\cos\theta. \quad (5.35)$$

From 5.34 and 5.35 ,

$$\tan\delta = \cos\phi\tan\theta. \quad (5.36)$$

From 5.33 and 5.34, substituting for δ in terms of ϕ and θ,

$$\tan\psi = \tan\phi\cos\theta. \tag{5.37}$$

This is valid for both the front and the rear tracks, so we have

$$\tan\psi_f = \tan\phi_f\cos\theta_f \tag{5.38}$$

$$\tan\psi_r = \tan\phi_r\cos\theta_r. \tag{5.39}$$

Since we are interested in finding the scattered angles of the scattered track with respect to the incident front track, it will be convenient if the front track lies along the z axis of the coordinate system. But since we have a distribution of incident angles, each incident track has its own z axis. Therefore, for every track the coordinate system has to be rotated so that its z axis lies along the direction of the incident track.

This is achieved by two rotations. First we rotate the yz plane around the x axis by an angle θ, so that $\hat{z}$ is along the front track. This is performed by the matrix (R1) as shown below. Then we rotate the coordinate system by an angle ψ so that the front track is on the xz plane. This is performed by the matrix (R2) given in the following equation.

If the new projection vectors along x, y and z directions for the front and rear track are $(\hat{x}'_f, \hat{y}'_f, \hat{z}'_f)$ and $(\hat{x}'_r, \hat{y}'_r, \hat{z}'_r)$, we can relate the new projection vectors to the old ones by

$$\begin{bmatrix} \hat{x}'_f \\ \hat{y}'_f \\ \hat{z}'_f \end{bmatrix} = \begin{bmatrix} 0 \\ 0 \\ 1 \end{bmatrix} = \overbrace{\begin{bmatrix} \cos\psi_f & 0 & -\sin\psi_f \\ 0 & 1 & 0 \\ \sin\psi_f & 0 & \cos\psi_f \end{bmatrix}}^{R1} \overbrace{\begin{bmatrix} 1 & 0 & 0 \\ 0 & \cos\theta_f & -\sin\theta_f \\ 0 & \sin\theta_f & \cos\theta_f \end{bmatrix}}^{R2} \begin{bmatrix} \hat{x}_f \\ \hat{y}_f \\ \hat{z}_f \end{bmatrix}. \tag{5.40}$$

Therefore the rear track projection vectors along the x, y, z directions also change

$$\begin{bmatrix} \hat{x}'_r \\ \hat{y}'_r \\ \hat{z}'_r \end{bmatrix} = \overbrace{\begin{bmatrix} \cos\psi_f & 0 & -\sin\psi_f \\ 0 & 1 & 0 \\ \sin\psi_f & 0 & \cos\psi_f \end{bmatrix}}^{R1} \overbrace{\begin{bmatrix} 1 & 0 & 0 \\ 0 & \cos\theta_f & -\sin\theta_f \\ 0 & \sin\theta_f & \cos\theta_f \end{bmatrix}}^{R2} \begin{bmatrix} \hat{x}_r \\ \hat{y}_r \\ \hat{z}_r \end{bmatrix}. \tag{5.41}$$

This will result in

$$\begin{bmatrix} \hat{x}'_r \\ \hat{y}'_r \\ \hat{z}'_r \end{bmatrix} = \begin{bmatrix} \cos\psi_f\,\hat{x}_r - \sin\theta_f\sin\psi_f\,\hat{y}_r - \cos\theta_f\sin\psi_f\,\hat{z}_r \\ \cos\theta_f\,\hat{y}_r - \sin\theta_f\,\hat{z}_r \\ \sin\psi_f\,\hat{x}_r + \sin\theta_f\cos\psi_f\,\hat{y}_r + \cos\theta_f\cos\psi_f\,\hat{z}_r \end{bmatrix}. \tag{5.42}$$

Using the result in Eq. 5.38 for ψ_f we determine $\hat{x}'_r$, $\hat{y}'_r$, $\hat{z}'_r$.

Now both front and rear tracks are in a coordinate system defined along the front track. Thus the angles of the rear track measured in this coordinate system are directly equal to the scattering angles. Now we determine the Cartesian scattering angles θ_{sc}, ϕ_{sc}, ψ_{sc}.

$$\psi_{sc} = \sin^{-1}(\hat{x}'_r) \tag{5.43}$$

$$\theta_{sc} = \sin^{-1}\left(\frac{\hat{y}'_r}{\cos\psi_{sc}}\right) \tag{5.44}$$

$$\phi_{sc} = \tan^{-1}\left(\frac{\hat{x}'_r}{\hat{z}'_r}\right) = \tan^{-1}\left(\frac{\tan\psi_{sc}}{\cos\theta_{sc}}\right). \tag{5.45}$$

What we are really interested are the azimuthal and polar angle distributions (ϕ_{fpp}, θ_{fpp}) for the scattering by carbon. These spherical angles are shown in Figure 5.16. ϕ_{fpp} is defined to be the angle of the projected rear track on to the $\hat{x}'_r\,\hat{y}'_r$ plane measured from the $\hat{y}'_r$.

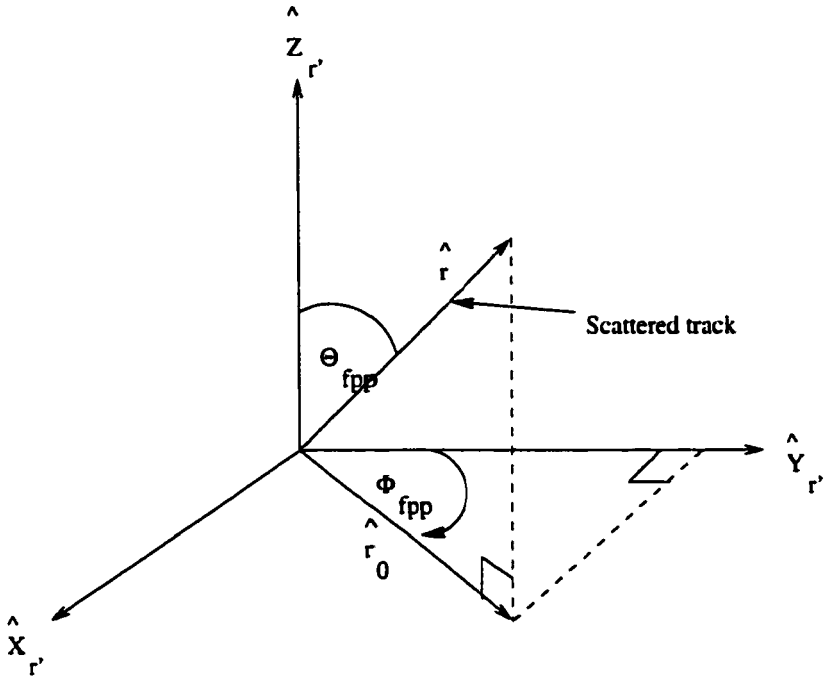

Figure 5.16: Spherical angle definition for FPP.

If $\hat{r}_0$ is the projection of $\hat{r}$ on to $\hat{x}'_r$ $\hat{y}'_r$ plane,

$$\hat{r}_0^2 = \hat{x}_r'^2 + \hat{y}_r'^2 \tag{5.46}$$

$$\theta_{fpp} = \tan^{-1}\left(\frac{\hat{r}_0}{\hat{z}'_r}\right) \tag{5.47}$$

$$\phi_{fpp} = \tan^{-1}\left(\frac{\hat{x}'_r}{\hat{y}'_r}\right). \tag{5.48}$$

These angles are calculated by the ESPACE analyzer for each scattered event.

5.6 Software cuts.

Before looking at the ϕ_{fpp} distributions to obtain the polarization observables at the focal plane, it was necessary to impose some software cuts to ensure the quality of the data. We can categorize these cuts in to five sets

1. Good electron event.
2. Good proton event.
3. Good coincidence event.
4. Good polarimetry event.
5. Separation of states.

5.6.1 Good electron event.

In order to make sure the electron detected by the electron spectrometer corresponds to a clean trajectory, the VDC data are restricted to some conditions. A track should fire at least 3 wires (high multiplicity). Only single track events are accepted (single cluster events). Further, a set of cuts were applied to remove the extreme trajectories.

5.6.2 Good proton event.

In addition to applying cuts to select good proton events as in the case of the good electron event, some cuts were applied on the FPP data to ensure that the event is a clean one for the FPP as well. For the FPP, both the front and the rear track have to be present. For this all four sets of straws; front U, front V, rear U, and rear V, should have acceptable hits, since loss of even one of these makes it impossible to calculate the scattering angles, θ_{fpp} and ϕ_{fpp}. Secondly we impose a cut on the χ^2 of the fit to the positions measured on each plane for the front tracks. Figure 5.7.2 shows the unnormalized χ^2 distribution for the linear fit of the front u coordinate. Here the peak corresponds to the good fits as opposed to the tail which corresponds to poor fits or mis-tracking. χ^2 distribution is peaking around 0.15 rather than at 1, since our weighting factor was 1 cm rather than the resolutions. This gives us the

resolutions for the position determination, which would be about 225 microns. A software cut of $\chi^2 = 0.5$ was imposed on the front tracks.

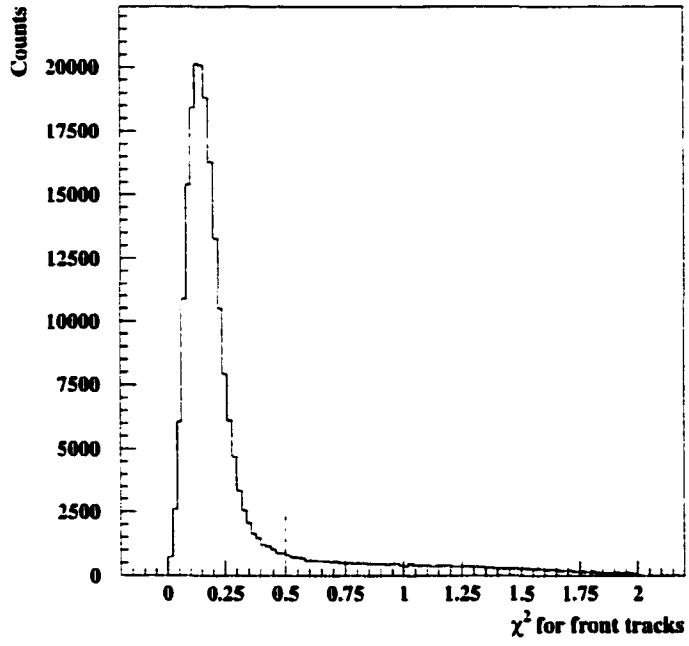

Figure 5.17: Unnormalized χ^2 distribution for the front U tracking of FPP.

5.6.3 Good coincidence events.

We have to make sure that the recorded coincidence events from the Hall A data acquisition system are true coincidence events rather than being accidentals. This was achieved by making two software cuts. The time of flight spectrum we have at Hall A for forward angles has very little background, due to the 100 % duty factor of the machine. A software cut was made on the coincidence time of flight peak from 198 ns to 208 ns. This is shown in the Figure 5.18. The finite width of this peak is due to electronic jitter in numerous cables used. To further eliminate accidentals, a y_{tg} cut was used so that the electron spectrometer and the hadron spectrometer both reconstruct the transverse position at the target to the same water foil. This is shown in Figure 5.19.

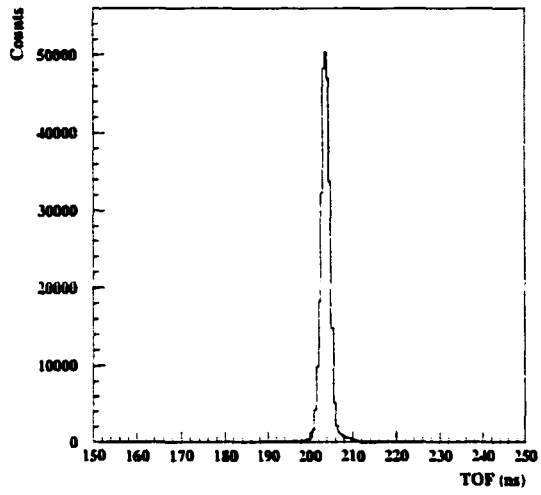

Figure 5.18: Coincidence time of flight.

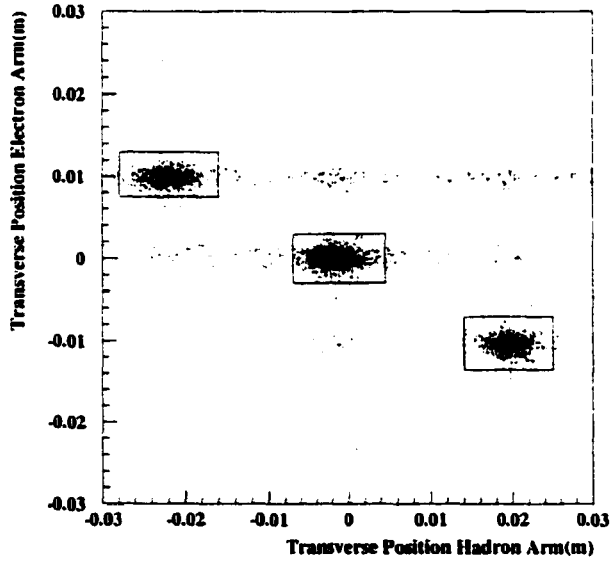

Figure 5.19: Transverse position reconstruction at the target for the three water foils from the two spectrometers.

5.6.4 Good polarimetry events.

There were some tests which were specifically on the variables obtained from the FPP. This is to further remove bad trajectories as well as ambiguous regions from the FPP data.

"Zclose" cut.

The first test removes events for which the incident and the scattered trajectories do not intersect within the physical thickness of the carbon analyzer (zclose cut). The actual thickness of carbon we used was 22.5 cm. Due to the smearing of trajectories and due to multiple scattering, the distribution is wider than this and the cut was made a little more than 2σ, which is 40 cm.

θ_{fpp} cut.

A second test is performed on the polar scattering angle θ_{fpp}. Since most of the small angle events are due to Coulomb scattered events (corresponding to the peak in Figure 5.20), these events were removed with a cut $\theta_{fpp} < 5^0$. The ^{12}C reaction analyzing power has to be known for the computation of individual polarizations. For large θ_{fpp} angles the analyzing power is not well known from the earlier models. Therefore we also use an upper limit on the θ_{fpp} distribution as well, which rejects the larger scattering angles. However, since both the analyzing power and the number of scattered events (efficiency) drop off rapidly for higher angles, the error bar actually does not improve much by the inclusion of these events.

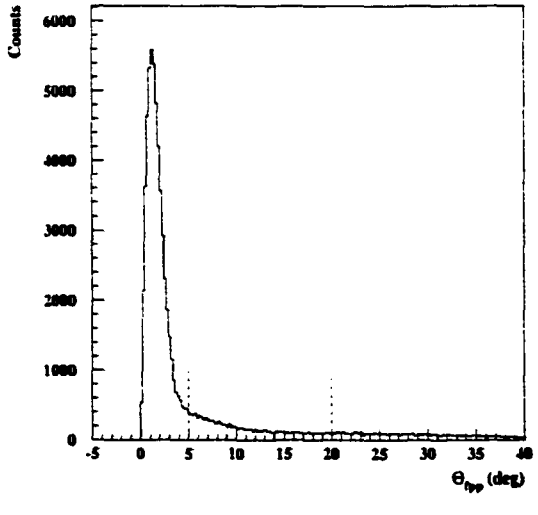

Figure 5.20: θ_{fpp} distribution for 85 MeV/c pmiss point. The dashed line shows the angular region used for the analysis.

Cone-test.

The third test was on the acceptance of the secondary scattering event. This requirement was necessary to ensure that the acceptance effects did not introduce any false asymmetries. We define a cone-test by rotating the scattered trajectory around the incident trajectory, keeping the angle θ_{fpp} constant. We check whether the four extreme corners of the ellipse ($\pm$ x and $\pm$ y) lie within the acceptance of the rear chambers. In Figure 5.21, the event A will pass the cone-test while the event B will fail the cone-test. However, due to the very large acceptance of the rear FPP chambers only 1% of the incident events fail this test for the angular range $\theta_{fpp} < 20^0$. As the figure shows, for θ_{fpp} above 40^0 all the events fail the cone-test. Therefore the cone-test is necessary if one wishes to go to higher θ_{fpp} angles. The cone-test results are shown in Figure 5.22.

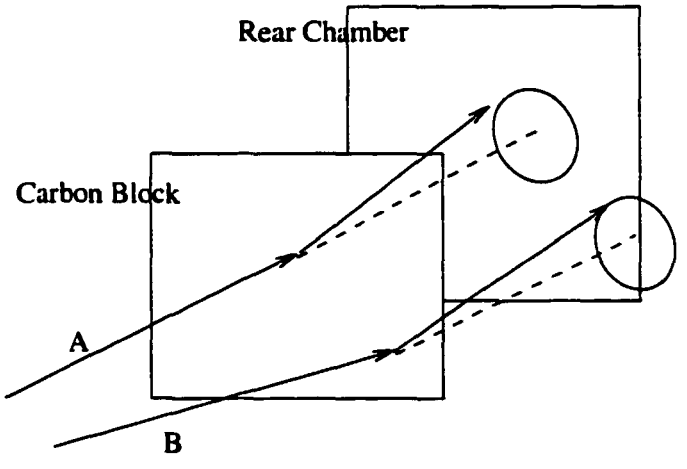

Figure 5.21: Schematic diagram to describe the cone-test. Event A will pass the cone-test while event B will fail the cone-test.

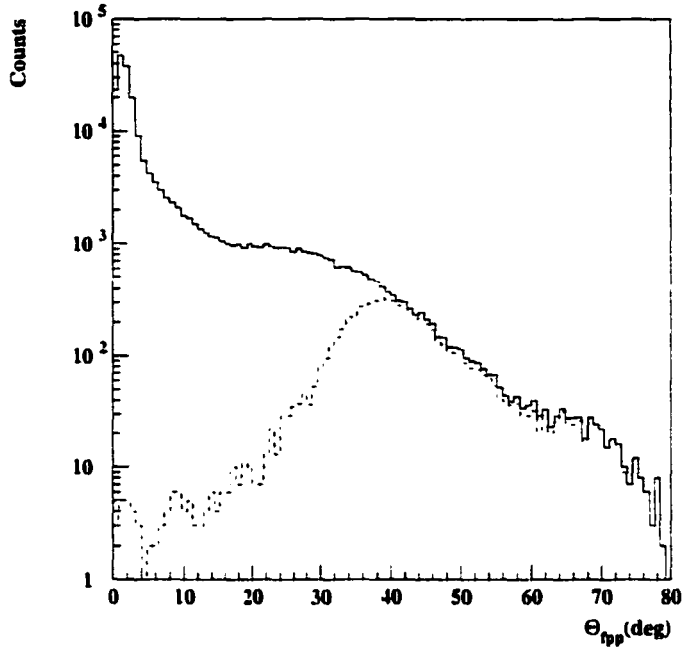

Figure 5.22: Cone-test results for 85 MeV/c pmiss point. The solid line shows the total # of events and the dashed line shows the cone-test failed events. Note that the y axis is in logarithmic scale. For $\theta_{fpp} < 20^0$, less than 1.0 % of the events fail the cone-test.

5.6.5 Separation of states.

Since this experiment was performed with a waterfall target in the quasielastic region, we had H$(e,e'p)$ in our acceptance at the 85 MeV/c pmiss point. These events had to be separated from ^{16}O (e,e'p) data. Furthermore, for ^{16}O data we had to separate the events into the individual valence states: $1p_{1/2}$, $1p_{3/2}$ and $1s_{1/2}$. For this we used a two dimensional plot of missing energy vs. missing momentum. Polygon cuts were used to separate the states as shown in Figure 5.23. On this plot the H(e,e'p) peak is present as a thick cluster of events at (Missing Energy = 0, Missing Momentum = 0) and the radiative tail from H is the band that extends at 45^0 to the missing momentum axis. The tail extending parallel to the missing momentum axis corresponds to H(e,e'p) events smeared due to the angular resolution

of the spectrometers. Since the $1s_{1/2}$ state is a broad bump in missing energy, we used a missing energy bin of 25 MeV (30 - 55 MeV) for this state.

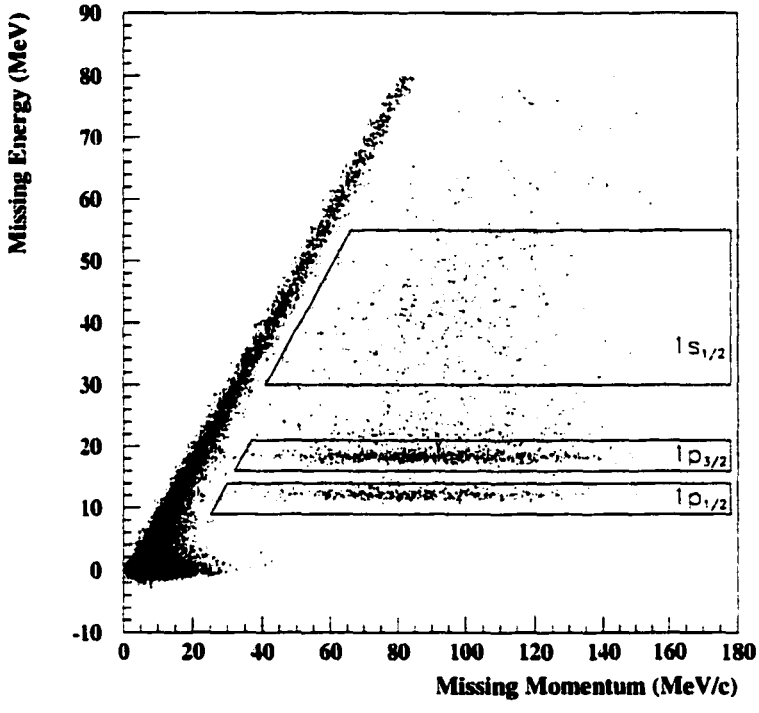

Figure 5.23: The missing energy vs. missing momentum distribution for the 85 MeV/c pmiss point. See text for details.

At several occasions over the course of the experiment, there were shifts in the missing energy spectrum of up to about 6 MeV. These shifts are due to various reasons such as shift in the beam energy, shift in the horizontal position of the beam or changes in the dipole magnetic field. Before adding the runs together, we adjusted the beam energies used to analyze each run so that the $1p_{1/2}$ peak in missing energy is aligned at 12.1 MeV as shown in Figure 5.24.

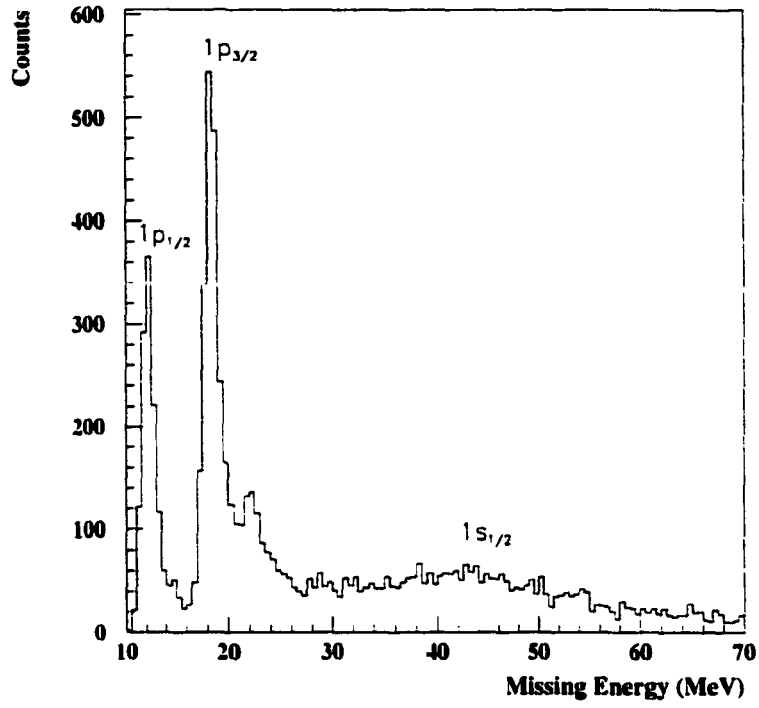

Figure 5.24: Note that the H(e,e'p) data has been removed by a software cut.

5.7 Extraction of Polarization observables.

5.7.1 Asymmetry.

To extract the final state proton polarization observables at the focal plane, we used the azimuthal angular distribution (ϕ_{fpp}) for the events that scatter off the carbon analyzer and pass the software cuts mentioned above.

The ϕ_{fpp} distribution for positive or negative helicity events, $\sigma^{\pm}$, can be written in the following form:

$$\sigma^{\pm}(\theta_{fpp},\phi_{fpp},T) = \sigma_0^{\pm}(\theta_{fpp},T)[1 + A_c(\theta_{fpp},T)\,(P_t^{fp})\sin\phi_{\rm fpp} - \mathrm{P_n^{fp}}\cos\phi_{\rm fpp}) + a_0\cos\phi_{\rm fpp} + \mathrm{b_0}\sin\phi_{\rm fpp} + \mathrm{c_0}\cos 2\phi_{\rm fpp} + \mathrm{d_0}\sin 2\phi_{\rm fpp}]. \quad (5.49)$$

Here P_t^{fp} and P_l^{fp} are the transverse and normal polarization components

measured at the focal plane (here the polarizations P_t^{fp} and P_l^{fp} at the focal plane are along $\hat{y_{fp}}$ and $\hat{x_{fp}}$ in Figure 5.7), h is the electron beam polarization, A_c is the analyzing power, $\sigma_0^+(\theta_{fpp}, T)$ and $\sigma_0^-(\theta_{fpp}, T)$ are the total number of rescattered protons for + and - helicity states respectively. Here a_0, b_0, c_0, d_0 are the instrumental or false asymmetries of the polarimeter. The negative sign for the $\cos\phi_{fpp}$ P_n^{fp} term is solely due to the definition of the angle ϕ_{fpp}.

However, we are interested in the polarization observables at the target in the reaction plane (as denoted in Chapter 2). When going through the spectrometer magnetic elements, the spin of the proton precesses. As a result, the target polarization components P_n, P_l' and P_t' are mixed together to give the focal plane polarizations P_n^{fp}, P_l^{fp} and P_t^{fp}. Note that we can measure only two components of the polarization, namely P_n^{fp} and P_t^{fp}, at the focal plane since the third component, P_l^{fp} is perpendicular to the FPP.

5.7.2 Precession angle calculation.

When the proton travels through the magnetic elements of the spectrometer, its spin precesses. In the simplest case we can assume that the spin precesses only due to a perfect dipole magnet. That is, there are no fringe field effects and the two poles of the dipole will be exactly parallel. In such a case the transverse component of the spin will be parallel to the magnetic field lines and will not precess. However, the longitudinal and the normal component of the spin will mix together to give new spin values for P_n^{fp} and P_l^{fp} at the focal plane. Such an effect can be calculated by the aid of a precession angle χ (which is a measure of how much time the proton spent traveling through the dipole), given by

$$\chi = \frac{g-2}{2}\gamma\theta_{bend} \tag{5.50}$$

$$\gamma = \frac{1}{\sqrt{1-\frac{p^2c^2}{E^2}}}. \tag{5.51}$$

Here, g is the gyro-magnetic ratio, θ_{bend} is the bend angle for the proton through the spectrometer, E and p are the energy and momentum of the proton. In the 2-Dimensional case where we assume that there is no change in the horizontal angle ϕ,

$$\theta_{\text{bend}} = (45^0 + \theta_{tg} - \theta_{fp}). \tag{5.52}$$

The angle of 45^0 has to be added since the target and focal plane coordinate systems differ by a rotation of 45^0.

In the 3-Dimensional case,

$$\theta_{\text{bend}} = cos^{-1}\,\hat{\beta}_{tg} \cdot \hat{\beta}_{fp} \tag{5.53}$$

$$\hat{\beta}_{\text{tg}} = \frac{1}{\sqrt{1 + \tan^2\theta_{\text{tg}} + \tan^2\phi_{\text{tg}}}}(\tan\theta_{\text{tg}},\, \tan\phi_{\text{tg}},\, 1) \tag{5.54}$$

$$\hat{\beta}_{\text{fp}} = \frac{1}{\sqrt{1 + \tan^2(\theta_{\text{fp}} + 45^0) + \tan^2\phi_{\text{fp}}}}(\tan(\theta_{\text{fp}} + 45^0),\, \tan\phi_{\text{fp}},\, 1). \tag{5.55}$$

2-D and 3-D precession angle χ plots for the 85 MeV/c pmiss point ^{16}O are shown in Figure 5.25.

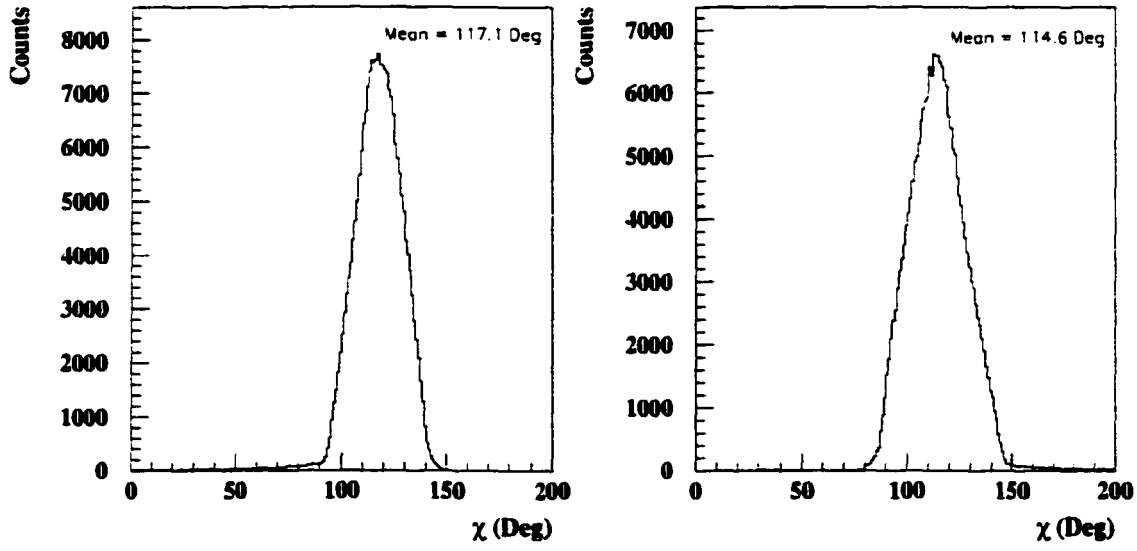

Figure 5.25: Event by event calculation of the precession angle χ for 2-D and 3-D cases for ^{16}O data. See text for details.

5.7.3 Spin transport.

To transform polarization components from target coordinate system to the focal plane coordinate system, we have to use the spin transport matrix. If we assume a simple dipole for the magnetic elements, the spin transport matrix is a simple 3 x 3 matrix as shown below.

$$\begin{bmatrix} P_n^{fp} \\ P_t^{fp} \\ P_l^{fp} \end{bmatrix}_{fp} = \begin{bmatrix} \cos\chi & 0 & \sin\chi \\ 0 & 1 & 0 \\ -\sin\chi & 0 & \cos\chi \end{bmatrix} \begin{bmatrix} P_n \\ \pm|h|\,P_t' \\ \pm|h|\,P_l' \end{bmatrix}_{tg} . \tag{5.56}$$

In reality, the high resolution hadron spectrometer consists of a dipole and three quadrupoles. Further, the dipole has edge effects or fringe field effects at the poles and all the magnetic elements have higher order poles and corrections. Therefore, the actual spin transport matrix is different from the simple dipole matrix and it changes from one trajectory to another, since it is a function of the target coordinates (θ, y, ϕ, $\delta)_{tg}$ of the trajectory.

The HRSH at Hall A was modeled using the differential analysis code COSY [115], [116] and a RAYTRACE code SNAKE [117]. For this analysis COSY was used to obtain the spin transport matrix elements for each event. For more details refer to Ref. [118].

COSY input.

COSY is an arbitrary order differential analysis code which allows us to determine both the transport coordinates as well as the spin transport matrix elements for a given set of magnetic elements. Table 5.3 and Table 5.4 give the characteristics and drift distances of the magnetic elements of HRSH used for the COSY input respectively.

Magnetic element	Radius (m)	Length (m)
Q1	0.075	0.9413
Q2	0.150	1.8266
Dipole	8.4	6.597
Q3	0.150	1.8268

Table 5.3: Characteristics of the magnetic elements of HRSH used for COSY input.

Magnetic elements	Drift distance (m)
target-Q1	1.6
Q1-Q2	1.1661
Q2-Dipole	4.4271
Dipole-Q3	1.5983
Q3-Focal plane	3.4505

Table 5.4: Drift distances of the magnetic elements of HRSH used for COSY.

The symplectic map from COSY is a Taylor expansion of the spin matrix which relates the spin at the target to the spin at the focal plane as a function of the target coordinates y_{tg}, θ_{tg}, ϕ_{tg}, and δ.

We can denote the real spin transport matrix as

$$\begin{bmatrix} P_n^{fp} \\ P_t^{fp} \\ P_l^{fp} \end{bmatrix}_{fp} = \begin{bmatrix} S_{nn} & S_{nt} & S_{nl} \\ S_{tn} & S_{tt} & S_{tl} \\ S_{ln} & S_{lt} & S_{ll} \end{bmatrix} \begin{bmatrix} P_n \\ \pm |h| P_t' \\ \pm |h| P_l' \end{bmatrix}_{tg} \tag{5.57}$$

$$\mathrm{P_n^{fp}} = \mathrm{S_{nn}\,P_n} \pm \mathrm{S_{nt}\,|h|\,P_t'} \pm \mathrm{S_{nl}\,|h|\,P_l'} \tag{5.58}$$

$$\mathrm{P_t^{fp}} = \mathrm{S_{tn}\,P_n} \pm \mathrm{S_{tt}\,|h|\,P_t'} \pm \mathrm{S_{tl}\,|h|\,P_l'}. \tag{5.59}$$

Accumulated spin transport matrix elements for ^{16}O data from the pmiss = 85 MeV/c kinematic setting with a comparison to the pure dipole case, are shown in Appendix C. Substituting equations 5.58 in equation 5.49 we obtain,

$$\begin{aligned} \sigma^{\pm}(\theta_{fpp}, \phi_{fpp}, \mathrm{T}) = {} & \sigma_0^{\pm}(\theta_{fpp}, T)[1 + A_c(\theta_{fpp}, T)\,(S_{tn}\,P_n \pm S_{tt}\,|h|\,P_t' \pm S_{tl}\,|h|\,P_l')\sin\phi_{\mathrm{fpp}} \\ & - A_c(S_{nn}\,P_n \pm S_{nt}\,|h|\,P_t' \pm S_{nl}\,|h|\,P_l')\cos\phi_{\mathrm{fpp}} \\ & + a_0\cos\phi_{\mathrm{fpp}} + \mathrm{b_0}\sin\phi_{\mathrm{fpp}} + \mathrm{c_0}\cos 2\phi_{\mathrm{fpp}} + \mathrm{d_0}\sin 2\phi_{\mathrm{fpp}}]. \end{aligned} \tag{5.60}$$

5.7.4 Difference distribution.

Now taking the difference of the two normalized distributions for the two helicity states and dividing by 2, the measured physics asymmetries at the target corresponding to P_l' and P_t' (canceling all the instrumental asymmetries) are obtained,

$$\begin{aligned} \mathrm{f}(\theta_{\mathrm{fpp}}, \phi_{\mathrm{fpp}}) = \frac{\sigma^+}{2\,\sigma_0^+} - \frac{\sigma^-}{2\,\sigma_0^-} = {} & (S_{tt}\,|h|\,A_c\,P_t' + S_{tl}\,|h|\,A_c\,P_l')\sin\phi_{\mathrm{fpp}} \\ & - (S_{nt}\,|h|\,A_c\,P_t' + S_{nl}\,|h|\,A_c\,P_l')\cos\phi_{\mathrm{fpp}}. \end{aligned} \tag{5.61}$$

Such difference distributions for Hydrogen, and the ^{16}O $1p_{1/2}$, $1p_{3/2}$, and $1s_{1/2}$ states are shown in Figures 5.26 and 5.27. The phase shift of these difference

distribution is a measure of the form factor ratio for the proton. All four plots exhibit a nice $\sin\phi_{fpp}$, $\cos\phi_{fpp}$ distribution as expected. We fit these distributions with the function shown below and obtained the two coefficients of interest $a(\theta_{fpp})$ and $b(\theta_{fpp})$.

$$f(\theta_{fpp}, \phi_{fpp}) = a(\theta_{fpp})\cos\phi_{fpp} + b(\theta_{fpp})\sin\phi_{fpp} + c(\theta_{fpp})\cos 2\phi_{fpp} + d(\theta_{fpp})\sin 2\phi_{fpp}. \tag{5.62}$$

A Fourier Transformation of equations 5.61 and 5.62 gives,

$$a(\theta_{fpp}) = \frac{1}{\pi}\int_0^{2\pi} -(S_{nt}\,|h|\,A_c\,P_t' + S_{nl}\,|h|\,A_c\,P_l')\cos^2\phi_{fpp}\,d\phi_{fpp} \tag{5.63}$$

$$b(\theta_{fpp}) = \frac{1}{\pi}\int_0^{2\pi} (S_{tt}\,|h|\,A_c\,P_t' + S_{tl}\,|h|\,A_c\,P_l')\sin^2\phi_{fpp}\,d\phi_{fpp}. \tag{5.64}$$

Replacing the integral with a finite sum,

$$a(\theta_{fpp}) = -\frac{2}{N}\left[\sum_{i=1}^{N}(S_{nt}^i\,(|h|\,A_c\,P_t') + S_{nl}^i\,(|h|\,A_c\,P_l'))\right]\cos^2\phi_{fpp}^i \tag{5.65}$$

$$b(\theta_{fpp}) = \frac{2}{N}\left[\sum_{i=1}^{N} -(S_{tt}^i\,(|h|\,A_c\,P_t') + S_{tl}^i\,(|h|\,A_c\,P_l'))\right]\sin^2\phi_{fpp}^i. \tag{5.66}$$

where N is the total number of unpolarized events. For each event, the spin transport matrix elements and the polar scattering angle ϕ_{fpp}^i will be different. Since we have two equations and two unknowns this allows us to determine the two quantities of interest (hA_cP_t') and (hA_cP_l'). Using the beam polarization (h) and the average analyzing power (A_c), we determined the polarization observables at the target, P_l' and P_t'.

Note that A_c, a, and b are functions of the polar scattering angle θ_{fpp}. We performed this analysis for four small θ_{fpp} bins and then took a weighted average of P_l' and P_t' over these angular bins to obtain the final polarization components.

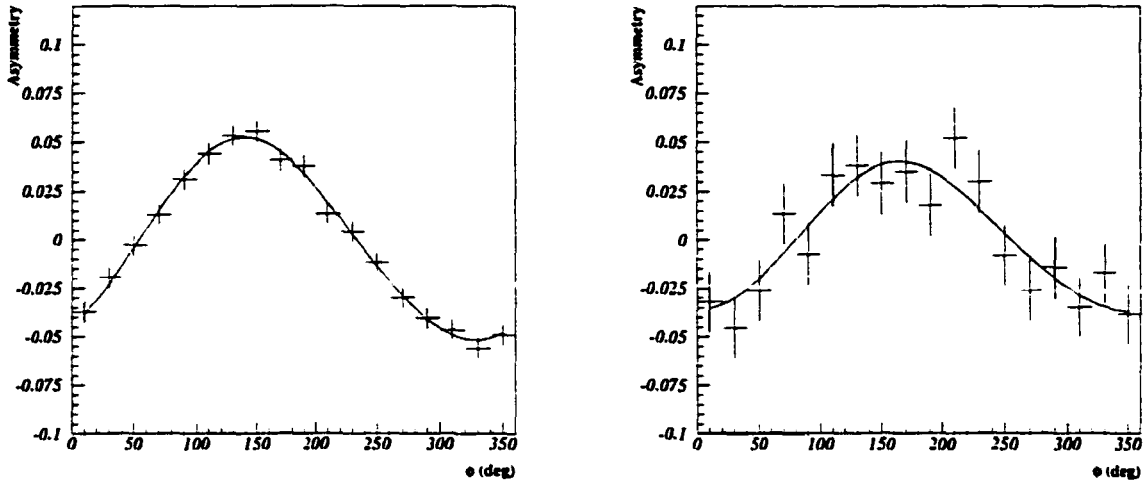

Figure 5.26: Difference distributions of ϕ_{fpp} for Hydrogen (left) and the $1p_{1/2}$ state of ^{16}O (right) with the fits superimposed.

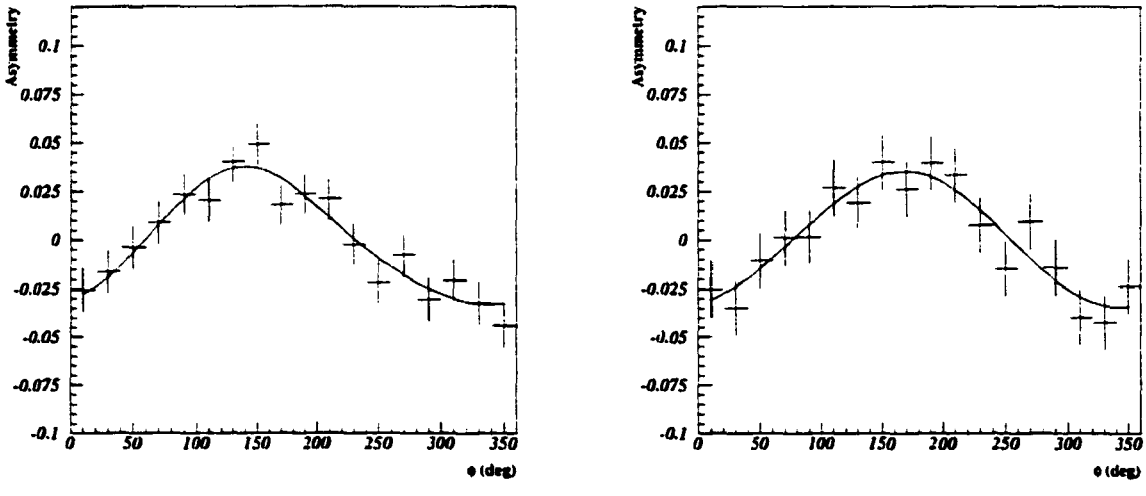

Figure 5.27: Difference distributions of ϕ_{fpp} for the $1p_{3/2}$ (left) and $1s_{1/2}$ (right) states of ^{16}O with the fits superimposed.

Though we do not use a simple dipole approximation to determine the spin precession through the spectrometer, simple dipole method was used as a cross check to see by how much the values change due to the actual spin precession. We found out that the differences between these two methods for the case where there is a symmetric distribution of events through the quadrupoles and the dipole, such as the

^{16}O data and the H data at the parallel kinematic point, were less than 2% for all the data sets. However in the case of Hydrogen data at the 85 MeV/c pmiss point (see Figure 5.28) , where the events are at one corner of the phase space, there is quite a big difference between the simple dipole analysis and the real spin precession analysis. about 9%. Nevertheless, for $\mu G_E/G_M$, the Hydrogen results at the parallel kinematic point and at the 85 MeV/c pmiss point both are in very good agreement with each other to less than a percent level when the full correction is performed. This gives us confidence in our analysis, especially the spin precession method. The θ_{tg} vs. ϕ_{tg} plots for the hadron arm for these two cases are shown in Figure 5.28.

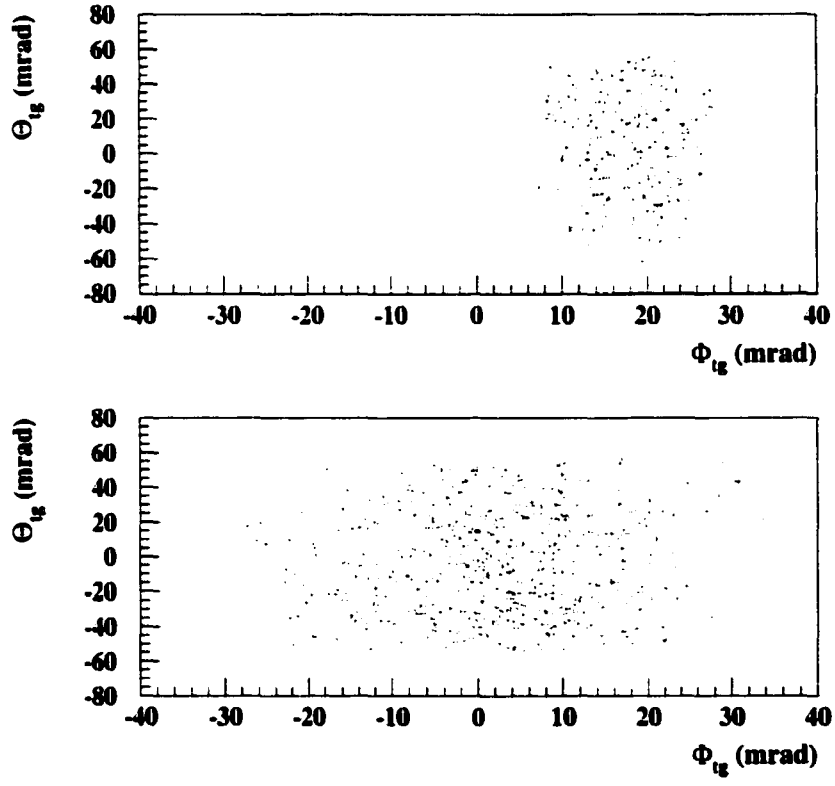

Figure 5.28: θ_{tg} (out-of-plane) vs. ϕ_{tg} (in-plane) distributions for the hadron arm at the target for the two extreme cases of H data. As the figure shows the parallel kinematic setting has a symmetric event distribution in both θ_{tg} and ϕ_{tg}, while the H events in 85 MeV/c point are at a corner of the acceptance.

5.8 Determination of instrumental (false) asymmetries.

Instrumental asymmetries can arise due to several reasons. They are mainly due to the variations in the efficiency of the chamber system and to the residual misalignments. Although in section 5.58 we talk about only four coefficients for the false asymmetries, this can be an infinite series of θ_{fpp} dependent coefficients. However, since the Fourier series is orthogonal, the higher order coefficients do not affect the fit to the physically significant terms.

We obtained some measure of the false asymmetries by measuring the final state proton polarizations for the case of unpolarized electrons elastically scattering off of H. Since there can be no normal component of polarization at the target for Hydrogen, the total asymmetry measured corresponds to the instrumental asymmetry. For heavier targets, an induced P_n can occur from FSI. The H measurements were performed using polarized electrons. By summing the two helicity states, we effectively formed an unpolarized beam. Further, since we normalize the two helicity distributions before summing them, we do not produce an additional asymmetry due to the possible small differences in the number of events for the two states. As shown by the following equation, the sum distribution should be flat in the absence of any instrumental asymmetries. Any non-zero elements correspond to instrumental asymmetries. The sum distribution for H data is given by

$$\frac{\sigma^+}{2\sigma_0^+} + \frac{\sigma^-}{2\sigma_0^-} = 1 + a_0 \cos\phi_{\mathrm{fpp}} + b_0 \sin\phi_{\mathrm{fpp}} + c_0 \cos 2\phi_{\mathrm{fpp}} + \sin 2\phi_{\mathrm{fpp}}. \qquad (5.67)$$

The sum distribution for H with the fit superimposed is shown in Figure 5.29.

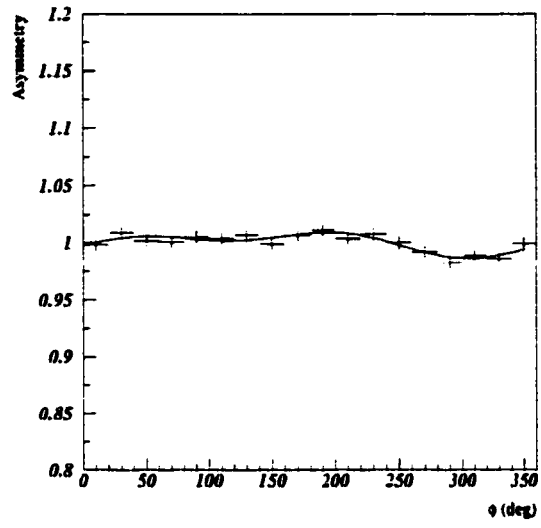

Figure 5.29: Sum distributions for Hydrogen showing the instrumental asymmetries with the fits superimposed for the parallel kinematic setting.

A listing of the instrumental asymmetry terms obtained for the whole focal plane are shown in Table 5.5. They are all less than 0.006, which is close to the design goal of the FPP.

Term	Value	Error
$\cos\phi_{fpp}$	-0.0056	0.0018
$\sin\phi_{fpp}$	0.0058	0.0018
$\cos 2\phi_{fpp}$	0.0027	0.0018
$\sin 2\phi_{fpp}$	0.0054	0.0018

Table 5.5: Values obtained for the instrumental asymmetries for the whole focal plane.

For the determination of P_l' and P_t', false asymmetries do not matter since they cancel out in the difference distribution to the first order. In any case, this was

checked for the H data by fitting the difference distribution with the function

$$f(\theta_{fpp}, \phi_{fpp}) = (K + a\,cos\phi_{fpp} + b\,sin\phi_{fpp}) \times (1 + a_0\,cos\phi_{fpp} + b_0\,sin\phi_{fpp} + c_0\,cos2\phi_{fpp} + d_0\,sin2\phi_{fpp}). \quad (5.68)$$

Here the instrumental asymmetry terms were explicitly incorporated as a_0, b_0, c_0, d_0. The difference between the two analyses for both a and b coefficients were less than 1% while the statistical error bar was about 4%.

5.9 Determination of analyzing power.

Since the measured asymmetries were a product of the polarization and the average analyzing power (A_c), to determine individual polarizations we need to know the analyzing power for the $\vec{p}$–^{12}C reaction. This is the probability that a proton scatters off of a ^{12}C nucleus with a spin dependent asymmetry.

Though the experiment E93027 [124] will eventually parameterize A_c for the ^{12}C reaction from the Hall A FPP data, it was shown that for the angular range θ_{fpp} from 5° to 20° data the measured A_c agrees with the Los Alamos parameterization (McNaughton *et al.* [15]). Though there exist a wide range of other parameterizations for A_c in the $\vec{p}$–^{12}C reaction, only two of these could be used in the proton kinetic energy range employed for this experiment. These were the McNaughton parameterization and the Aprile-Giboni *et al.* [16] parameterizations. Though these two parameterizations have very different functional forms they both produce A_c values that are in good agreement with each other for our data.

5.9.1 McNaughton parameterization.

Using the low energy range from McNaughton (kinetic energy < 450 MeV),

$$A_c(\theta_{fpp}, E_{Carbon}) = \frac{ar}{1 + br^2 + cr^4}, \quad (5.69)$$

where

$$r = p \sin\theta_{fpp}. \tag{5.70}$$

Here p is the momentum of the proton in GeV/c, and a, b, c, d are energy dependent fourth order polynomials of the form

$$a = \sum_{n=0}^{4} a_n p'^n \tag{5.71}$$

$$p' = p - 0.7\text{GeV/c}. \tag{5.72}$$

These coefficients are given in Table 5.6. The systematic uncertainty given for this method is 2%.

5.9.2 Aprile-Giboni parameterization.

The second functional form of A_c we investigated was from Aprile-Giboni*et al.* Here we used the high energy fit (150 to 571 MeV).

$$A_c(\theta_{fpp}, T) = D(\theta_{fpp}, T)\,\alpha(T)\left[\frac{\sin\theta_{fpp}}{1+\beta(T)\sin^2\theta_{fpp}+\gamma(T)\sin^4\theta_{fpp}} + \delta(T)\sin\theta_{fpp}\right] \tag{5.73}$$

$$D(\theta_{fpp}, T) = \frac{1}{1+C\exp[\theta^2_{fpp}/2\theta^2_s(T)]} \tag{5.74}$$

$$\theta^2_s(T) = C_0 + C_1\,(15/p\beta)^2. \tag{5.75}$$

Here $\theta^2_s(T)$ is to account for the angular resolution of the detector system used to obtain these fit parameters. Here $D(\theta_{fpp}, T)$ is an empirical damping factor which has an effect on the small angle scattering, and $\alpha, \beta, \gamma, \delta$ are energy-dependent third order polynomials of the form,

$$\alpha(T) = \sum_{i=0}^{4} \alpha_n X^n \tag{5.76}$$

$$X = \frac{(T-400)}{200}. \tag{5.77}$$

Here, T is the kinetic energy of the proton, given in MeV. The systematic error due to this method is 1.4 %.

McNaughton		Aprile-Giboni	
a_0	5.3346	α_0	3.3561
a_1	-5.5361	α_1	-0.91758
a_2	2.8353	α_2	0.38654
a_3	61.915	α_3	0.30807
a_4	-145.54	β_0	-7.9741
b_0	-12.774	β_1	5.3176
b_1	-68.339	β_2	12.532
b_2	1333.5	β_3	-3.1091
b_3	-3713.5	γ_0	857.93
b_4	3738.3	γ_1	810.41
c_0	1095.3	γ_2	-127.21
c_1	949.50	γ_3	-163.39
c_2	-28012.0	δ_0	0.079421
c_3	96833.0	δ_1	0.12568
c_4	-118830.0	δ_2	-0.082377
		C	58.361
		C_0	0.12
		C_1	0.38511
χ^2/d.o.f.	1.54	χ^2/d.o.f.	1.14

Table 5.6: Coefficients used for the McNaughton and Aprile-Giboni parameterizations.

Since this method is reliable only for small carbon thicknesses (3cm to 12cm) and we had a 22.5 cm thick carbon-block, rather than using the kinetic energy of the

proton at the center of the carbon we used the exact kinetic energy for each particle. Knowing the energy loss through carbon and the interaction point, we calculated the proton kinetic energy at the interaction point of the track with carbon for each particle. We found out that the energy loss through carbon is approximately linear, and it was 5.2 MeV/cm^{-1} for an incident proton energy of 412 MeV.

Figure 5.30 shows a plot of average analyzing power vs θ_{fpp} for H in parallel kinematic data using the McNaughton parameterization.

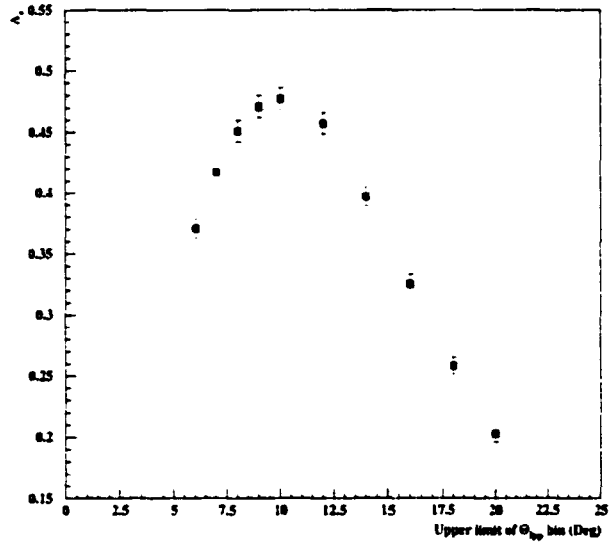

Figure 5.30: Analyzing power vs θ_{fpp} using McNaughton parameterization, taking a weighted average over the energy bins.

We used the analyzing power calculated using McNaughton parameterization to obtain the beam polarization from the H data, taken in both parallel kinematics as well as in 85 MeV/c pmiss point. The results of the overall analyzing power obtained, taking a weighted average over the angular bins, for each of these kinematic points are shown in Table 5.7. For the ^{16}O data we computed A_c using these methods for each kinematic point, each individual state and for different bins of θ_{fpp}. These results are shown in Table 5.8.

Kinematic point	A_c
H in parallel	0.383±0.008
H in 85 MeV/c piss	0.416±0.008

Table 5.7: Average analyzing power for H data.

Kinematic point	A_c
85 MeV/c pmiss	
$1p_{1/2}$ state	0.391±0.008
$1p_{3/2}$ state	0.385±0.008
$1s_{1/2}$ state	0.387±0.008
140 MeV/c pmiss	
$1p_{1/2}$ state	0.407±0.008
$1p_{3/2}$ state	0.407±0.008
$1s_{1/2}$ state	0.409±0.008

Table 5.8: Average analyzing power for ^{16}O data.

5.10 Determination of beam polarization.

As mentioned in Chapter 4, for this experiment the beam polarization was measured using a Mott polarimeter located at the injector at the 5 MeV point. Since this was the first physics experiment to use polarized beam at Jefferson Lab, the Mott polarimeter was also in its first stage of operation. Furthermore, since the beam had to steer through different magnetic elements of the beam line, this polarization can be different from the beam polarization at the target. Therefore we needed to have a cross check on these Mott numbers. Since we had Hydrogen data at the focal plane for one of the settings we could easily do this using the FPP.

5.10.1 Mott analysis.

There were several Mott measurements taken on different days throughout each kinematic setting. These Mott results are shown in the Appendix D. An average polarization for each kinematic point was determined by taking the mean value with respect to time. The statistical error for the beam polarization for each kinematic setting was obtained by taking the rms variance for each of the measurements with respect to the mean value. Figure 5.31 shows the individual polarization measurements made for each kinematic point and Table 5.9 shows the average Mott measurements for each kinematic point.

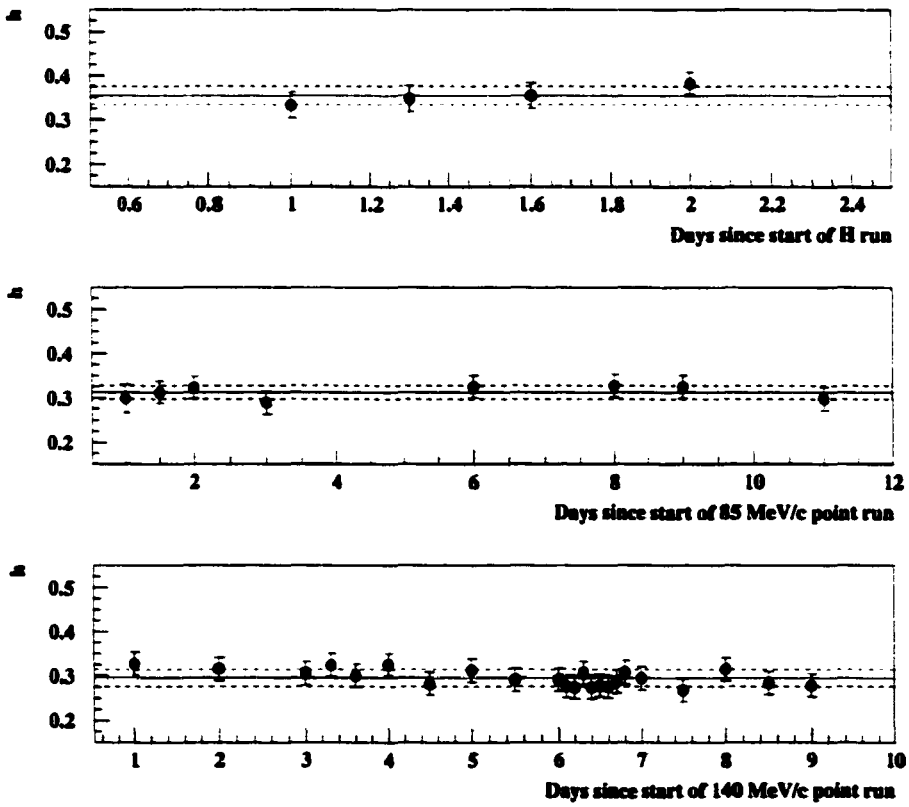

Figure 5.31: Beam polarization measurements obtained from the Mott polarimeter.

Kinematic point	h
Parallel	0.356±0.023
85 MeV/c pmiss	0.314±0.022
140 MeV/c pmiss	0.296±0.019

Table 5.9: Average beam polarizations (h) for each kinematic setting obtained by the Mott polarimeter.

5.10.2 FPP analysis.

According to Arnold, Carlson and Gross [30], from a free proton target, one can deduce the analyzing power times the beam polarization. Since the two polarization transfer observables are related to the ratio of the form factors times μ, and we already know this ratio, $\mu\, G_E/G_M$,

$$P'_t = -2\sqrt{\tau(1+\tau)}\tan(\theta_e/2)\frac{G_E/G_M}{(G_E/G_M)^2+\tau(1+2(1+\tau)\tan^2(\theta_e/2))} \tag{5.78}$$

$$P'_l = \frac{(E_i+E_f)}{M_N}\frac{\sqrt{\tau(1+\tau)}\tan^2(\theta_e/2)}{(G_E/G_M)^2+\tau(1+2(1+\tau)\tan^2(\theta_e/2))} \tag{5.79}$$

$$\frac{G_E}{G_M} = -\frac{(hA_c(\theta_e)P'_t)}{(hA_c(\theta_e)P'_l)}\frac{(E_i+E_f)}{2M_N}\tan(\theta_e/2) \tag{5.80}$$

$$\tau = Q^2/4M_N^2. \tag{5.81}$$

Here the quantities $(hA_c(\theta_{fpp})P'_t)$ and $(hA_c(\theta_{fpp})P'_l)$ are known from the analysis described in section 5.7. By knowing A_c and either P'_l or P'_t one can deduce the beam polarization, h from the quantities $(hA_c(\theta_{fpp})P'_t)$ and $(hA_c(\theta_{fpp})P'_l)$.

Since we already know A_c from the parameterization, we can obtain the beam polarization h. Figure 5.32 shows the comparison of the beam polarization for the 85 MeV/c recoil momentum point using the Mott values and the FPP values for different run times. The overall average beam polarization obtained from the Mott was

0.314±0.022 while the FPP gave a value of 0.319±0.013 which is in good agreement with the Mott results.

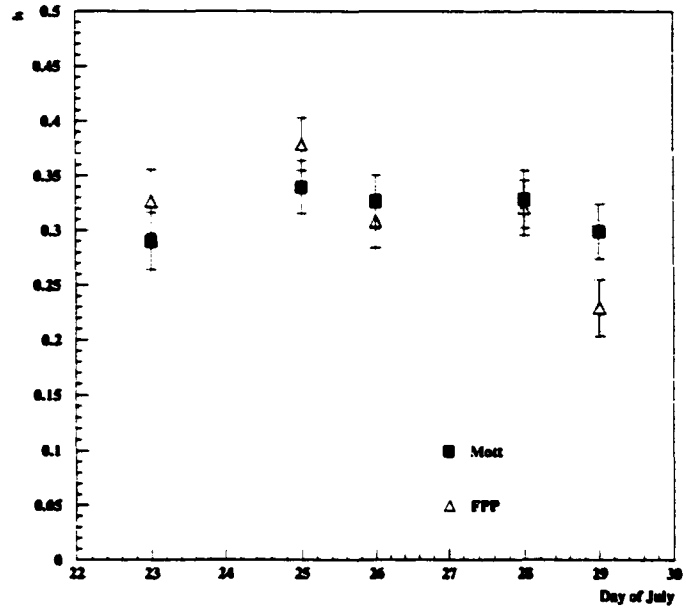

Figure 5.32: Comparison of beam polarization using FPP data and Mott data. The horizontal axis represents the time of different measurements taken during the 85 MeV/c pmiss point.

Chapter 6

Results and Discussion.

In this chapter we present the polarization transfer observable results from the experiment E89033. First we present the results for the two Hydrogen data sets and compare them to theoretical predictions. Second, we discuss the techniques we have used to correct for the phase-space averaging effects due to the finite acceptance of the hadron spectrometer. Next we will discuss how we obtained the theoretical predictions for the polarization observables at the target using these methods, so that we can truly compare the theory to the experimentally obtained data. Finally we will present the ^{16}O polarization transfer results compared to the theoretical predictions available. We conclude with a discussion of the future developments that can take place in this area of nuclear physics from the point of view of an experimentalist.

6.1 H($\vec{e}$,$e'\vec{p}$) data.

As mentioned in the earlier chapters, the use of the waterfall target had the additional advantage of providing H($\vec{e}$,$e'\vec{p}$) data simultaneously with the ^{16}O($\vec{e}$,$e'\vec{p}$) data. By measuring the polarization of the recoiling proton corresponding to H($\vec{e}$,$e'\vec{p}$), we can determine the electric to magnetic form factor ratio times the μ, $\mu G_E/G_M$ for the free proton. From Chapter 5, the $\mu G_E/G_M$ ratio is related to the polarization

observables by

$$\frac{G_E}{G_M} = -\left[\frac{(h\,A_c(\theta_{fpp})\,P_t')}{(h\,A_c(\theta_{fpp})\,P_l')}\right]\frac{E_i + E_f}{2\,M_N}\tan\left(\frac{\theta_e}{2}\right) \tag{6.1}$$

$$\frac{G_E}{G_M} = -r(\theta_{fpp})\,K. \tag{6.2}$$

Here θ_e is the event-averaged electron scattering angle, and E_i and E_f are the energies of the incident and scattered electrons respectively. For each θ_{fpp} bin, $r(\theta_{fpp})$ and the kinematic factor K were obtained from the relevant data set. Finally taking a weighted average over the angular bins, $\mu\ G_E/G_M$ was obtained. Here θ_e can be written as

$$\theta_e = \cos^{-1}\left[\frac{\cos\theta_0 + \phi_{tg}\sin\theta_0}{\sqrt{1 + \theta_{tg}^2 + \phi_{tg}^2}}\right]. \tag{6.3}$$

Here θ_0 is the spectrometer central angle for the electron arm, ϕ_{tg} and θ_{tg} are the in-plane and the out-of-plane angles measured with respect to the spectrometer central ray for each event.

The H($\vec{e}$,$e'\vec{p}$) data were present in the experimental acceptance for the parallel kinematic setting as well as in the pmiss = 85 MeV/c kinematic setting. Table 6.1 summarizes the results for $\mu G_E/G_M$ calculated for the H data in these two kinematic settings.

Observable	H in pmiss=0 MeV/c	H in pmiss=85 MeV/c
$\mu\ G_E^p/G_M^p$	0.905±0.065	0.897±0.065
P_l	0.302±0.013	0.298±0.017
P_t	-0.199±0.006	-0.194±0.005

Table 6.1: H results for the two kinematic settings.

Figure 6.1 shows the value of $\mu\ G_E/G_M$ for the free proton extracted for several bins of relative momentum, $\delta = \frac{dp}{p}$. As the figure shows, the $\mu G_E/G_M$ ratio is very

stable across the dispersive direction. This indicates that our systematics are under control, in both tracking as well as in spin precession.

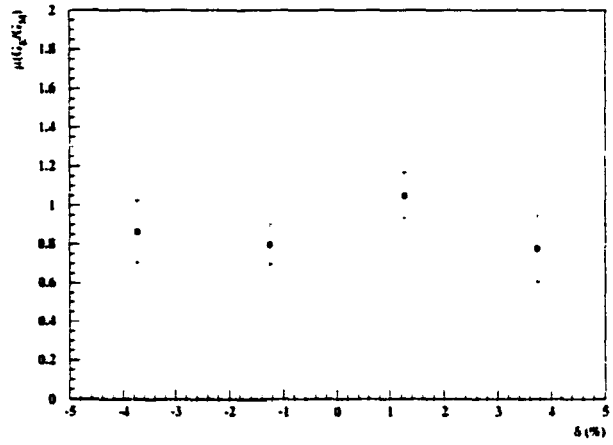

Figure 6.1: $\mu G_E/G_M$ vs. relative momentum δ for H data.

The average $\mu\ G_E/G_M$ for both data sets was 0.901 $\pm$ 0.046. Figure 6.2 shows this average value compared to the currently available theoretical calculations plotted as a function of Q^2. Here "GK" corresponds to an extended vector dominance model by M.F. Gari and W. Krümpelmann [119]; "GK1" corresponds to the standard form of [120] with a helicity-flip scale corresponding to the quark-gloun scale and "GK3" corresponds to a helicity-flip scale corresponding to a meson scale and the strange quark contributions are taken into account via the ϕ-meson. "MMD" corresponds to a vector meson dominance model by P. Mergell, U.G. Meissner and D. Drechsler [121], [122]. Here the distinction between "MMD1", "MMD2"and "MMD3" is the use of the existing proton and neutron form factor data for the fits: "MMD2" uses some extra low Q^2 proton data and some more neutron data than that of "MMD1". "MMD3" is a fit which also includes the data from the time-like ($Q^2 < 0$) region. "Höhler" corresponds to a vector dominance model by G. Höhler *et al.* [43]. "CBM" corresponds to the D.H. Lu *et al.* [123] calculations using a Cloudy Bag Model (CBM). As mentioned in Chapter 2, the experimental point agrees well with the MMD model.

In a following high precision experiment using a liquid H target to measure the form factor ratio for the free proton using the recoil polarimetry technique, E93027 [124] measured a value of 0.93±0.02 [125] at the same Q^2 point of 0.8 $(GeV/c)^2$, agreeing very well with the free value we measured.

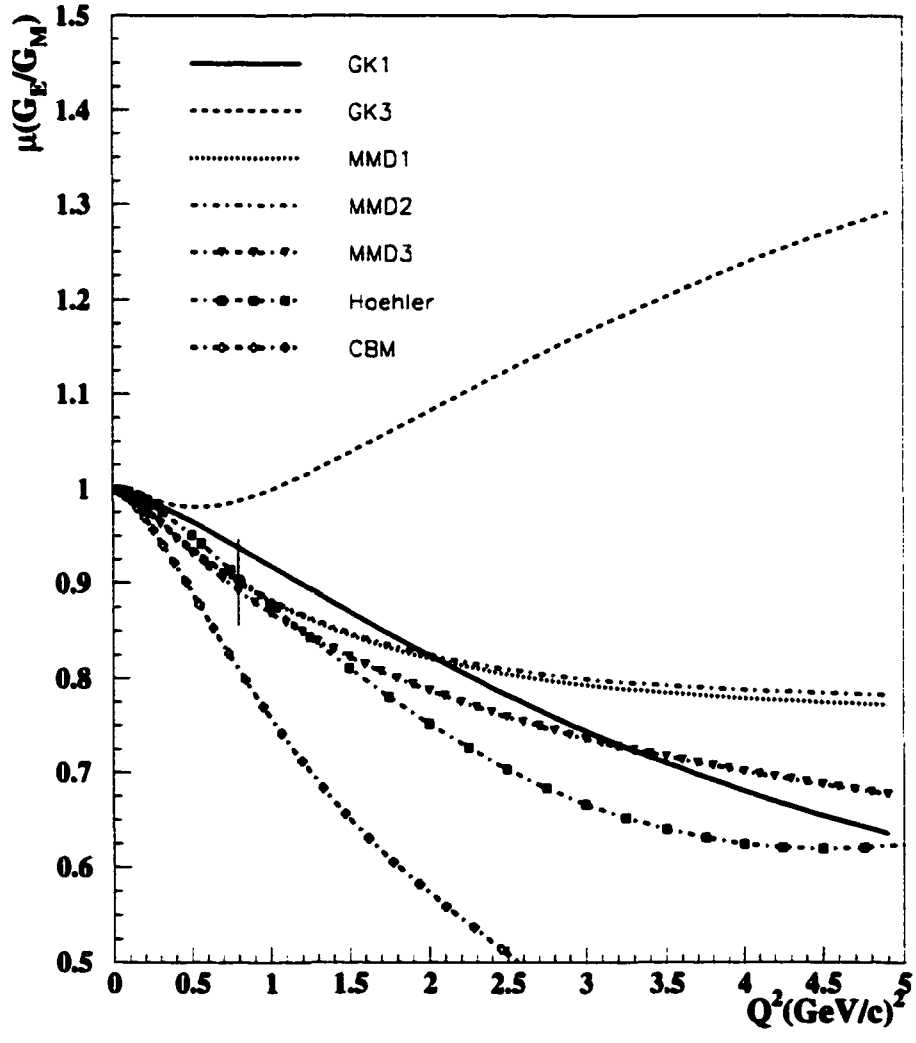

Figure 6.2: $\mu\, G_E/G_M$ vs. Q^2 for the free proton compared with available theoretical predictions.

6.2 ^{16}O $(\vec{e},e'\vec{p})$ results.

6.2.1 Comparison of theory to experiment.

In crossing the bridge between experimentally observed quantities and the theoretical predictions for polarization observables at the interaction point, there are three main aspects one has to take in to account:

1. Experimentally we measure the polarization observables over a finite acceptance that is determined by the acceptances of the electron and hadron spectrometers used, as opposed to a point acceptance as used by the theorists.

2. Due to the finite acceptance one has to worry about the mixing of other helicity dependent observables.

3. One has to correct for the fact that the knocked out proton has to travel through the nuclear medium until it comes out of the effective interaction region of the rest of the nucleus before being detected. Furthermore, before the interaction with the knocked out proton, the corresponding electron has to travel through a medium having Coulombic interactions where it loses energy and momentum.

The first effect, accounted for by acceptance averaging of the theory is described below. The second and third effects are accounted for in the theoretical calculations as described in Chapter 3.

6.2.2 MCEEP.

The theoretical calculations are evaluated for point acceptances while in experiments we have a finite acceptance. Thus in order to compare the theory to the experimentally obtained observables, we need to take into account the variations of these theoretically obtained observables over the experimental acceptance in variables such as ω, q, θ_{pq}, ϕ, Q^2 and pmiss.

Since it is not sufficient to merely compare the theory evaluated at the central kinematics with experimental observables measured and averaged over a finite acceptance, we used the Monte-Carlo code MCEEP to fold in the theoretical models over the known experimental acceptance. MCEEP was written by P. E. Ulmer [126]. Given the response functions, for a particular theoretical model, MCEEP uses them in a grid over a selected set of variables. In our case we chose the variables to be ω, q, pmiss and ϕ. MCEEP will interpolate the theory between these grid points to obtain the response functions for any event in the acceptance, using a linear interpolation algorithm. Taking in to account the theoretical cross sections and the acceptance effects MCEEP then weights the polarization observables across the acceptance to give the final acceptance-averaged theoretical predictions at the target.

MCEEP can be used for calculation of elastic scattering (e,e'), scattering to a bound state of a residual nucleus (e,e'p), or scattering to the continuum. In the case of bound states MCEEP performs a five dimensional integral where the ejectile momentum is calculated using five kinematic choices (for example, electron and proton momenta, in-plane and out-of-plane angles for the electron and for the proton). MCEEP can also be used for the analysis of uncertainties. MCEEP outputs cross sections, yields (convolution of cross section and acceptance) and polarization observables.

The first step in using MCEEP for acceptance averaging was to compare the yields generated by the simulation to the experimental yields to verify that the simulation is capable of reproducing the experimental acceptance. Figure 6.3 shows the experimental yield compared to yields from MCEEP folded in with a DWIA calculation by J.J. Kelly. There is reasonable agreement between the simulation and experiment. Since the experimental acceptance is uniform only up to $\pm 3\%$ in δ and after that the acceptance drops off rapidly (the E89003 experimental results for the relative efficiency for the HRSH spectrometer using the same waterfall target is given in Ref. [127]), while in the MCEEP we assume a uniform acceptance for $\delta \pm 4\%$ the

distributions are not exactly the same as the simulated ones.

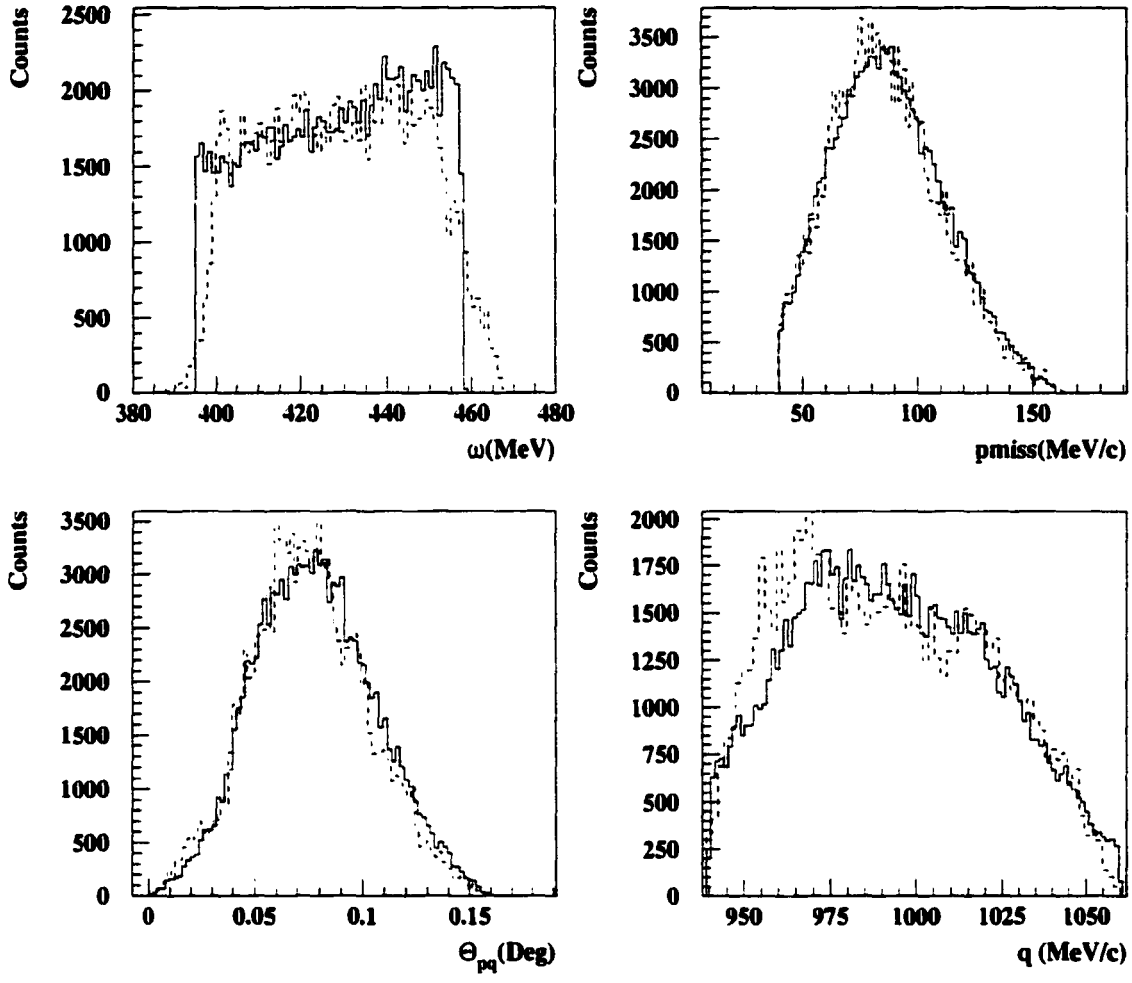

Figure 6.3: Comparison of kinematic quantities of real data with Monte-Carlo simulations obtained using a DWIA calculation. The solid curve represents the Monte-Carlo results while the dashed curve gives the experimental data.

MCEEP Input.

The main Input Deck to MCEEP requires the following input:

1. Target type specifications with the missing mass for the bound state.

2. Kinematics of the reaction (energies and angles).

3. Momentum and angular acceptances for the two spectrometers.

4. Target information: the waterfall target geometry was incorporated in MCEEP with the correct foil thicknesses.

5. A theoretical model for the nuclear polarized and unpolarized response functions.

6. Desired software cuts: We used a global cut for the missing momentum range we are interested in (40 - 160 MeV/c).

Non-relativistic DWIA calculations generated by Kelly's code LEA were folded into MCEEP for acceptance averaging. We did not use any spectrometer optics in MCEEP since we were comparing theory to experiment at the target.

Coordinate systems for polarization observables used by MCEEP.

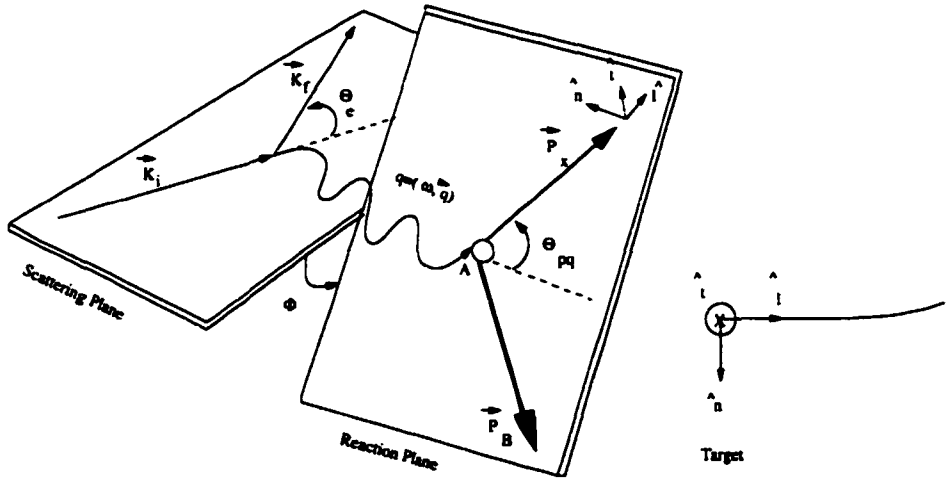

Figure 6.4: The two frames of reference used in which the polarization observables are determined in MCEEP, the reaction frame (left) and the spectrometer frame (right). Note here ϕ_{pq}=180^0 is for $\theta_p > \theta_q$ and for such a trajectory the only difference between the two frames is the sign change in the transverse component.

The input response functions to MCEEP are independent of the azimuthal angle ϕ and therefore independent of the frame of reference, in contrast to the polarization observables. In MCEEP, there are two coordinate systems in which one could extract the final state proton polarizations: The reaction frame which changes with each particle and the spectrometer frame which is a space fixed frame. We used the spectrometer frame since the experimentally observed observables were calculated in this frame.

The components of polarization are defined as shown in Figure 6.4. In the reaction frame, the longitudinal component is along the momentum direction of the hadron, $\hat{n}$ is normal to the reaction plane containing the $\vec{q}$ and the proton momentum, and the transverse component is in the reaction plane but normal to the longitudinal component such that $\hat{n}$, $\hat{l}$ and $\hat{t}$ define a right-handed system. By convention $\hat{n}$ points downward for coplanar kinematics with $\phi = 180^0$. Thus we have

$$\hat{\mathrm{l}} = \frac{\vec{p}}{|\vec{p}|} \tag{6.4}$$

$$\hat{\mathrm{n}} = \frac{\vec{q} \times \vec{p}}{|\vec{q} \times \vec{p}|} \tag{6.5}$$

$$\hat{\mathrm{t}} = \vec{n} \times \vec{l}. \tag{6.6}$$

Note that this frame changes from event to event.

In the space-fixed spectrometer frame, $\hat{l}$ is along the central ray of the transport system, $\hat{n}$ is vertically down at the target (along the dispersive direction, x) and $\hat{t}$ is given by $\hat{l} \times \hat{n}$. Therefore for a proton coming along the central ray of the spectrometer with $\phi = 180^0$, the only difference between the two frames is the sign change in the transverse component (P_t'). The spectrometer frame exactly matches the coordinate system used to evaluate the experimental results.

6.2.3 LEA.

As one of our theoretical calculations, we used the code LEA (see Chapter 3) to obtain the polarization observables and response functions.

Coordinate system used for LEA.

Since the experimentally determined quantities are in the spectrometer frame in MCEEP, we had to give the point acceptance theory from LEA also in the same coordinate system. Since for a proton coming along the central ray the two frames, reaction and the spectrometer, are the same, we employed the reaction frame (the coordinate system referred to as the helicity frame in LEA) to obtain the point acceptance theory in the spectrometer frame. The helicity frame is the frame normally used by theorists to calculate the final state polarizations. Furthermore missing momentum is positive for $\theta_p > \theta_q$ (or $\theta_{pq}>0$) in LEA. This is the same in the experiment. In the present experiment P_l', P_t' were measured only for positive pmiss values.

Form factors used for the free proton.

In LEA we assumed free values for the form factors for the proton inside the ^{16}O nucleus, calculated the P_l' and P_t' and compared to data. Differences between these calculations and the data would indicate possible modifications of the form factor ratio in the nuclear medium. The H$(\vec{e}, e'\vec{p})$ data from this experiment indicated that all 3 MMD model [121], [122] predictions agree well with the free form factors. Results from a more recent detailed H$(\vec{e}, e'\vec{p})$ experiment, to be published, support this choice [124] as well. Thus, this model was used in LEA to obtain the proton form factor values.

For a three dimensional grid in the space of independent variables ω, q and pmiss the unpolarized and polarized response functions were obtained from LEA to perform the phase-space averaging. In MCEEP, each event generated within the acceptance was binned using the same 3-D grid used by LEA. Then for each event, the polarization observables were calculated using the response functions given by LEA for that grid bin and the azimuthal angle, ϕ, for the event. As explained later, ϕ played an important role in the acceptance averaging for the pmiss=85 MeV/c kinematic point. The experimental ranges for the four variables, ω, q, pmiss and ϕ

used to obtain the response functions from LEA are given in Table 6.2.

Kinematic point	q(MeV/c)	ω(MeV)	pmiss(MeV/c)	ϕ
85 $p_{1/2}$	940 - 1060	395 - 465	40 - 160	70^0 - 290^0
85 $p_{3/2}$	940 - 1060	400 - 475	40 - 160	70^0 - 290^0
85 $s_{1/2}$	940 - 1060	410 - 480	50 - 170	70^0 - 290^0
140 $p_{1/2}$	940 - 1060	395 - 465	70 - 210	120^0 - 250^0
140 $p_{3/2}$	940 - 1060	400 - 475	80 - 210	120^0 - 250^0
140 $s_{1/2}$	940 - 1070	410 - 500	100 - 230	120^0 - 250^0

Table 6.2: Ranges for the four independent variables used to do the phase space averaging.

Comparison of acceptance-averaged theoretical results from LEA to experimental results are shown in Table 6.3 below. There is fair agreement between the experimental results and the acceptance-averaged theory for most of the settings.

Kinematic point	P_l'(Exp)	P_l'(Theory)	P_t'(Exp)	P_t'(Theory)
85 $1p_{1/2}$	0.304±0.074	0.305	-0.219±0.065	-0.176
85 $1p_{3/2}$	0.217±0.057	0.285	-0.105±0.051	-0.183
85 $1s_{1/2}$	0.416±0.056	0.307	-0.159±0.049	-0.150
140 $1p_{1/2}$	0.325±0.050	0.310	-0.085±0.047	-0.140
140 $1p_{3/2}$	0.259±0.035	0.278	-0.159±0.030	-0.144
140 $1s_{1/2}$	0.289±0.044	0.295	-0.065±0.039	-0.092

Table 6.3: Comparison of acceptance averaged theory to experimental data.

Plotting of results.

It is more illuminating to compare the experimentally measured P_l' and P_t' values at the two pmiss settings with the acceptance-averaged theory as a function of

pmiss. However, due to computational difficulties it is not possible to plot acceptance-averaged theory values of P_l' and P_t' as a function of pmiss. Thus the experimental values had to be compared to the theory evaluated for a point acceptance.

The point acceptance theoretical values were obtained by using the central values for q, ω, pmiss and ϕ. To transform the experimentally obtained values of polarization observables to point acceptance values, a factor R defined below was utilized. The R factors for each of the kinematic points are shown in Table 6.4.

$$\mathrm{R} = \frac{\text{Point theory}}{\text{Acceptance averaged theory}}. \tag{6.7}$$

$$\text{Experiment point acceptance} = R\ (\text{Experiment full acceptance}). \tag{6.8}$$

Kinematic point	R(P_l')	R(P_t')
85 $1p_{1/2}$	1.034	0.976
85 $1p_{3/2}$	0.966	0.986
85 $1s_{1/2}$	1.023	0.914
140 $1p_{1/2}$	1.028	0.960
140 $1p_{3/2}$	1.004	0.985
140 $1s_{1/2}$	1.041	0.993

Table 6.4: Factors used to transform experimentally obtained points to point acceptance experiment values.

Results for ^{16}O .

The measured values of P_l' and P_t' in the spectrometer frame, transformed to point acceptance values using Eq. 6.7, compared to the DWIA calculations are shown in Figure 6.5. All three theoretical curves assume free proton values for the proton form factors inside the ^{16}O nucleus. All three calculations seem to agree well with each other in the range of the missing momentum covered by this experiment, suggesting that model dependence of the polarization observables in the relevant range is not

large. Furthermore, the agreement of the experimental data points with the theory (with the only exception of the 85 MeV/c missing momentum point of P_t' in $1s_{1/2}$ state which is about two σ away from the theory) suggests that the medium modifications of the form factors for the proton inside ^{16}O nucleus are small.

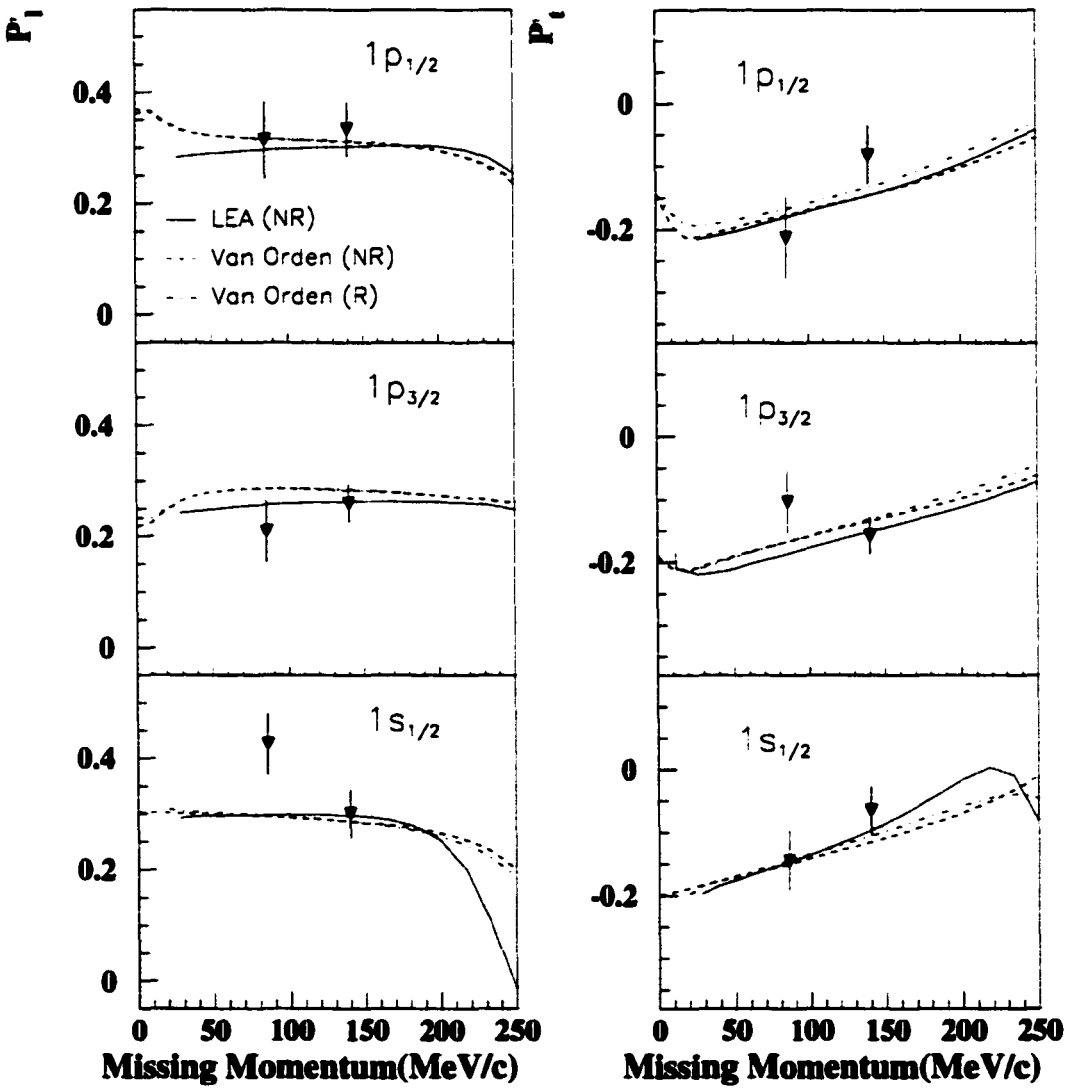

Figure 6.5: P_l' and P_t' experimental results compared to three DWIA calculations for the three valence states of ^{16}O. The non-relativistic DWIA Kelly calculations were obtained by using LEA. Also shown are non-relativistic and relativistic DWIA calculations by Van Orden. These calculations are discussed in detail in Chapter 3.

Discussion of acceptance averaging.

As the Table 6.4 indicates, the acceptance averaging effects in the spectrometer frame used here are small for both kinematic settings. The Figure 6.6 shows the polarization observables as a function of ϕ in the spectrometer frame.

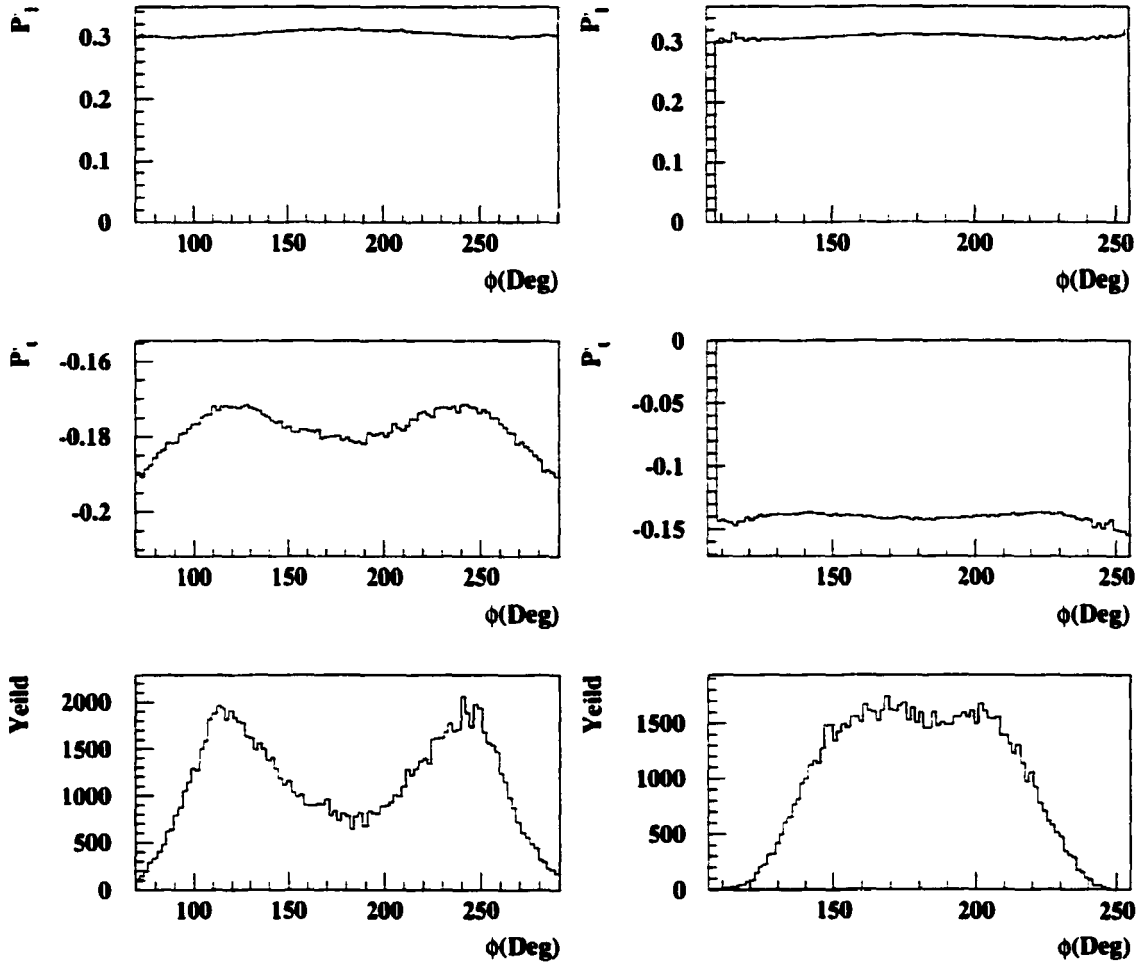

Figure 6.6: Variation of polarization observables with ϕ in the spectrometer frame and the corresponding yields. The left side corresponds to the pmiss = 85 MeV/c setting, while the right side corresponds to the pmiss = 140 MeV/c setting. The variations with ϕ are less pronounced than in the reaction frame shown in Figure 6.9.

The variation of the polarization observables P_l' and P_t' in the phase space of the hadron spectrometer in the spectrometer frame is shown in Figure 6.7. As the

figure indicates, the maximum variation is from 0.19 to 0.16 for P_t' (14%) and 0.31 to 0.30 for P_l' (3%), making the phase space averaging meaningful.

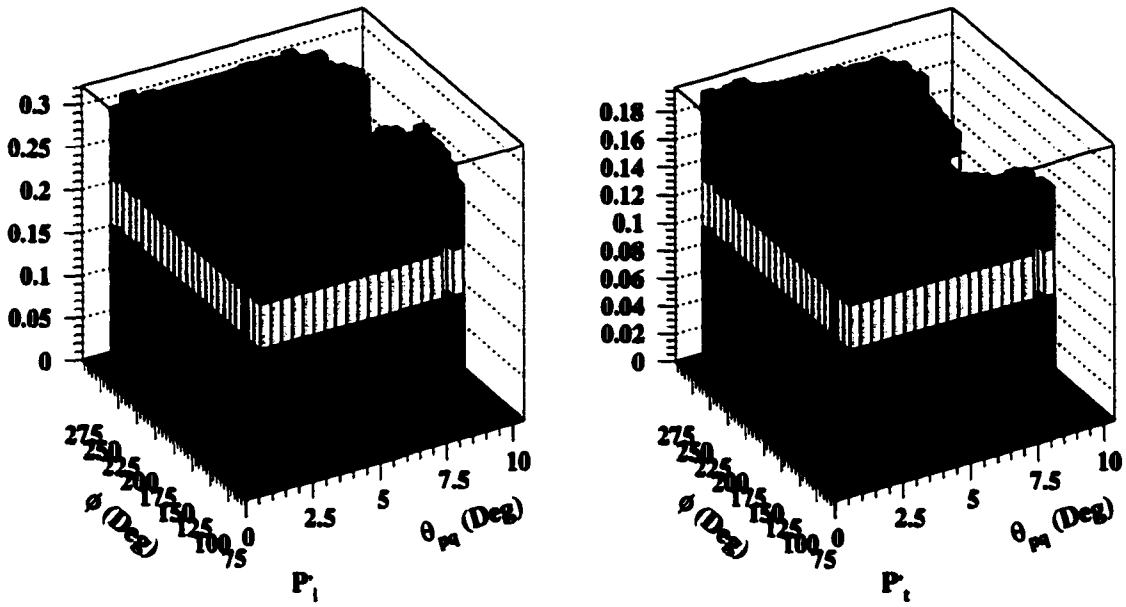

Figure 6.7: Variation of polarization transfer observables P_l' and P_t' across the acceptance of the hadron spectrometer for the pmiss = 85 MeV/c setting. Here θ_{pq} is the horizontal variation while ϕ gives the out-of-plane range.

If we had tried to do the acceptance averaging in the reaction frame, we could have had innumerable difficulties. In the reaction frame the acceptance averaged values differ greatly from the central, point acceptance values for the 85 MeV/c kinematic point, while for the pmiss=140 MeV/c setting the acceptance averaged and point values agree. This is due to the fact that for the 140 MeV/c setting with $\theta_{pq} \sim 8^0$, ϕ is restricted to a small range centered around 180^0 while for the 85 MeV/c setting with $\theta_{pq} \sim 2.5^0$ (q vector in the acceptance), ϕ can take a larger range. For the point acceptance case both these settings have $\phi = 180^0$. The polarization observables depend strongly on ϕ. Thus the large range of ϕ for the 85 MeV/c setting results in the acceptance averaged polarizations being very different from the point acceptance values in the reaction frame.

The relationship between the polarization transfer observables and the out-of-plane angle is given by

$$P'_l = \frac{1}{I_0}[V'_{LT}\, R'^{L}_{LT} \cos\phi + V'_{TT}\, R'^{L}_{TT}] \tag{6.9}$$

$$P'_t = \frac{1}{I_0}[V'_{LT}\, R'^{T}_{LT} \cos\phi + V'_{TT}\, R'^{T}_{TT}]. \tag{6.10}$$

(6.11)

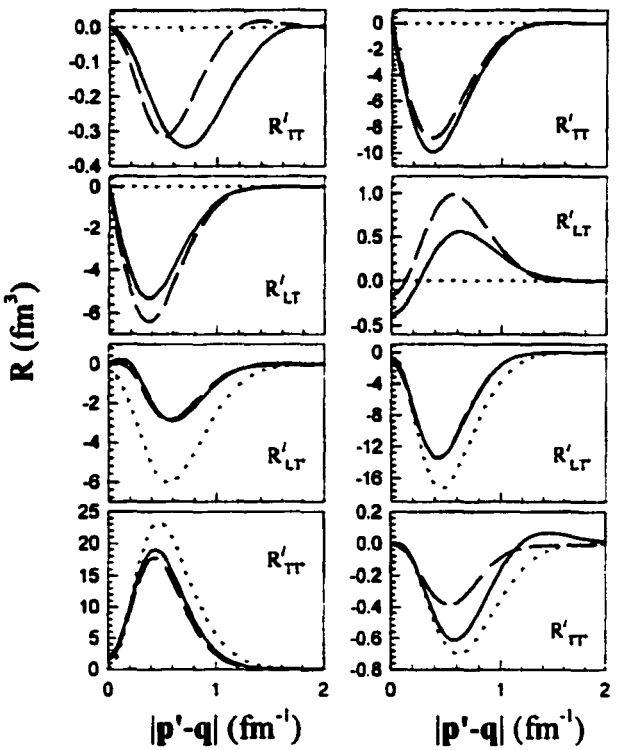

Figure 6.8: Polarization response functions. $R^l_{LT'}$ and $R^l_{TT'}$ ($R^t_{LT'}$ and $R^t_{TT'}$) are the left (right) side, plots 3 and 4 respectively. These are DWIA calculations obtained from Ref. [27], for approximately our kinematics.

As the equations above indicate, the ϕ dependence of P'_l (P'_t) is associated with the $R^l_{LT'}$ ($R^t_{LT'}$) term, while the contribution of $R^l_{TT'}$ ($R^t_{TT'}$) term is independent of ϕ. As illustrated by Figure 6.8, $R^t_{LT'} \gg R^t_{TT'}$. Thus P'_t is heavily dependent on ϕ and the above-described acceptance averaging difference is significant for P'_t. On the

other hand, $R^l_{LT'} < R^l_{TT'}$. Thus P'_l is only mildly dependent on ϕ and the acceptance averaged and central values of P'_l do not differ much. Figure 6.9 shows the yield and the polarization observables as a function of possible ϕ values for 85 and 140 MeV/c points in the reaction frame.

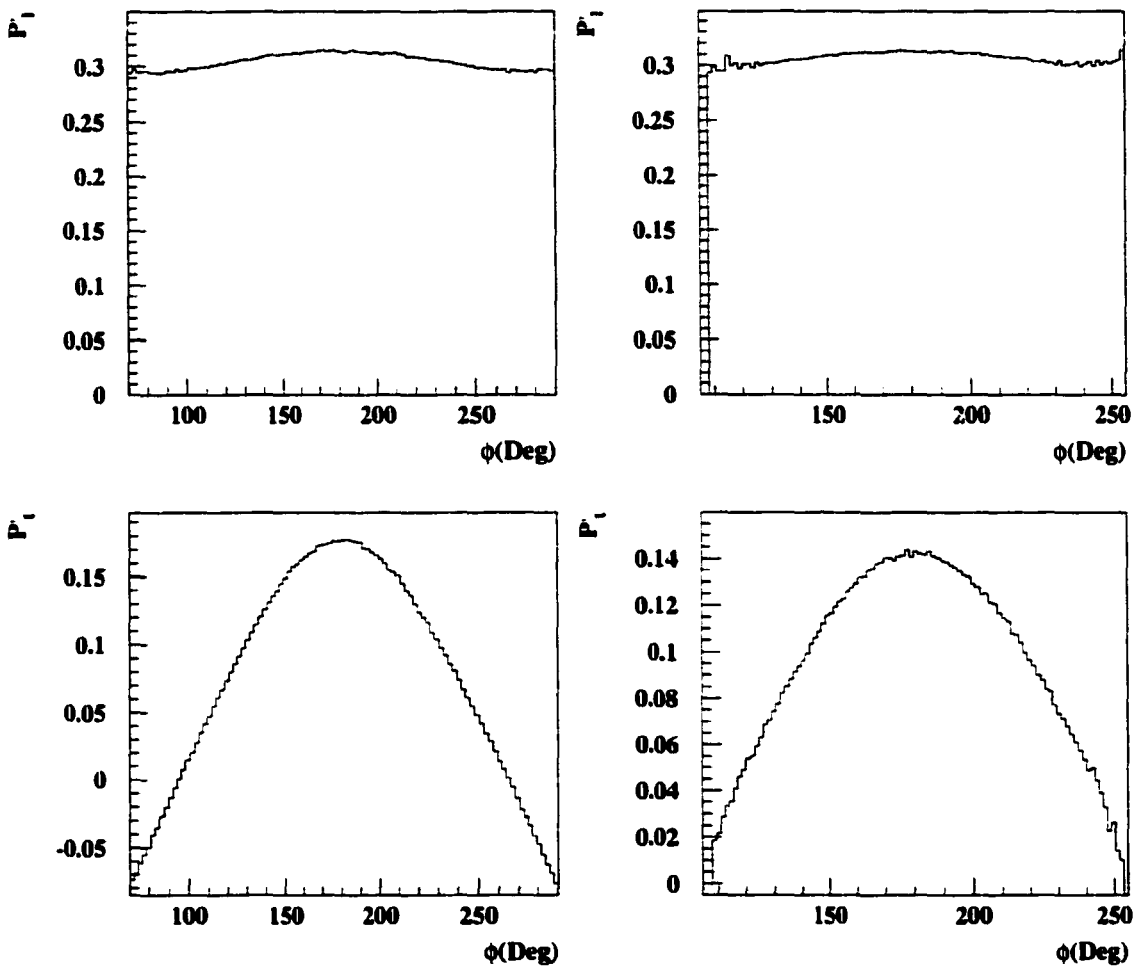

Figure 6.9: Variation of polarization observables with ϕ in the reaction frame. The left hand side gives the values corresponding to the pmiss = 85 MeV/c setting, while the right hand side corresponds to the pmiss = 140 MeV/c setting. These plots were obtained through MCEEP with LEA, using DWIA response functions.

Due to this heavy dependence of P'_l on ϕ in the reaction frame, it was not meaningful to compare the data to acceptance-averaged theoretical values in this frame.

On the other hand, both P_l' and P_t' vary only very little with ϕ in the spectrometer fame as indicated by Figure 6.6. Due to this reason all the comparisons of the present results to the theory were done in the spectrometer frame.

Mixing of other polarization observables in the spectrometer frame.

The polarization observables are initially calculated by the theorists in the reaction frame. When these observables are rotated into the spectrometer frame, all three components in the reaction frame mix to give each observable in the spectrometer frame. However, since we are measuring helicity-dependent polarizations from the difference distributions of the helicity + and helicity - signals there is no possibility that we can get mixing of helicity-independent polarization components into the helicity dependent ones. Since we were not exactly in in-plane kinematics (as mentioned earlier the azimuthal angle ϕ has a wide range in the pmiss = 85 MeV/c setting) there are some helicity-dependent out-of-plane polarization components that can contribute to our measurement. As discussed in Chapter 2, the helicity-dependent normal component P_n' is the polarization component that is not present in the in-plane case, but comes in the general out-of-plane case, given by

$$\sigma_0 P_n' = K\sigma_M(V_{LT}' R_{LT}'^N \sin\phi). \tag{6.12}$$

As indicated in the discussion on the response functions in Chapter 2, $R_{LT}'^N$ is non-zero in both PWIA and in DWIA. The contribution from this helicity-dependent P_n' in the reaction frame to the P_l' and P_t' calculated in the spectrometer frame are given in the Table 6.5. Due to the way the different contributions mix, the P_n' contribution to P_t' is much more significant than to P_l'. As expected the table shows that the contributions of P_n' to the P_t' at the pmiss = 85 MeV/c setting is almost an order of magnitude larger than at the 140 MeV/c setting.

Kinematic point	P'_n on (P'_l)	P'_n on (P'_t)
85 $1p_{1/2}$	0.0009	-0.1060
85 $1p_{3/2}$	0.0010	-0.0941
85 $1s_{1/2}$	0.0010	-0.0637
140 $1p_{1/2}$	0.0007	-0.0297
140 $1p_{3/2}$	0.0007	-0.0258
140 $1s_{1/2}$	0.0006	-0.0184

Table 6.5: Contribution from the helicity-dependent normal component, P'_n in the reaction frame to, P'_l and P'_t, calculated in the spectrometer frame.

Systematic uncertainties.

The main sources of systematic errors for this experiment are associated with the knowledge of spin precession through the hadron spectrometer. kinematical quantities, analyzing power and the incident beam polarization.

Error type	$\frac{\Delta P'_l}{P'_l}(\%)$	$\frac{\Delta P'_t}{P'_t}(\%)$	$\frac{\Delta(G_E/G_M)}{(G_E/G_M)}(\%)$
y_{tg} (1.5 mm)	0.45	0.30	0.7
θ_{tg} (2 mr)	0.40	0.26	0.6
ϕ_{tg} (1 mr)	0.33	0.23	0.5
$\frac{\Delta P_p}{P_p}$ (1.5×10^{-3})	0.15	0.15	0.5
Total on spin	0.61	0.43	1.04

Table 6.6: Systematic uncertainties on P'_l, P'_t, and $\mu(G_E/G_M)$ due to spin precession.

The range of the kinematical quantities were fed in to the spin precession analysis code to obtain the total systematic uncertainty due to the spin precession on individual

polarization-transfer observables and on $\mu G_E/G_M$. The percentage errors due to spin precession are given in Table 6.6. Here total systematic error is calculated by adding individual errors in quadrature.

Table 6.7 gives the systematic uncertainties due to other variables, obtained using MCEEP and the model LEA. For the beam polarization we assumed a 5% systematic uncertainty, although the FPP and Mott values agreed to better than 2%. Uncertainty due to beam polarization is the largest systematic error for this analysis. However, from the current Molar and Mott measurements in Hall A, the systematic uncertainty can be quoted as 3% for future measurements. Both Table 6.6 and Table 6.7 numbers include the effects due to finite acceptances.

Error type	$\frac{\Delta P'_l}{P'_l}(\%)$	$\frac{\Delta P'_t}{P'_t}(\%)$	$\frac{\Delta(G_E/G_M)}{(G_E/G_M)}(\%)$
A_c (2%)	2.0	2.0	0.0
h (5%)	5.0	5.0	0.0
θ_e (1 mr)	0.16	0.14	0.21
$\frac{\Delta E_i}{E_i}$ (1.0×10^{-3})	0.03	0.07	0.08
$\frac{\Delta P_e}{P_e}$ (1.5×10^{-3})	0.00	0.00	0.00
Total (with spin)	5.42	5.40	1.06

Table 6.7: Systematic uncertainties on P'_l, P'_t, and (μ G_E/G_M) due to spin precession.

To estimate the model uncertainty we again used 2 different DWIA theoretical calculations; DWIA non-relativistic from LEA and DWIA relativistic from Van Orden. The model uncertainty including only the p states for the two kinematic settings give values of 3.35% and 6.02% for P'_l and P'_t respectively, and if the s states are also included, the model uncertainties are 4.02% and 6.70% for P'_l and P'_t respectively.

Quantification of the medium modification effects on the form factor ratio.

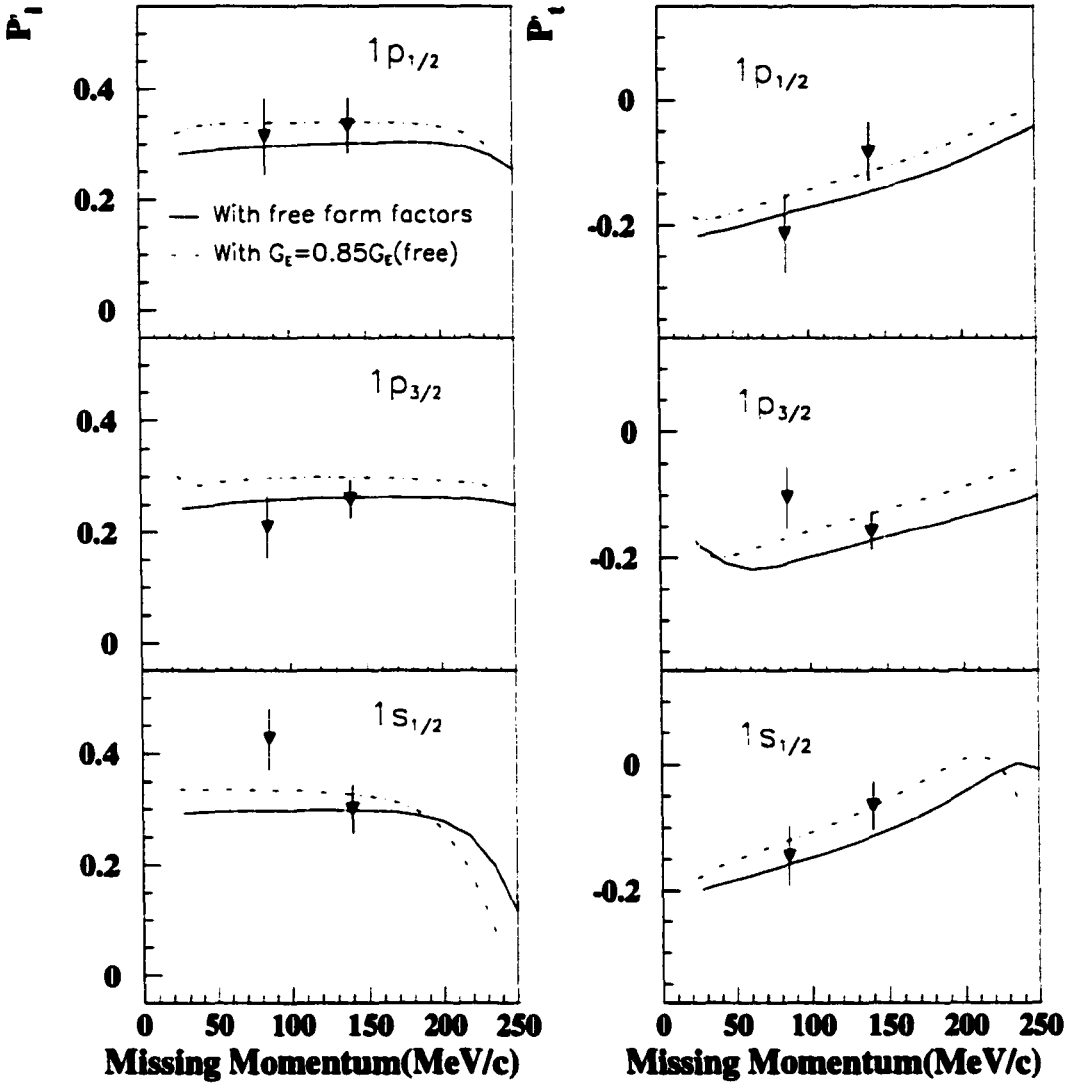

Figure 6.10: Comparison of P_l' and P_t' for a form factor suppression of 15% with free form factors. P_l' and P_t' experimental results with theory using Kelly's code LEA for the three states of ^{16}O. The solid line corresponds to free values of the form factors while the dashed line corresponds to a suppression of 15% of the charge form factor. The theoretical motivation for this is discussed in detail in Chapter 3.

As discussed in Chapter 3, the calculations by Thomas *et al.* [96] have indicated that at the kinematics of this experiment, the electric form factor of the proton should be suppressed by $\sim$ 15% due to medium effects, while the magnetic form factor should be basically unchanged. Thus, in order to quantify the medium modification effects on the proton, we performed the LEA calculation, changing the electric form factor by 15% from its free value while keeping the magnetic form factor as it is, and obtained P_l' and P_t'. The P_l', P_t' curves thus obtained for each state, compared to the experimental results are shown in Figure 6.10.

As the figure indicates, there is a distinct difference between the two theoretical curves. However, the high statistical uncertainty of the experimental results prevents us from distinguishing between the two curves. Since the systematic uncertainties for the experimental results are very small (less than 3%), if one does a high statistics measurement using the recoil polarization technique to quantify the medium modification effects using the FPP at Jefferson Lab Hall A, one should be able to distinguish between the two curves. Being the first experiment to use polarized beam at Jefferson Lab, this experiment suffered heavily due to beam unavailability. However, being the first experiment to look for medium modification effects using the recoil polarization technique, this experiment has been successful in defining a low systematic uncertainty method for future experiments.

Possible $\mu\frac{G_E}{G_M}$ ratio for proton inside ^{16}O and a super ratio.

We know that in the case of a free proton P_t'/P_l' ratio is directly proportional to the form factor ratio with a known kinematic factor, $\mu\,\frac{E_i+E_f}{2M_N}\tan(\theta_e/2)$ which is equal to 1.37 in our kinematics. As far as the one body current operator is concerned, the P_t'/P_l' ratio for ^{16}O is also only a function of the form factor ratio and not a function of individual form factors. The relationship between the polarization observable ratio and the form factor ratio for the proton inside ^{16}O nucleus can be written as a linear

function (at least for the p states)

$$\frac{P_t'}{P_l'}K' = \mu\frac{G_E}{G_M}. \tag{6.13}$$

We used the code LEA to obtain the constant K' for each of the kinematic points of this experiment. Using these constants K', and our experimental results for P_t'/P_l', we were able to calculate possible form factor ratios for the proton inside the ^{16}O nucleus. The results are shown in the Table 6.8.

Kinematic point	K'	$\mu\frac{G_E}{G_M}$
85 $1p_{1/2}$	1.555	1.120±0.401
85 $1p_{3/2}$	1.403	0.679±0.374
85 $1s_{1/2}$	1.843	0.704±0.244
140 $1p_{1/2}$	2.001	0.523±0.318
140 $1p_{3/2}$	1.734	1.064±0.247
140 $1s_{1/2}$	2.899	0.652±0.411

Table 6.8: Possible form factor ratios, ($\mu\ G_E/G_M$) for ^{16}O, assuming that the one body current operator provides an adequate description of the $(\vec{e}, e'\vec{p})$ reaction; see text for details.

We combined the $\mu\ G_E/G_M$ values given for different states, weighting by the statistical error. However we did not include the $1s_{1/2}$ state data in this average because the $1s_{1/2}$ state is a wide bump spread out in missing energy and therefore it is not possible to separate $1s_{1/2}$ contributions from the continuum contributions. Thus we took the weighted average of the p states to obtain the $\mu\ G_E/G_M$ ratio at each kinematic setting. This gives $\mu\ G_E/G_M$ values of 0.84±0.27 and 0.88±0.20 for pmiss = 85 MeV/c and pmiss = 140 MeV/c respectively and an overall average of 0.87±0.16 for the $\mu\frac{G_E}{G_M}$ ratio (weighted by the cross section and by the statistical uncertainty). The world data using the cross section also predicts approximately a value of 0.81

for the ratio, $\mu G_E/G_M$ inside the nuclear medium and this again agrees with our measurement qualitatively (going in the right direction) as well as quantitatively even though with a large statistical uncertainty. Note that since this result is independent of the analyzing power of the FPP (A_c) and the beam polarization (h), it is a cleaner result than the individual polarization observables. Note that the overall average does not take into account the fact that K' depends on the individual state, nor the fact that $\mu\ G_E/G_M$ could depend on the individual nuclear state.

A better way to take an overall average that is independent of the state is to compute the super ratio,

$$\frac{(\frac{P'_t}{P'_l})_{experiment}}{(\frac{P'_t}{P'_l})^{free}_{theory}}. \tag{6.14}$$

Here $(G_E/G_M)^{free}_{theory}$ is the polarization observable ratio assuming the free values for the bound nucleon form factors. If we assume that the one body current operator provides an adequate description of the ^{16}O $(\vec{e}, e'\vec{p})$ reaction, and the differences between theory and experiment arises solely from medium modification effects of the nucleon form factors, we can write

$$\frac{(\frac{P_t}{P_l})_{experiment}}{(\frac{P_t}{P_l})^{free}_{theory}} = \frac{(\frac{G_E}{G_M})_{medium}}{(\frac{G_E}{G_M})_{free}}. \tag{6.15}$$

Given these conditions we can consider the super ratio numbers given in Table 6.9 as a measure of the medium modification effects on the nucleon. The results are consistent with no medium modifications to the free nucleon form factors within our statistical sensitivity.

Kinematic point	$\frac{(\frac{G_E}{G_M})_{medium}}{(\frac{G_E}{G_M})_{free}}$
85 MeV/c point	0.936±0.304
140 MeV/c point	0.982±0.224
Overall	0.968±0.181

Table 6.9: Possible super ratio's $(\frac{(p'_l/p'_t)_{experiment}}{(p'_l/p'_t|^{prime})^{free}_{theory}})$ for ^{16}O, assuming one body current operator is an adequate description (see text for details).

6.3 Drawbacks of this experiment and improvements for the future.

There were several problems that prevented us from doing the best possible measurement. The foremost drawback was the low statistics. Being the first physics experiment to use polarized beam at Jefferson Lab, and being one of the first experiments in Hall A, this experiment suffered heavily due to accelerator and equipment failures. Total beam time for the polarization transfer measurements was only about 150 hours. Frequent "recesiations" of the polarized source and accelerator down times reduced the beam availability to the hall.

Even though the beam polarization is immaterial to the determination of the P'_t/P'_l ratio, the product, hA_c is important for the determination of the individual polarization observables. Higher values of h and A_c correspond to lower statistical uncertainty for individual polarizations. The electron beam polarization during this experiment was low (~29 - 30%) at an average beam current of only ~ 40μA. The polarized source group at TJNAF was beginning to understand the polarized beam system at the time of this experiment. After a year of operation and practice, they

are now able to deliver 70% polarized beam with over 100μA with a new kind of source (strained GaAs) where as earlier they were using a bulk GaAs crystal.

Another pitfall was the inefficiencies of the FPP chambers. One of the rear FPP chambers (ch. 3) had a high level of inefficiency during the time of this experiment. Even though we had two "U" and two "V" planes in that chamber, there were times when not a single U or V plane of chamber 3 fired. This resulted in the rejection of $\sim$ 30% of the events. This also increased our statistical uncertainty. The FPP chambers had been close to 100% efficient at later time periods.

Of the two ^{16}O kinematic settings of this experiment, the 85 MeV/c kinematic setting contained a considerable out-of-plane contribution. As was described earlier in this chapter, this made it difficult for the results from this setting to be compared to the theoretical calculations in the reaction frame. There was mixing of other polarization observables as well. Thus instead of 85 MeV/c, if a setting with pmiss $\sim$ 100 MeV/c were chosen from this experiment, the measurement would have been "cleaner". Since the momentum distribution for the p states peak around 100 MeV/c, as shown in Figure 6.11, this choice would have been better in terms of counts as well. At higher pmiss the s state is weaker. However, since the s state is a wide bump spread over missing energy it is difficult to isolate the s state contributions from the continuum contributions. This makes the s-state in ^{16}O, a poor choice to compare to theory to look for medium modifications. Thus the kinematics of this experiment could be optimized for the p states.

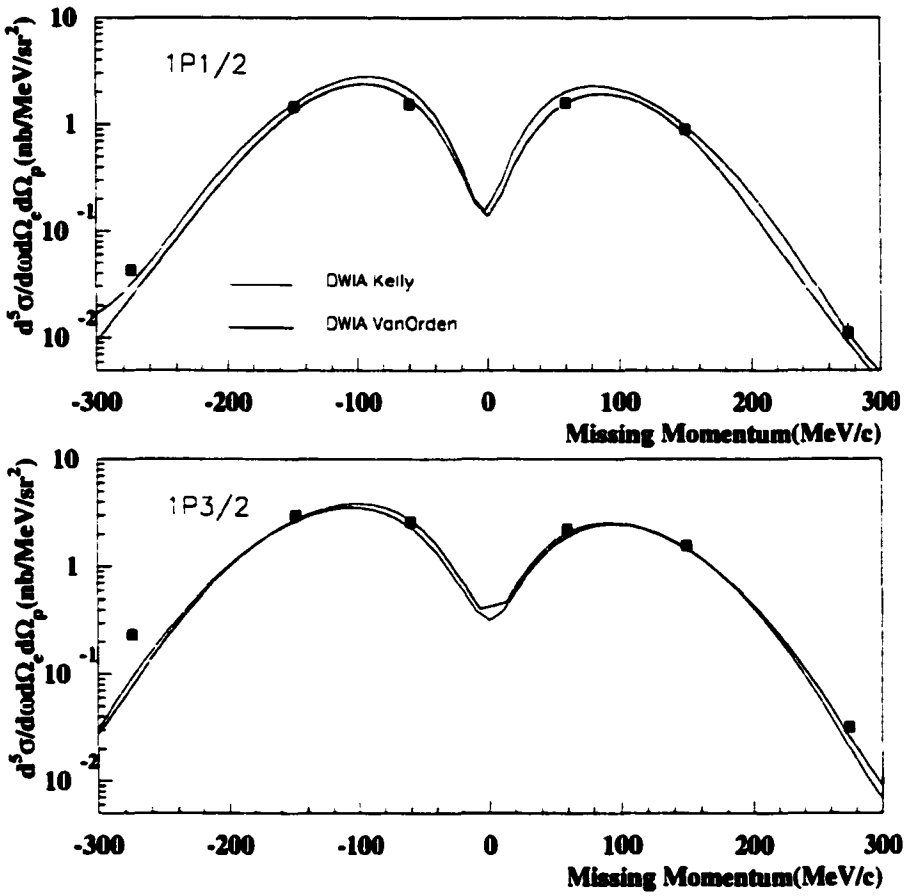

Figure 6.11: Momentum distributions obtained for $1p_{1/2}$ and $1p_{3/2}$ states of ^{16}O taken from Jefferson Lab experiment 89003 [128].

6.4 Future of polarization transfer measurements and search for medium modification effects at TJNAF.

Several high statistics measurements aimed at investigating medium modification effects are scheduled to run at Jefferson Lab.

One experiment which is closely related to the present experiment is experiment E93049 [129] which is scheduled to run in the spring of 2000 in Hall A. This

experiment is designed to measure the polarization transfer observables in the reaction ^{4}He$(\vec{e}, e'\vec{p})^3$H using the Hall A, FPP, and thereby to quantify the effects of medium modification effects. For this reaction the only valence state available is the $1s_{1/2}$ state. The $1s_{1/2}$ state being in a high density region will be very favorable in looking for medium modification effects. In this experiment P_l' and P_t' will be determined as a function of Q^2, for $0.8 < Q^2 < 4$ (GeV/c)^2 and as a function of missing momentum in the range of 0 to 250 MeV/c. As in the case of the present experiment, the determination of the form factor ratio will have a small systematic error, since only one beam energy will be used and the kinematic configuration will be fixed. However, their estimated statistical errors are much smaller than the statistical errors for the present experiment. The proposed measurements will give an accurate experimental value of the ratio P_l'/P_t' with a statistical uncertainty of about 2%, 3% and 5% for Q^2 of 0.8, 1.5, and 3(GeV/c)^2 respectively. The predicted P_l' and P_t' polarization components of the ejected proton versus missing momentum are shown in Figure 6.12. Here, P_X', P_Z' and P_Y^0 correspond to P_t', P_l' and P_n respectively. Again, it is seen that, for P_l' and P_t' the deviations from PWIA due to charge-exchange, FSI and MEC effects are negligible for missing momenta below 300 MeV/c.

The predictions from A.W Thomas *et al.* [130], for ^{4}He for the medium modification effects are shown in Figure 6.13. With the high statistical precision anticipated, E93049 will be able to definitely test the calculations of Thomas *et al.*, and also several other calculations that present the medium modification effects of the nucleon.

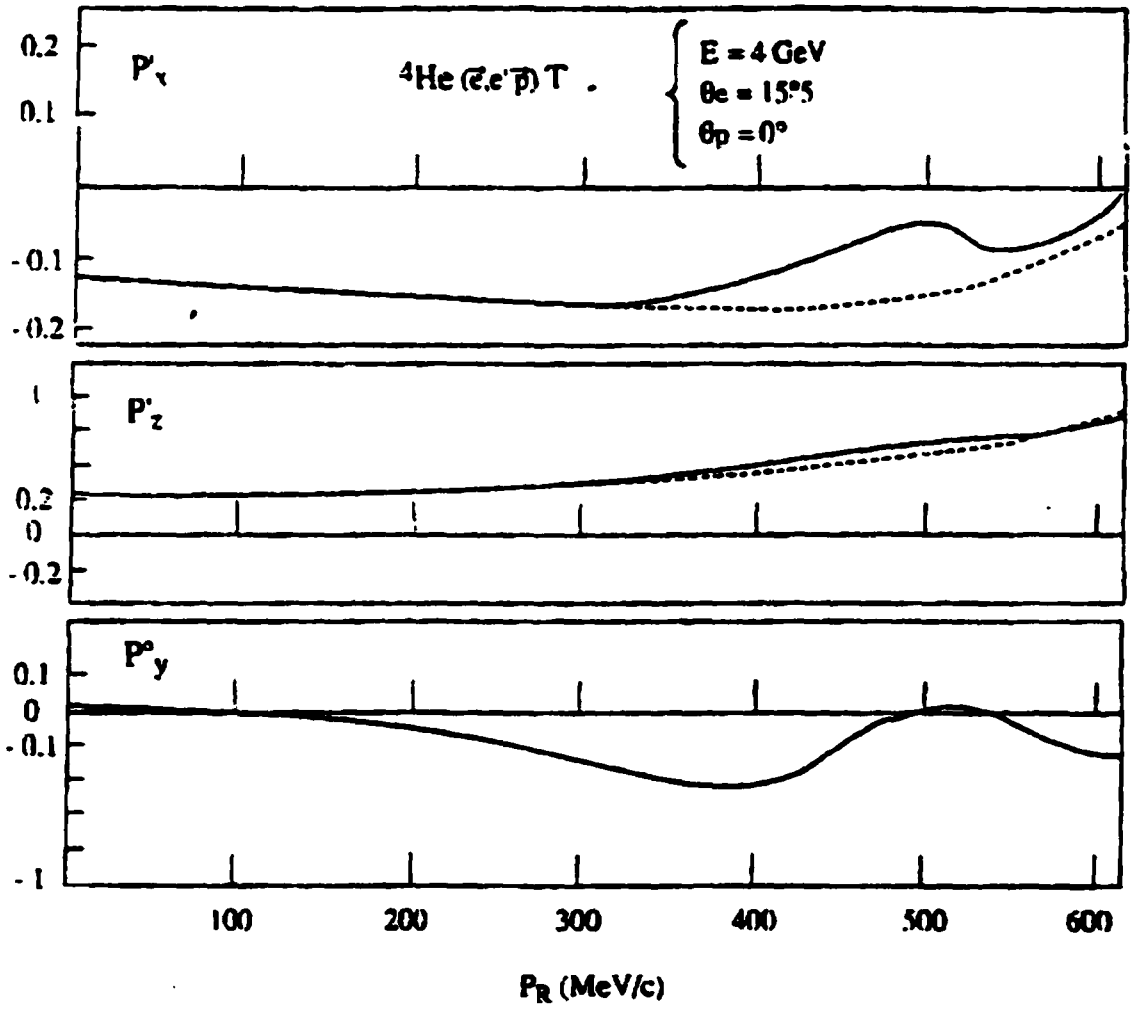

Figure 6.12: The spin transfer polarizations P'_X, P'_Z, and P^0_Y of the reaction $^4\mathrm{He}(\vec{e}, e'\vec{p})^3H$ calculated by Laget [129]. The dashed curve is the PWIA prediction, and the solid curve represents the results of the calculation including FSI and MEC effects.

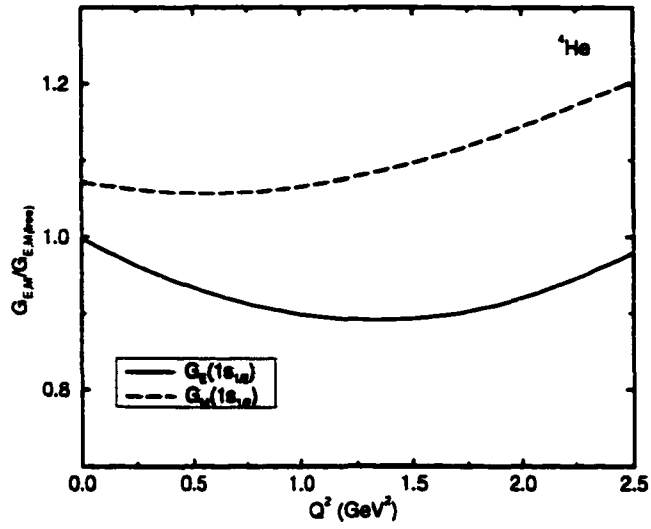

Figure 6.13: Predictions for the change of the charge (G_E) and magnetic (G_M) form factors with respect to the free values for ^{4}He performed by the Adelaide group using a QMC model [130].

6.5 Summary and conclusions.

Polarization transfer observables, P_l' and P_t' for the $^{16}O(\vec{e}, e'\vec{p})$ reaction have been measured in the quasielastic region with Q^2=0.8 (GeV/c)^2 in perpendicular kinematics for the three states $1p_{1/2}$, $1p_{3/2}$ and $1s_{1/2}$ at two recoil momenta points, 85 MeV/c and 140 MeV/c. The same measurement was performed for the free proton at the same value of Q^2, and the form factor ratio, $\mu\, G_E/G_M$ for the free proton was calculated and compared to existing theoretical calculations. A free form factor ratio of 0.90±0.04 was obtained at $Q^2 = 0.8$ (GeV/c)^2.

The individual polarization transfer results were compared to a non-relativistic DWIA calculation from Kelly and non-relativistic and relativistic DWIA calculations from Van Orden. Both calculations used the free nucleon values for the form factors of the proton inside ^{16}O nucleus. These calculations used MMD and Höhler models

to obtain the free values of nucleon form factors. At a Q^2 of $0.8(GeV/c)^2$, and both these models agree with the free nucleon form factor ratio of 0.9 measured during this experiment.

The specific conclusions can be summarized as follows:

- This experiment measured a value of 0.901 ± 0.046 for the form factor ratio, $\mu G_E/G_M$ for the free proton at Q^2 of 0.8 $(GeV/c)^2$, and this value agrees with the vector meson dominance model calculations by Meisner *et al.* (MMD model). This allowed a direct comparison of the form factor ratio between the free proton and the bound proton from a simultaneous measurement, hence reducing systematic uncertainties.

- Comparison of the measured polarization observables and the theory evaluated for free form factor values show good agreement.

- Within the statistical precision of this experiment this indicates that the medium modifications are less than 18%.

- However, due to high statistical uncertainty, this experiment could not distinguish between a calculation using free form factor values and one using form factor values suppressed by 15% as predicted by Thomas *et al.*

- Both theoretical and experimental arguments show that the recoil polarimetry technique is a powerful and precise tool for studying medium modification effects of the nucleon.

- Systematic uncertainties on the form factor ratio using the recoil polarimetry technique can be as small as 3%.

This benchmark experiment using the recoil polarimetry technique, to look for medium modification effects has been successful in showing that due to the small systematic uncertainty, a similar but high statistics measurement would be able to

definitively test medium modification models. This is just the beginning of the search for medium modification effects using the recoil polarimetry technique, the times ahead will be very exciting.

Appendix A

Alignment of the Focal Plane Polarimeter.

Software alignment of the polarimeter chambers is necessary for the proton polarization data analysis. The FPP consists of 2 front straw chambers and two rear straw chambers (Figure 4.8). Each chamber has 6 straw planes. Chambers 1, 2, and 4 each have three "u" planes and three "v" planes, while chamber 3 has two "u", two "v" and two "x" planes, see Figure 4.14. Using each chamber one can determine a point on the actual particle track in space. Therefore, the front two chambers measure the incident track to the carbon block in space, while the rear two chambers measure the scattered track. The distribution of the azimuthal scattering angle is a measure of the polarization of the protons. The azimuthal scattering angle is determined from the difference between the orientations of the front and the rear tracks. Thus in order to properly determine the azimuthal scattering angle distribution, one must align the four FPP chambers with respect to each other (internal alignment). Furthermore, since we use the polarizations measured at the focal plane by the FPP, to obtain the target polarizations, with the aid of a transport matrix, we must also align the four chambers to the VDC's (absolute alignment).

Since the Hall A FPP is not aligned physically at all, one has to do a careful

software alignment, taking into consideration the misalignments between each pair in positions as well as in angles. To test the validity of the alignment method, during the FPP commissioning in Spring 1997 we moved each FPP chamber in the y direction (only direction the chambers have flexibility of motion) by known distances. When these data were analyzed, the alignment method gave us the shifted distances with the correct direction (+ or -) to within a millimeter. Furthermore, after moving the chambers back to where they were before, and using dowel pins to ensure the physical reproducibility to a few micron level, the alignment parameters were found to be reproducible to within a mm in position and a couple of mr in angles.

If the chambers were aligned properly, the ϕ_{fpp} distribution for all the unpolarized scattered particles (helicity sum) should give us a flat distribution for H(e,e'p) data.

A.1 Alignment procedure.

Each FPP chamber was aligned separately to the VDC's. This takes care of angular and position misalignments within the group; front or rear. We used only the "golden tracks" for this alignment. A "golden track" is defined as a track for which each plane of that chamber got a single hit. For this alignment, each FPP chamber has six physical offsets with respect to the central ray and the central plane:

- Three position offsets:
  - u_{off} - Distance (in cm) to the first straw of u plane from the center.
  - v_{off} - Distance (in cm) to the first straw of v plane from the center.
  - z_{off} - z position (in cm) of the middle of the chamber with respect to the VDC center.
- Three angular offsets:

- θ_{uv} - Angle of in-plane rotation (in degrees) of the chamber with respect to the central uv axis.
- θ_{zu} - Angle of out-of-plane rotation (in degrees) of the chamber around the z axis, in the u direction.
- θ_{zv} - Angle of out-of-plane rotation (in degrees) of the chamber around the z axis, in the v direction.

These offsets are shown in figures A.1 and A.2

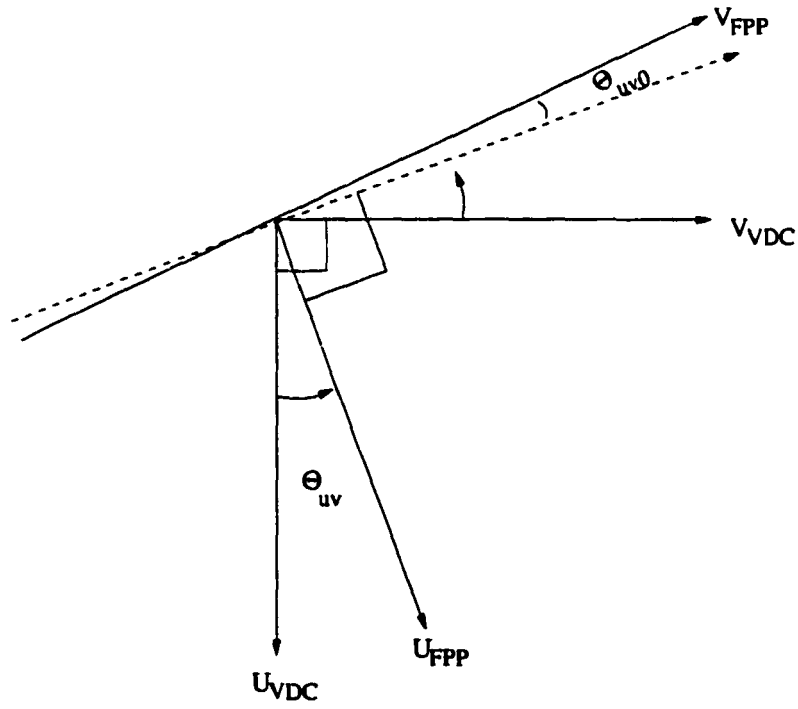

Figure A.1: In-plane rotation from VDC to FPP.

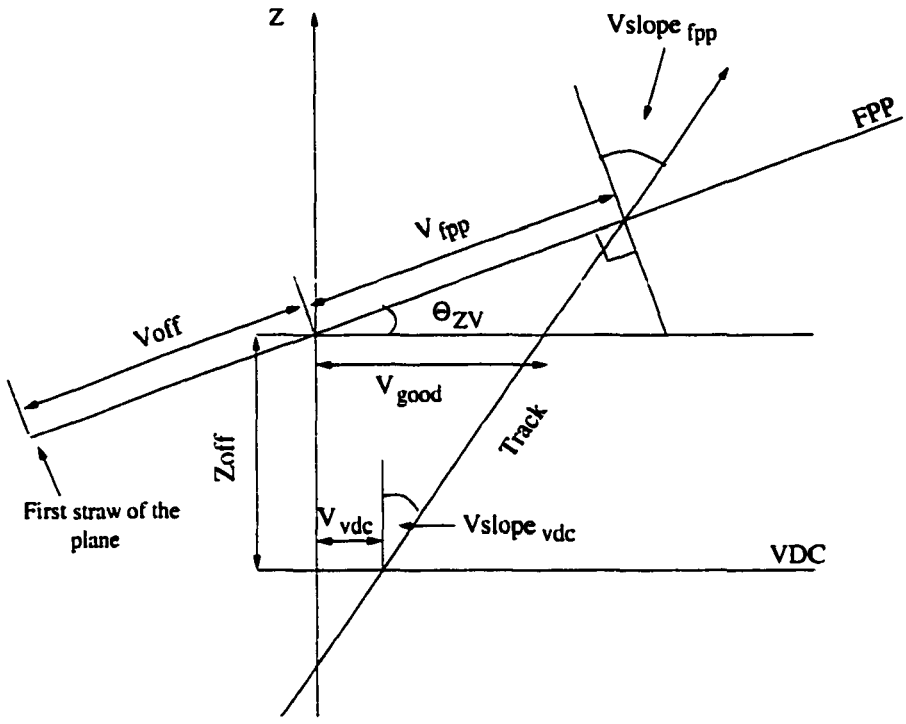

Figure A.2: The cross-section of an FPP chamber on the ZV plane showing the out-of-plane rotation.

For each golden track, the VDC u, v positions (in cm) and u-slope ,v-slope angles (in radians) were obtained using the VDC track information. The same variables were obtained for each FPP chamber at the mid-plane of that chamber, using the FPP track information. Using the positions and angles of the track calculated at the VDC, the track was projected up to the mid-plane of each FPP chamber. Since VDC's have a better angular resolution (0.3 mr) than the FPP (about 3 mr), it is always better to project VDC values on to the FPP than the other way around. Then for the difference between the projected VDC values (positions as well as angles) and the FPP values at each FPP chamber, a χ^2 minimization was performed to obtain the best values for the offsets given above. The relevant equations for the projection are given below.

For the position calculations:

In Figure A.2

$$Z = \frac{Zoff + Uoff \times tan\theta_{ZU} + Voff \times tan\theta_{ZV}}{1 - tan(Uslope_{vdc}) \times tan\theta_{ZU} - tan(Vslope_{vdc}) \times tan\theta_{ZV}} \tag{A.1}$$

$$V_{fpp} = \sqrt{(V_{vdc} + Vslope_{vdc} \times z)^2 + (z - zoff)^2} \tag{A.2}$$

$$U_{fpp} = \sqrt{(U_{vdc} + Uslope_{vdc} \times z)^2 + (z - zoff)^2}. \tag{A.3}$$

From Figure A.2 to Figure A.1

$$V_{VDC} = V_{fpp} - Voff \tag{A.4}$$

$$U_{VDC} = U_{fpp} - Uoff. \tag{A.5}$$

In Figure A.1

$$V_{FPP} = cos(\theta_{uv} + \theta_{uv0}) \times V_{VDC} - sin(\theta_{uv} + \theta_{uv0}) \times U_{VDC} \tag{A.6}$$

$$U_{FPP} = cos\theta_{uv} \times U_{VDC} + sin\theta_{uv} \times V_{VDC}. \tag{A.7}$$

For the angle calculation:

From Figure A.2

$$Vslope'_{fpp} = \theta_{ZV} + Vslope_{vdc} \tag{A.8}$$

$$Uslope'_{fpp} = \theta_{ZU} + Uslope_{vdc}. \tag{A.9}$$

In Figure A.1

$$Vslope_{FPP} = cos(\theta_{uv} + \theta_{uv0}) \times Vslope'_{fpp} - sin(\theta_{uv} + \theta_{uv0}) \times Uslope'_{fpp} \tag{A.10}$$

$$Uslope_{fpp} = cos\theta_{uv} \times Uslope'_{fpp} + sin\theta_{uv} \times Vslope'_{fpp}. \tag{A.11}$$

Figure A.3 shows the difference distributions for the tracks reconstructed using the fourth FPP chamber and using VDC's after the alignment procedure was performed.

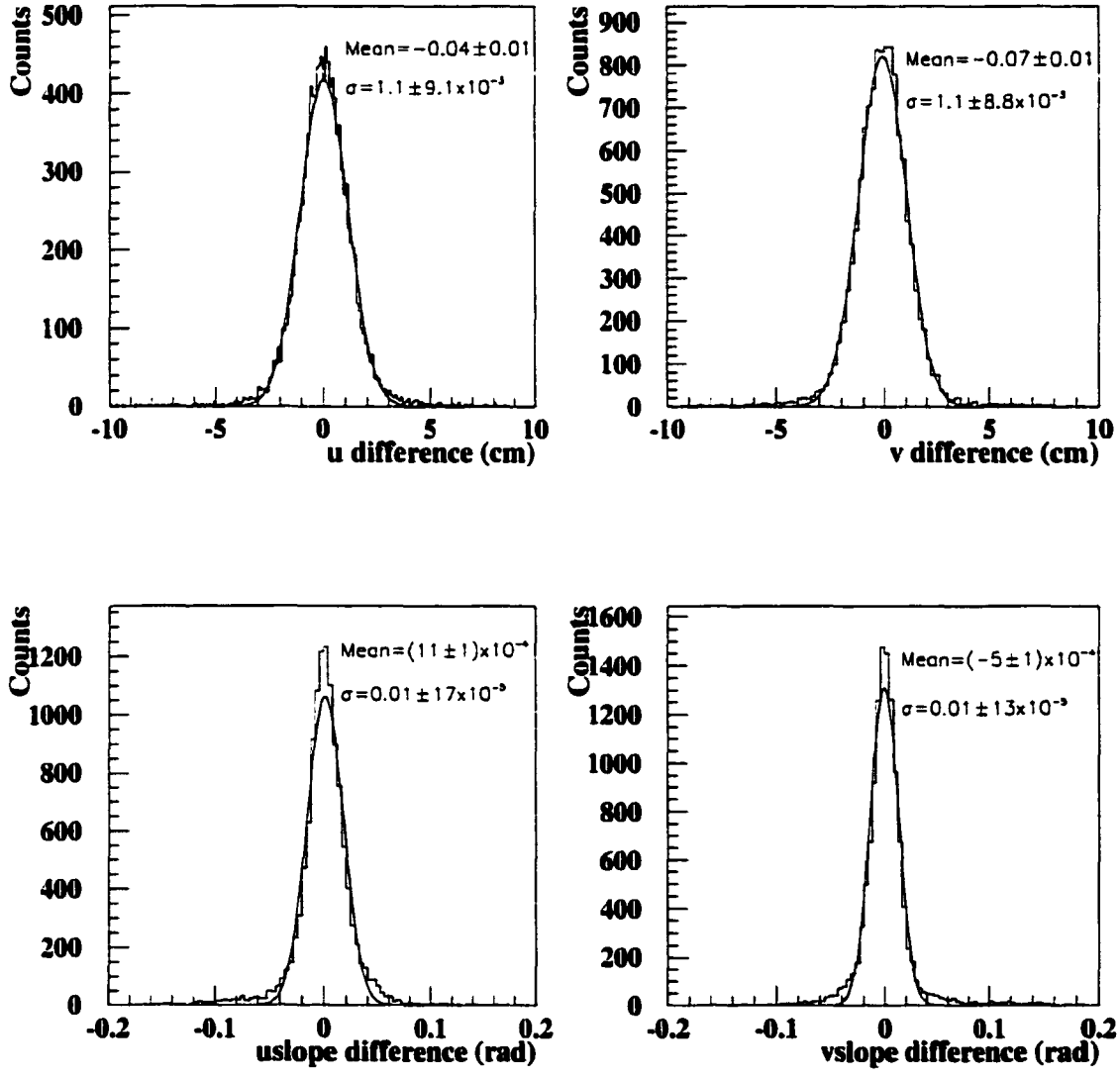

Figure A.3: Difference distributions for the four variables u, v, u-angle and v-angle between the measured values from chamber 4, FPP and VDC after the alignment procedure was performed. The mean and the resolution for each variable are shown on the plots.

Such obtained offsets for the FPP at Hall A are given in the table A.1. The table A.2 gives the physically meaningful offsets in x and y directions for the misalignment of each chamber with respect to the VDC coordinate system.

Offset	Ch. 1	Ch. 2	Ch. 3	Ch. 4
Z_{off}cm	189.093	305.473	397.256	433.977
U_{off}cm	-100.442	-102.149	-134.422	-152.937
V_{off}cm	-80.777	-80.506	-123.247	-138.689
θ^o_{uv}	0.043	0.200	0.381	0.032
θ^o_{zu}	-0.055	-0.169	-0.574	0.330
θ^o_{zv}	-0.832	-0.916	-1.089	-0.860

Table A.1: Offsets obtained for FPP chambers.

Chamber	dx (cm)	dy (cm)
1	-5.23	1.07
2	-5.75	-0.05
3	-3.44	-0.72
4	-6.08	0.52

Table A.2: physical offsets of chambers with respect to VDC's

A.2 Incorporation of alignment in the tracking routine.

We used the offsets calculated using the alignment procedure along with the above equations to transform the positions and angles measured by each FPP plane in to the VDC coordinate system. As the equations indicate, the transformation of a u position measured by a "u" plane to u_{VDC} also requires the knowledge of the v_{FPP} position at that "u" plane. Similarly, the transformation of a v position also require the knowledge of the u coordinate at that "v" plane. Since within one chamber, the planes are parallel to each other, we can project the position measured by the "u" planes of one chamber on to each v plane of the same chamber and use those as the u positions on the "v" planes. Figure A.4 illustrates how this projection is performed.

After the transformation to the VDC coordinates, each hit will have a corrected u or a v position with respect to the VDC coordinate system. These values are used as inputs to the tracking routine.

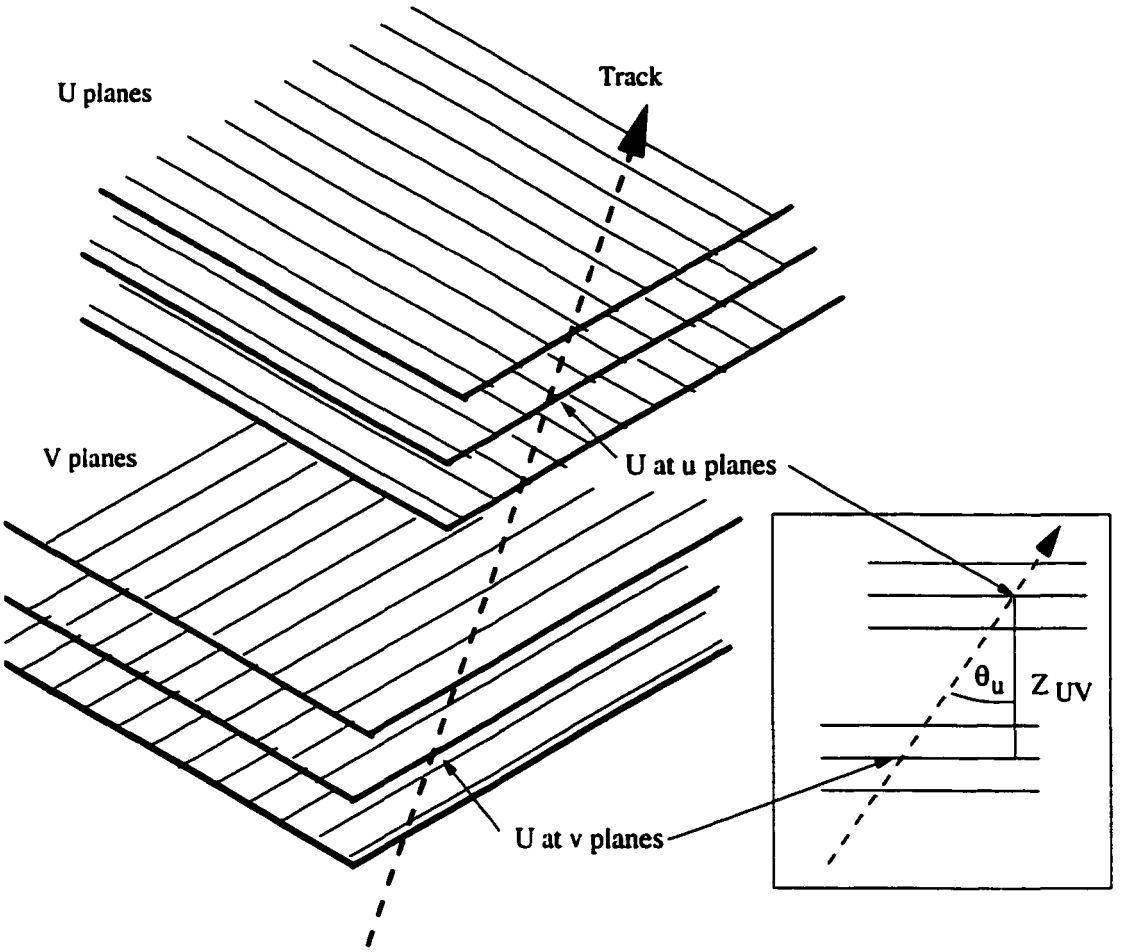

Figure A.4: Projection of the u positions on to the "v" planes.

Once the positions measured at the planes are transformed in to VDC coordinates, the positions measured at all six front u planes (three from chamber 1 and three from chamber 2) are used to calculate the front u position and the u angle. Similarly the front v planes are used to calculate the front v position and front v angle. The use of all six planes allows for higher accuracy of the angle calculations due to the long lever arm. In case some planes did not fire, we can use any number of planes in tracking up to six. Same procedure was used for the rear chambers. Position resolutions achieved were of the order of 0.5 cm and the angular resolutions were of the order of 5 mrad (using both chambers to determine the positions and angles).

This method resulted in instrumental asymmetries of the order of 0.006 (all four terms. as shown in table A.3). A plot of the Cartesian scattered angles θ_{sc} vs ϕ_{sc} provides a qualitative measure of the quality of alignment. See Figure A.5. The symmetric "equi-strength" circles indicate a high level of alignment for the present case.

Term	Value	Error
cosϕ	-0.0056	0.0018
Sinϕ	0.0058	0.0018
cos2ϕ	0.0027	0.0018
Sin2ϕ	0.0054	0.0018

Table A.3: Values obtained for the instrumental asymmetries

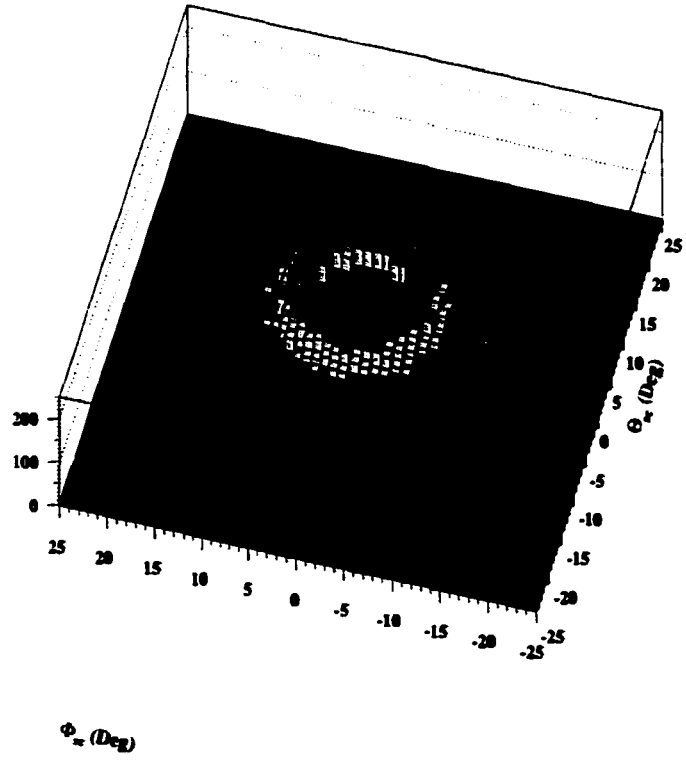

Figure A.5: θ_{sc} vs ϕ_{sc} distribution for unpolarized events.

Appendix B

Beam energy from H(e,e′p) angles

In this appendix we deduce the formula used for the beam energy measurement in Chapter 5.

From Figure 5.9, e_f denotes the scattered electron, p denotes the momentum of the recoiling proton and e_i denotes the incident electron. E's for the energies and M's for the masses are used.

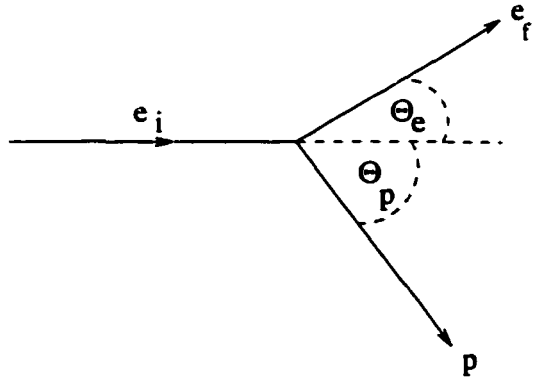

Figure B.1: Incident, scattered electrons and scattered proton for the (e,e′p) reaction.

From the conservation of energy,

$$E_i + M_p = E_f + E_p. \tag{B.1}$$

From the conservation of momentum in the incident electron direction

$$E_i = E_f \cos\theta_e + p\cos\theta_p. \tag{B.2}$$

and in the direction perpendicular to the initial electron momentum

$$E_i \sin\theta_e = p\sin\theta_p. \tag{B.3}$$

Here we assume that the electron has zero mass in the extreme relativistic limit.

From equations A.2 and A.3 we can solve for E_f and p

$$E_f = E_i \frac{\sin\theta_p}{\sin\theta_t} \tag{B.4}$$

$$p = \frac{\sin\theta_e}{\sin\theta_t}. \tag{B.5}$$

Here $\theta_t = \theta_e + \theta_p$.

From equation A.1,

$$E_p = E_i + M_p - E_f. \tag{B.6}$$

Squaring this and using the fact that $E_p^2 = M_p^2 + p^2$,

$$p^2 = E_i^2 + E_f^2 + 2E_i M_p - 2E_i E_f - 2M_p E_f. \tag{B.7}$$

Finally substituting for E_f and p from A.4 and A.5 in equation A.7 and using $E_i = E_{beam}$,

$$E_{beam} = 2M_p \left[\frac{\sin\theta_t (\sin\theta_p - \sin\theta_t)}{(\sin\theta_p - \sin\theta_t)^2 - \sin^2\theta_e}\right]. \tag{B.8}$$

Appendix C

Event averaged spin matrix elements from COSY.

For the $1p_{1/2}$ state at pmiss = 85 MeV/c kinematic setting. Comparison to the simple dipole case shows the matrix elements S_{nt}, S_{tn}, S_{tl}, S_{lt} should be equal to zero and S_{tt} should be equal to one. Qualitatively the HRSH spin matrix elements show the similarity to a simple dipole behavior. Here the structure of the S_{lt} shows a high correlation with y_{tg}.

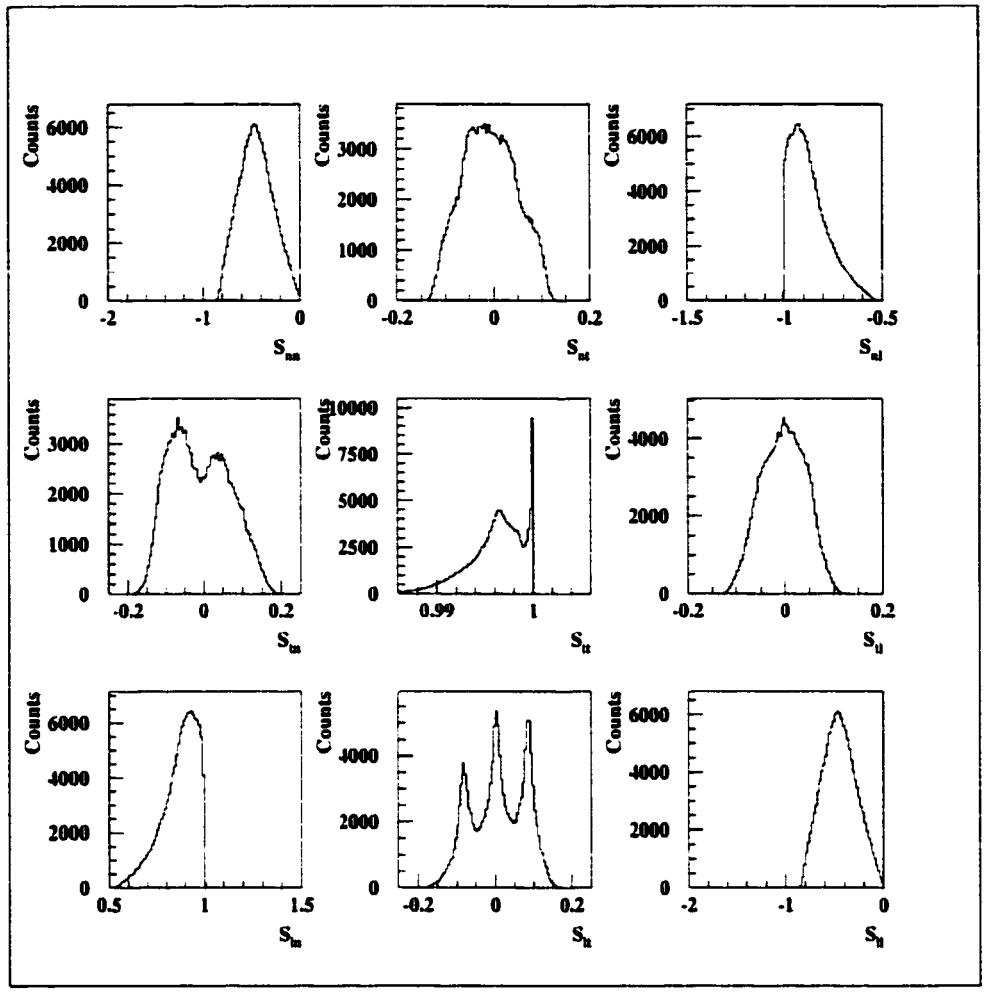

Figure C.1:

Appendix D

Mott measurements for each kinematic setting

Hydrogen data in parallel kinematics

Date	Polarization
19 July 97	0.334±0.029
19 July 97	0.349±0.029
20 July 97	0.356±0.029
21 July 97	0.384±0.025

^{16}O in 85 MeV/c Missing momentum point

Date	Polarization
21 July 97	0.300±0.032
21 July 97	0.314±0.025
22 July 97	0.325±0.025
23 July 97	0.291±0.026

26 July 97	0.327±0.025
28 July 97	0.329±0.026
29 July 97	0.326±0.025
31 July 97	0.300±0.025

^{16}O in 140 MeV/c Missing momentum point

Date	Polarization
31 July 97	0.329±0.026
1 August 97	0.317±0.025
2 August 97	0.308±0.025
2 August 97	0.326±0.025
2 August 97	0.302±0.025
3 August 97	0.327±0.025
3 August 97	0.284±0.025
4 August 97	0.314±0.026
4 August 97	0.293±0.025
5 August 97	0.293±0.025
5 August 97	0.278±0.025
5 August 97	0.276±0.026
5 August 97	0.308±0.025
5 August 97	0.276±0.026
5 August 97	0.280±0.025
5 August 97	0.277±0.025
5 August 97	0.289±0.026
5 August 97	0.309±0.026
6 August 97	0.296±0.025

6 August 97	0.270±0.026
7 August 97	0.317±0.025
7 August 97	0.285±0.025
8 August 97	0.280±0.025

Appendix E

Basic HRS tensor elements used for E-89033

See Eqns. 5.15, 5.20 and 5.24 for the definitions of the tensor elements.

E.1 HRSE

Element	C_0 term	C_1 term	C_2 term	C_3 term
t000	-1.0027E+00	-3.3012E-01	-3.2536E-02	1.2912E-03
y000	-7.2837E-03	3.2563E-03		
p000	-2.1774E-03	-8.9684E-04		
D000		8.5175E-02	1.0472E-02	
D100	-3.5017E-02	2.6963E-01	4.2004E-02	-2.4595E-02
D200	-1.4479E+00	5.7568E-01		
D002	2.4081E-01	-7.7477E-02	-6.7727E-01	
D020	3.6117E-01	-7.5655E-01	-7.9962E-01	
D011	2.6138E-01	6.8103E-01		
D300	2.4742E+01			

Element	C_0 term	C_1 term	C_2 term	C_3 term
D120	-3.1889E+01	1.9336E+01		
D102	-2.6759E+01			
D111	-1.5159E+01	-9.0963E+01		
D400	1.9030E+03			
D202	-9.9579E+02			
D220	-1.6571E+03			
D211	1.9152E+03			
D013	-1.4450E+02			
T100	-2.2707E+00	4.9131E-01	1.4908E-02	
T200	-7.2421E+00	2.6135E+00		
T002	1.2824E-01	4.1137E-01	3.6680E+00	
T011	1.0730E+00	-1.4196E+00	-3.7090E+00	
T020	-4.2284E-01	-3.6365E-01		
T120	2.5136E+01			
T102	2.0016E+01	-5.1216E+01		
T300	1.0336E+02			
T040	5.9637E+02			
T022	1.0304E+03			
T111	-2.1599E+01			
T202	-5.4090E+02			
T013	-1.0237E+03			
T031	-1.4686E+03			
T400	5.0437E+03			
P001	-6.9215E-01	-9.8569E-02	2.6903E-01	-1.0106E-01
P010	-3.2907E-01	2.7852E-01	-9.4349E-02	1.2984E-01
P012	-3.9218E+00	5.1591E+01		

Element	C_0 term	C_1 term	C_2 term	C_3 term
P110	3.0497E+00	-1.4259E-01	-7.7373E+00	
P101	5.9176E+00	-7.4720E-01	2.6263E+00	
P003	1.6310E+01	-3.0004E+01		
P201	3.1715E+00	-1.5169E+02		
P210	-9.3060E+01	7.9745E+01		
P030	-5.3575E+00			
P021	-1.7005E+01	-1.0125E+02		
P103	-8.3756E+02			
P310	-1.8746E+03			
P112	1.2034E+03			
P121	-7.0797E+02			
Y001	6.6644E-01	-1.2792E+00	-5.9088E-01	1.0070E-01
Y010	-1.1716E+00	-7.3591E-01	2.0473E-01	
Y110	-1.2006E+01	-7.4347E-01		
Y101	-5.5873E-01	-5.2015E+00	-4.7578E+00	
Y012	4.9334E+00			
Y003	2.2622E+01			
Y201	4.5543E+02	2.3879E+02		
Y210	3.1102E+02	-9.1130E+01		
Y030	4.7275E+01			
Y021	6.1093E+01	1.8791E+02		
Y103	-7.9386E+02			
Y130	1.0332E+03			
Y112	1.8212E+03			
Y301	3.4467E+03			
Y310	2.0201E+03			
Y121	-2.0668E+03			

E.2 HRSH

Element	C_0 term	C_1 term	C_2 term	C_3 term
t000	-1.0050E+00	-3.3613E-01	-4.0828E-02	4.1021E-03
y000	-2.8496E-03	-2.0963E-03		
p000	-1.5000E-03	3.7015E-03	5.4167E-04	-3.8885E-02
D000		8.4083E-02	1.0977E-02	
D100	-3.6552E-02	2.8788E-01	4.5414E-02	-2.4305E-01
D200	-1.8889E+00	2.3637E-01	4.2717E+00	
D002	6.5985E-03	3.4792E-01	-7.3869E-01	
D020	5.7923E-01	6.7117E-01	3.6213E-01	
D011	4.7218E-01	2.4993E-02	-5.0836E-01	
D300	3.0423E+01	-4.5712E+01		
D120	-6.6381E+00	5.4344E+01		
D102	-2.0548E+01	-8.2423E+00		
D111	-2.3487E+01	-3.6214E+01		
D400	2.1520E+03			
D202	-3.8587E+02			
D220	-4.8900E+02			
D004	-3.2195E+01			
D022	-1.5905E+02			
D013	9.8379E+01			
T100	-2.2896E+00	5.0418E-01	3.5689E-02	-7.0449E-01
T200	-3.6320E+00	1.0594E+00	-1.2168E+00	
T002	9.2892E-01	-9.9527E-01	5.6382E-01	
T011	1.0931E+00	2.3203E-01	-2.2600E+00	
T020	1.9557E-01	-5.5917E-01	1.8563E+00	
T120	-3.5913E+01	-5.0596E+01		

Element	C_0 term	C_1 term	C_2 term	C_3 term
T102	7.0259E+00	-1.1836E+01		
T300	2.6225E+01	2.0447E+02		
T040	4.3965E+02			
T220	-2.6534E+03			
T022	6.7276E+02			
T111	-1.6025E+01	1.0197E+01		
T211	-1.4569E+03			
T004	-4.9292E+02			
T202	4.1458E+02			
T013	-9.8358E+02			
T031	-8.3672E+02			
T400	-3.2178E+03			
P001	-6.3921E-01	-1.3752E-01	2.5155E-01	3.3808E-02
P010	-2.6977E-01	3.5996E-01	-2.9549E-01	-4.1009E-01
P012	-2.7086E+01	9.6591E+01	6.8284E+01	
P110	4.1184E+00	-1.4942E+00	-3.6635E+00	
P101	4.7979E+00	1.0219E+00	6.6895E+00	
P003	2.2081E+01	-1.7388E+01		
P201	-4.4012E+01	-1.1585E+02		
P210	-8.0492E+01	4.5335E+01		
P030	-5.2006E+01	-6.8045E+01		
P021	7.2137E+01	7.0909E+01		
P103	-8.0018E+02			
P130	-9.5414E+02			
P301	-5.7890E+02			

Element	C_0 term	C_1 term	C_2 term	C_3 term
P310	-1.2265E+03			
P112	1.6526E+03			
P121	4.2314E+02			
Y000	-2.8000E-03	5.0000E-03		
Y001	7.2375E-01	-1.2442E+00	-6.1419E-01	-5.1404E-02
Y010	-1.3038E+00	-7.2763E-01	1.9965E-01	2.8169E-01
Y110	-1.4394E+01	-5.8599E-01	-2.1977E+00	
Y101	-2.6824E+00	-7.7489E+00		
Y012	1.2734E+02	-1.4658E+02		
Y003	-2.7597E+01	1.5418E+02		
Y201	4.4010E+02			
Y210	2.3204E+02	-1.4032E+02		
Y030	1.0307E+02	6.0966E+01		
Y021	-9.2602E+01	4.1490E+01		
Y103	7.4580E+02			
Y112	-8.2829E+02			
Y301	6.7646E+03			
Y310	4.2477E+03			

Bibliography

[1] T. de Forest and J.D. Walecka, Adv. Phys. **15**, 1 (1966).

[2] B. Frois and C.N. Papanicolas, Ann. Rev. of Nucl. and Part. Sci., **37**, 133 (1987).

[3] E.J. Moniz, Phys. Rev. **184**, 1154 (1969).

[4] P.D. Zimmerman, Ph.D. thesis, Stanford (1969), (unpublished).

[5] R.R. Whitney *et al.*, Phys. Rev. C **9**, 2230 (1974).

[6] C.J. Horowitz and B.D. Serot, Nucl.Phys. **A368**, 503 (1981).

[7] M.N. Rosenbluth, Phys. Rev. **79**, 615 (1950).

[8] I. Sick *et al.*, Phys. Lett., **88B**, 245 (1979).

[9] J.D Walecka, Theoretical Nuclear and Subnuclear Physics, Oxford Univ. Press, p140 (1995).

[10] J.W. Negele, Phys. Rev. C **1**, 1260 (1970).

[11] P.E. Ulmer *et al.*, Phys. Rev. Lett. **59**, 2259 (1987).

[12] G. van der Steenhoven *et al.*, Phys. Rev. Lett. **57**, 182 (1986).

[13] D. Reffay-Pikeroen *et al.*, Phys. Rev. Lett. **60**, 776 (1988).

[14] J.F.J. Van Der Brand, CEBAF PAC 6, PR93-049.

[15] M.W. McNaughton *et al.*, Nucl. Instrum. Methods **A241**, 435 (1985).

[16] E. Aprile-Giboni, *et al.*, Nucl. Instrum. Methods **215**, 147 (1983).

[17] B. Bonin *et al.*, Nucl. Instrum. Methods **A288**, 379 (1990).

[18] R.D. Ransome *et al.*, Nucl. Instrum. Methods **201**, 315 (1982).

[19] N.E. Cheung *et al.*, Nucl. Instrum. Methods **A363**, 561 (1995).

[20] G. Chang, C. Glashausser, S. Nanda and P.M. Rutt, Measurement of recoil polarization in the $^{16}O(\vec{e},e'\vec{p})$ reaction with 4 GeV electrons, TJNAF Proposal 89-033 (1989).

[21] S. Malov, Ph.D. Thesis, Rutgers University 1999 (unpublished).

[22] A. Picklesimer and J.W. Van Orden, Phys. Rev. C **35** (1987) 266.

[23] A.S. Raskin and T.W. Donnelly, Ann. Phys (NY), **191**, 78 (1989).

[24] C. Giusti and F.D. Pacati, Nucl. Phys. **A504**, 685 (1989).

[25] J.D. Bjorken and S.D. Drell, Relativistic Quantum Mechanics, McGraw-Hill, New York, 1964.

[26] N. Dombey, Rev. Mod. Phys. **41**, 236 (1969).

[27] Hiroshi Ito, S.E.Koonin and Ryoichi Seki, Phys. Rev. C **56**, 3231 (1997).

[28] A. Picklesimer and J.W. Van Orden, Phys. Rev. C **40**, 290 (1989).

[29] A.I. Akhiezer and M.P Rekalo, Sov. J. Particle Nucl., **3**, 277 (1974).

[30] R. Arnold, C. Carlson and F. Gross, Phys. Rev. C **23**, 363 (1981).

[31] J.J. Kelly, Adv. Nucl. Phys., **23** ed. by J.W. Neegle and E. Vogt 75 (1996).

[32] B.D. Serot and J.W. Walecka, Adv. Nucl. Phys. **16**, 327 (1986).

[33] J.J. Kelly, LEA: Linear Expansion Analysis, A program to compute nucleon-nucleus scattering and nucleon knockout by electron scattering. "http://www.nscp.umd.edu/kelly/LEA/lea.html".

[34] Z. Y. Ma and J. Wambach, Nucl. Phys. **A402**, 275 (1983).

[35] Z. Y. Ma and J. Wambach, Phys. Lett. **B256**, 1 (1991).

[36] M. Leuschner *et al.*, Phys. Rev. C **49**, 955 (1994).

[37] T. de Forest, Ann. Phys (NY) **45**, 365 (1967).

[38] T. de Forest, Nucl. Phys. **A392**, 232 (1983).

[39] E. D. Cooper, S. Hama, B. C. Clark, and R. L. Mercer, Phys. Rev. C **47**, 297 (1993).

[40] J.J. Kelly, Phys. Rev. C **56**, 2672 (1997).

[41] S. Boffi, C. Giusti, F. D. Pacati, and M. Radici, Nucl. Phys. **A518**, 639 (1990).

[42] S. Boffi, M. Radici, J.J. Kelly, and T. M. Payerle, Nucl. Phys. **A539**, 597 (1992).

[43] G. Höhler *et al.*, Nucl. Phys. **B114**, 505 (1976).

[44] C.J. Horowitz, Indiana University report No. IU/NTC 88-4.

[45] M.V. Hynes, A. Picklesimer, P.C. Tandy, and R.M. Thaler, Phys. Rev. Lett. **52**, 978 (1984); Phys. Rev. C **31**, 1438 (1985).

[46] A. Picklesimer, J.W. Van Orden, and S.J. Wallace, Phys. Rev. C **32**, 1312 (1985).

[47] V. Phandaripande, I. Sick and P.K.A. de Witt Huberts, Rev Mod. Phys. **69**, 981 (1997).

[48] S. Boffi, C. Giusti, F.D. Pacati, and M. Radici, Nucl. Phys. **A518**, 639 (1990).

[49] S. Boffi and M. Radici, Phys. Lett. **B242**, 151 (1990).

[50] S. Boffi and M. Radici, Nucl. Phys. **A526**, 602 (1991).

[51] J. Ryckebusch, K. Heyde, L. Machenil, *et al.*, Phys. Rev. C **46**, R829 (1992).

[52] J. Ryckebusch, L. Machenil, M. Vanderhaeghen, V. van der Sluys, and M. Waroquier, Phys. Rev. C **49**, 2704 (1994).

[53] V. van der Sluys, J. Ryckebusch, and M. Waroquier, Phys. Rev. C **49**, 2695 (1994).

[54] J. Ryckebusch *et al.*, Nucl. Phys. **A624**, 581 (1997).

[55] J. Ryckebusch *et al.*, Nucl. Phys. **A476**, 237 (1988).

[56] J. Ryckebusch *et al.*, Nucl. Phys. **A503**, 694 (1989).

[57] M. Waroquier *et al.*, Phys. Rev. **148**, 249 (1987).

[58] J. Ryckebusch *et al.*, LANL pre-print nucl-th/9904011 (1999).

[59] J.D. Walecka, Ann. Phys. (NY) **83**, 497 (1974); B.D. Serot, J.D. Walecka, Adv. Nucl. Phys. **16**, 1 (1986).

[60] R. Brockmann, R. Machleidt, Nucl.-th/9612004, to appear in: M.Baldo *et al.* (Eds.), Open Problems in Nuclear Matter, World Scientific, Singapore, 1997.

[61] P.A.M. Guichon, Phys. Lett. **B200**, 235 (1988).

[62] S. Fleck, W. Bentz, K. Shimizu, K. Yazaki, Nucl. Phys. **A510**, 731 (1990).

[63] K. Saito, A.W. Thomas, Phys. Lett. **B327**, 9 (1994);Phys. Rev. C **52**, 2789 (1995); C **51**, 2757 (1995).

[64] J.J. Aubert *et al.*, Phys. Lett. **123B**, 123 (1983).

[65] C. Marchand *et al.*, Phys. Lett. **B153**, 29 (1985).

[66] K. A. Dow *et al.*, Phys. Rev. Lett. **61**, 1706 (1988).

[67] S. A. Dytman *et al.*, Phys. Rev. C **38**, 800 (1988).

[68] K. F. von Reden *et al.*, Phys. Rev. C **41**, 1084 (1990).

[69] P. Barreau *et al.*, Nucl. Phys. **A402**, 515 (1983).

[70] M. Deady *et al.*, Phys. Rev. C **28**, 631 (1983).

[71] Z. Meziani *et al.*, Phys. Rev. Lett. **52**, 2130 (1984); Nucl. Phys. **A446**, 113c (1985).

[72] M. Deady *et al.*, Phys. Rev. C **33**, 1897 (1986).

[73] R. Altemus *et al.*, Phys. Rev. Lett. **44**, 965 (1980).

[74] K.W. McVoy and L. Van Hove, Phys. Rev. **125**, 1034 (1962).

[75] J.V. Noble, Phys. Rev. Lett. **46**, 412 (1981).

[76] L.S. Celenza *et al.*, Phys. Rev. Lett. **53**, 891 (1984).

[77] P.J. Mulders, Nucl. Phys. **A459**, 525 (1986).

[78] T.C. Yates *et al.*, Phys. Lett. **B312**, 382 (1993).

[79] A. Zghiche *et al.*, Nucl. Phys. **A572**, 513 (1994).

[80] C.C. Blatchley *et al.*, Phys. Rev. C **34**, 1243 (1986) .

[81] J. Jourdan, Phys. Lett. **A353**, 381 (1995).

[82] J. Morgerstern, Private communication, to be published.

[83] A. Amroun *et al.*, Nucl. Phys. **A579**, 596 (1994).

[84] G.G. Simon *et al.*, Nucl. Phys. **A333**, 381 (1980).

[85] A. Fabrocini and S. Fantoni, Nucl. Phys. **A503**, 375 (1989).

[86] Y. Jin, D.S. Onley and L.E. Wright, Phys. Rev. C **45**, 1311 (1992) .

[87] P.D. Zimmerman, C.F. Williamson and Y. Kawasoe, Phys. Rev. C **19**, 279 (1979).

[88] J.M. Finn, R.W. Lourie and B.H. Cottman, Phys. Rev. C **29**, 2230 (1984).

[89] I. Sick, Comments Nucl. Part. Phys. **18**, 109 (1988).

[90] D.B. Day, J.S. McCarthy, T.W. Donnelly and I. Sick, Ann. Rev. Nucl. Part. Sci. **40**, 357 (1990).

[91] I. Sick in: H. Klapdor (Ed.), Proc. Int. Conf. on Weak and Electromagnetic Interactions in Nuclei, Springer-Verlag, Berlin, p.415 (1986).

[92] T.W. Donnelly and I. Sick, Phys. Rev. Lett. **82**, 3212 (1999).

[93] T.W. Donnelly and I. Sick, MIT-CTP 2780 (Published).

[94] W.M. Alberico, A. Molinari, T.W. Donnelly, E.L. Kronenberg, and J.W. Van Orden, Phys. Rev. C **38**, 1801 (1988).

[95] M.B. Barbaro, R. Cenni, A. DePace, T.W. Donnelly, and A. Molinari, Nucl. Phys. A, in print.

[96] D.H. Lu, A.W. Thomas, K. Tsushima, A.G. Williams, K. Saito, Phys. Lett. **B417**, 217 (1998).

[97] D. H. Lu, K. Tsushima, A.W. Thomas, A.G. Williams and K. Saito, Private communication.

[98] P.A.M. Guichon, K. Saito, E. Rodionov, A.W. Thomas, Nucl. Phys. **A601**, 349 (1996).

[99] A. Chodos, R.L. Jaffe, K. Johnson, C.B. Thorn, V.F. Weisskopf, Phys. Rev. D **9**, 3471 (1974).

[100] A. Chodos, R.L. Jaffe, K. Johnson, C.B. Thorn, Phys. Rev. D **10**, 2599 (1974).

[101] T.A. DeGrand, R. L. Jaffe, K. Johnson, J. Kiskis, Phys. Rev. D **12**, 2060 (1975).

[102] A.W. Thomas, Adv. in Nucl. Phys. **13**, 1 (1984).

[103] S. Theberge, G. A. Millar, A.W. Thomas, Can. J. phys. **60**, 59 (1982).

[104] D.H. Lu, K. Tsushima, A.W. Thomas, A.G. Williams, ADP-97-45/T273, (1997).

[105] J.M. Finn, Private communication.

[106] F. Garibaldi *et al.*, Nucl. Instrum. Methods **A314,** 1 (1992).

[107] W. Bertozzi *et al.*, Nucl. Inst. and Meth. **141**, 457 (1977).

[108] R. Veenhof, Garfield, a drift-chamber simulation program: User's Guide Version 5.18, CERN Technical Memorandom, (1995).

[109] E.A.J.M. Offerman, ESPACE users guide (1997), (unpublished).

[110] E.A.J.M. Offerman, Ph.D thesis, University of Amsterdam (1988) (unpublished).

[111] J. Gao *et al.*, Beam energy measurement at Jefferson Lab using the Hall A Spectrometers, MIT-LNS IR #0498 (unpublished).

[112] Nilanga Liyanage *et al.*, Optics Commissioning of the Jefferson Lab Hall A High Resolution Spectrometers, MIT-LNS IR #1198(unpublished).

[113] Nilanga Liyanage, Ph.D. Thesis, MIT 1999 (unpublished)

[114] E.A.J.M. Offerman *etal.*, The Hall A sextupole crisis: an evaluation of the magnitude of the problem and possible solutions (1995).

[115] M. Berz Nucl. Instrum. Methods, **A298**, 473 (1990).

[116] M. Berz, COSY INFINITY, Los Alamos LA-11857-C:137, 1990, (unpublished).

[117] P. Vernin, private communication.

[118] G. Quemener, Ph.D. Thesis, William & Mary 1999 (unpublished).

[119] M.F. Gari and W. Krümpelmann, Phys. Lett. **B247**, 159 (1992).

[120] M.F. Gari and W. Krümpelmann, Z. Phys. **A322**, 689 (1985); Phys. Lett. **B173**, 10 (1986).

[121] P. Mergell, U.G. Meissner and D. Drechsel, Nucl. Phys. **A596**, 367 (1996).

[122] A.W. Hammer, U.G. Meissner and D. Drechsler, Phys. Lett. **B385**, 343 (1996).

[123] D.H. Lu, A.W. Thomas, and A.G. Williams, Phys. Rev. C **57**, 2628 (1998).

[124] C.F. Perdrisat, V. Punjabi, Electric form factor of the proton by recoil polarization, TJNAL Proposal 93-027 (1993).

[125] G. Quemener, M.K. Jones, C.F. Perdrisat and V. Punjabi, for the Jefferso Lab, hall A collaboration, *et al.*, to appear in the proceedings of the INPC 98, Paris (1998).

[126] P.E. Ulmer, MCEEP-Monte Carlo for Electro-Nuclear Coincidence Experiments, CEBAF-TN-91-01 (1991).

[127] J. Gao, Ph.D. Thesis, MIT 1999 (unpublished).

[128] A. Saha *et al.*, Study of the quasielastic (e,e/p) reaction in ^{16}O at high recoil momentum, TJNAF Proposal 89-003 (1989).

[129] J.F.J. van der Brand, R. Ent, P.E. Ulmer, Polarization transfer in the reaction $^{4}He(\vec{e}, e'\vec{p})^{3}H$ in the quasi-elastic scattering region, TJNAF Proposal 93-049 (1993).

[130] A.W. Thomas, Private communication.

VITA

Krishni Wijesooriya from Colombo, Sri Lanka, received a Bachelors degree in Physics from the University of Colombo in Sepetember 1993. The author entered the University of New Hampshire as a graduate student in September of 1994. There she was actively involved in the construction and testing of the Hall B CLASS scintillators for CEBAF. In the summer of 1996, she transfered to College of William and Mary, joined the nuclear interactions group, and started working in Hall A FPP project at CEBAF. She has taken a majour role in the installation and commissioning as well as the software developement for the analysis of FPP data. Since then she had been an active member of the CEBAF Hall A (e,e'p) program. She received a Masters of Physics in May 1998 and a Ph.D. in June 1999. She has accepted a Research Associate position with the University of Illinois at Urbana-Champaign and will be working on more electron scattering experiments.